

Summer 2002

# Investigation of Port Fuel Injector Spray Mass Distribution by Laser Induced Fluorescence

Tuba Bayraktar  
*Old Dominion University*

Follow this and additional works at: [https://digitalcommons.odu.edu/mae\\_etds](https://digitalcommons.odu.edu/mae_etds)

 Part of the [Mechanical Engineering Commons](#)

---

## Recommended Citation

Bayraktar, Tuba. "Investigation of Port Fuel Injector Spray Mass Distribution by Laser Induced Fluorescence" (2002). Doctor of Philosophy (PhD), dissertation, Mechanical Engineering, Old Dominion University, DOI: 10.25777/9fbh-g066  
[https://digitalcommons.odu.edu/mae\\_etds/111](https://digitalcommons.odu.edu/mae_etds/111)

This Dissertation is brought to you for free and open access by the Mechanical & Aerospace Engineering at ODU Digital Commons. It has been accepted for inclusion in Mechanical & Aerospace Engineering Theses & Dissertations by an authorized administrator of ODU Digital Commons. For more information, please contact [digitalcommons@odu.edu](mailto:digitalcommons@odu.edu).

**INVESTIGATION OF PORT FUEL INJECTOR SPRAY MASS  
DISTRIBUTION BY LASER INDUCED FLUORESCENCE**

by

Tuba Bayraktar  
B.S.M.E., June 1993, Suleyman Demirel University  
M.S.M.E., January 1997, Istanbul Technical University

A Dissertation submitted to the Faculty of  
Old Dominion University in  
Partial Fulfillment of the Requirements for the Degree of

**DOCTOR OF PHILOSOPHY**

**MECHANICAL ENGINEERING**

**OLD DOMINION UNIVERSITY**

August 2002

Approved by:

---

Dr. A. Sidney Roberts, Jr. (Director)

---

Dr. Surendra N. Tiwari (Member)

---

Dr. Arthur C. Taylor III (Member)

---

Dr. Amin N. Dharamsi (Member)

## **ABSTRACT**

### **INVESTIGATION OF PORT FUEL INJECTOR SPRAY MASS DISTRIBUTION BY LASER INDUCED FLUORESCENCE**

**Tuba Bayraktar  
Old Dominion University, 2002  
Director: Dr. A. S. Roberts, Jr.**

Modern internal combustion engines have stringent requirements for performance and reduced toxic emissions. The fuel delivery system, and particularly the fuel injectors, have a vital role in reducing unburned hydrocarbons (HC) and carbon monoxide (CO) in exhaust emission.

The main goal of this study is to map the spatial and temporal distribution of the spray from a low-pressure gasoline fuel injector. To attain this goal, three tasks were performed: (1) the experimental investigation of the spray oscillation as functions of operating pressure and injector timing, (2) the determination of the appropriate dye/fuel combinations for one particular experimental technique, and (3) the demonstration of the capabilities of a Computational Fluid Dynamics (CFD) code, Fluent, in the dispersed two-phase flow solutions.

An experimental technique, planar laser induced fluorescence (PLIF), was employed to investigate the spatial and temporal distribution of the spray mass from a set of four-hole, split-stream port fuel injectors. The spatial and temporal spray evolution in a horizontal cross-section was imaged instantaneously via detection of fluorescence intensities. The lateral displacement of the spray mass is clearly displayed in time

sequence via the PLIF images, and the spray instability is shown to be sensitively dependent upon small geometric differences along the internal flow paths.

In the course of a study to develop a quantitative PLIF diagnostic for the mass distribution emanating from a liquid fuel injector, spectroscopic results were assembled for certain dye/fuel solutions. Experiments were performed with combinations of hydrocarbon solvents and organic dyes. Results are presented in the form of absorption and emission spectra, including extinction coefficients with error analysis, comparisons with data in the literature, and Stokes shift estimates.

A Computational Fluid Dynamics (CFD) code, Fluent, was employed to demonstrate its capabilities in the solution of dispersed two-phase flows. The dispersed two-phase flow consists of discrete elements surrounded by a continuous phase. The continuous phase equations were solved in an Eulerian reference frame. The Lagrangian approach was used to track packets of discrete phase elements. Inputs of the numerical dispersed two-phase flow model were obtained from the conditions of the PLIF experiments. Two cases were solved with the same input and boundary conditions. In the first case the spray consists of droplets with 100  $\mu\text{m}$  diameter. A linear droplet diameter distribution between 40 and 100  $\mu\text{m}$  was specified in the second case. Results indicate the existence of a core region with higher velocity values for both cases. The core region appears at the spray center close to the injection tip. The increase in the spray temperature towards the outlet boundary is larger for the constant droplet diameter case than the linear droplet diameter distribution case. Negligible evaporation is observed in the solution domain for both cases.

## ACKNOWLEDGMENTS

I would like to express my deepest gratitude to my advisor, Prof. A. Sidney Roberts, Jr. I am truly honored to have had his guidance in my studies and to take advantage of his perspectives on science and engineering. During my doctoral study I have faced many obstacles, both in my personal life and in my studies. Prof. Roberts' encouragement and his belief in my abilities were an enormous source of support and inspiration during the hard times. Throughout the years, I have learned to endure the grief without losing optimism and to accept life as a whole-with both joy and hardships. My doctoral study has been a very rewarding experience because I have improved my abilities, broadened my boundaries, and become a stronger individual. Prof. Roberts not only provided me a variety of opportunities in different engineering applications, but also set an example as a self-disciplined, dedicated, hard-working mentor.

I would like to extend my gratitude to the members of my dissertation committee, Prof. Surendra N. Tiwari, Prof. Arthur C. Taylor, and Prof. Amin N. Dharamsi, who provided me guidance during my course of study at ODU.

I would like to gratefully acknowledge the invaluable assistance of Mr. Jeff Pace and the support of this work by Siemens Automotive, Newport News, Va. Mr. Pace, an enthusiastic experimenter, made the experimental part of this study possible.

I want to thank my husband, Ilhan Bayraktar, for his constant support, love, optimism, and smiling face, even during the most stressful times. He has brought joy and sense of humor into my life. I am very fortunate having such a wonderful, loving spouse, a joking, smiling friend, and a logical, intelligent, dedicated engineer in my life.

Finally, I want to thank my family. The memory of my mother and the support of my brother have always been with me. I dedicate this thesis to them.

Tuba Bayraktar

August 2002

## TABLE OF CONTENTS

	Page
LIST OF TABLES.....	vii
LIST OF FIGURES.....	viii
LIST OF SYMBOLS.....	x
 Chapter	
1. INTRODUCTION .....	1
1.1 Motivation.....	1
1.2. Literature on Spray Fluid Dynamics.....	3
1.3. Specific Objectives of the Research .....	7
2. EXPERIMENTAL INVESTIGATION .....	9
2.1. Methods Available for Spray Measurements.....	9
2.1.1. Current Techniques.....	9
2.1.2. Planar Laser Induced Fluorescence .....	17
2.2. Spray Instability Characterization of Port Fuel Injectors Using PLIF.....	25
2.2.1. Discussion of Results.....	30
2.3. Fluorescence and Absorption Spectra of Dyes for Use in Fuel Spray Studies .....	37
2.3.1. The Selection of the Laser Dyes and Working Fluid.....	37
2.3.1.1. Important Concepts in Handling, Storing, and Disposing of Dyes, Solvents, and Solutions.....	41
2.3.1.2. The Toxicity and Health Hazard Information of Current Dyes/Solvents ...	43
2.3.2. The Development of the Experiment and the Instruments of the Experimental Setup .....	46
2.3.3. Discussion of Results.....	49
2.3.3.1. Absorption Measurements .....	49
2.3.3.2. Emission Measurements .....	57
2.4. Auxiliary Experiments: Droplet Generator and Quantum Efficiency .....	62
2.5. Summary of Spectral Results.....	71
3. SPRAY MODELING – DISCRETE and CONTINUOUS PHASES THEORY and NUMERICS.....	73
3.1. Dispersed Two-Phase Flow Modeling.....	73
3.1.1. Continuous Phase Governing Equations.....	75
3.1.2. Discrete Phase Governing Equations.....	77
3.2. Modeling of Spray in Ambient Air.....	85
3.2.1. Discretization .....	85

3.2.2. Inputs and Boundary Conditions .....	86
3.2.3. Cases and Convergence .....	88
3.2.4. Discussion of Results .....	90
4. SUMMARY OF RESULTS and CONCLUSIONS.....	103
4.1. Concluding Remarks for Experimental Results.....	103
4.2. Concluding Remarks for Spray Modeling Results .....	105
REFERENCES .....	108
APPENDIX.....	116
CURRICULUM VITA .....	119



## LIST OF TABLES

Table	Page
2.1 Pressure and trigger delay test matrix, uncertainty in pressure $\pm 0.1$ kPa; uncertainty in time $\pm 0.1$ $\mu$ s. ....	30
2.2 Laser excitation-dye combinations. ....	39
2.3 Fluorescent dye properties and solvent combinations. ....	40
2.4 Corresponding values for absorption maxima and excitation wavelengths.....	49
2.5 Comparison of centroid wavelength for the emission spectra. ....	61
2.6 Stokes shift values.....	62

## LIST OF FIGURES

Figure	Page
2.1 The Phase Doppler Anemometer measurement set-up, Dantec Dynamics (2001a)...	12
2.2 The geometry of the measurement volume, Dantec Dynamics (2001b). ....	13
2.3 The digital imaging of a laser sheet, Eckbreth (1988). ....	17
2.4 The picture of a DEKA IV injector.....	25
2.5 Sectional view of the DEKA IV injector tip.....	26
2.6 Shadowgraph images for the injector with the worst wobble characteristics under static flow condition (injector III).....	27
2.7 The exit orifice disk at the injector tip (the view from the bottom of the injector). ...	28
2.8 Experimental set-up. ....	28
2.9 Time sequence of spray patterns at 100 kPa for three injectors. ....	32
2.10 Time sequence of spray patterns at 300 kPa for three injectors. ....	33
2.11 Time sequence of spray patterns at 500 kPa for three injectors. ....	34
2.12 PLIF mass distribution compared with the accumulator results for (a) injector I, (b) injector II, (c) injector III.....	36
2.13 Experimental setup for the optical absorption measurements. ....	47
2.14 Experimental setup for the emission measurements.....	48
2.15 Absorption spectra for POPOP. ....	50
2.16 Absorption spectra for Anthracene. ....	50
2.17 Absorption spectra for BBQ. ....	51
2.18 Absorption spectra for LD390. ....	51
2.19 Absorption spectra for PPO. ....	52
2.20 Absorption spectra for Naphthalene. ....	52
2.21 The comparison of present absorption spectra results with Berlman's results for (a) POPOP in Cyclohexane, (b) Anthracene in Cyclohexane, (c) PPO in Cyclohexane, (d) Naphthalene in Cyclohexane. The line with symbols shows Berlman's results and the solid line shows the present spectra results.....	56
2.22 Emission spectra for POPOP. ....	57
2.23 Emission spectra for Anthracene. ....	58
2.24 Emission spectra for BBQ. ....	58
2.25 Emission spectra for LD390. ....	59
2.26 Emission spectra for PPO. ....	59
2.27 Emission spectra for Naphthalene. ....	60
2.28 Schematic figure of the experimental setup for single droplet experiments.....	63
2.29 Visualization of water droplets (a) 50 $\mu\text{m}$ orifice size, (b) 100 $\mu\text{m}$ orifice size.....	64
2.30 Quantum efficiency measurements experimental setup. ....	66
2.31 Schematic figure of the integrating sphere. ....	66
2.32 The spectra of $10^{-4}$ [M] Rhodamine 6G solution. Experiment (a): the cuvette is empty; experiment (b): the cuvette is filled with the solution and the laser beam is focused onto the sphere wall; experiment (c): the cuvette is filled with the solution and the laser beam is focused on the cuvette. ....	68
3.1 Mass, momentum and heat exchange between the discrete and continuous phases, Fluent Inc. (1998); reprinted from the Fluent manual with the permission of Fluent, Inc. ....	82

3.2 Computational grid.....	87
3.3 Convergence of the case cdd.....	89
3.4 Convergence of the case lddd.....	89
3.5 Droplet traces colored by the droplet velocity magnitude (m/s) for the case cdd. ....	90
3.6 Droplet traces colored by the droplet velocity magnitude (m/s) for the case lddd. ....	91
3.7 Droplet traces colored by the droplet temperature (K) for the case cdd.....	92
3.8 Droplet traces colored by the droplet temperature (K) for case lddd. ....	92
3.9 Velocity magnitude versus radial position for the case cdd. ....	93
3.10 Velocity magnitude versus radial position for the case lddd.....	94
3.11 Velocity magnitude versus axial position for the case cdd.....	95
3.12 Velocity magnitude versus axial position for the case lddd. ....	95
3.13 Temperature versus radial position for the case cdd.....	96
3.14 Temperature versus radial position for the case lddd. ....	97
3.15 Temperature versus axial position for the case cdd.....	98
3.16 Temperature versus axial position for the case lddd.....	98
3.17 Continuous phase velocity vectors for the case cdd. ....	99
3.18 Droplet traces colored by the droplet residence time (s) for the case cdd. ....	100
3.19 Droplet traces colored by the droplet residence time (s) for the case lddd.....	100
A.1 Intensity fluctuations for Cyclohexane. ....	116
A.2 Intensity fluctuations for Heptane.....	117
A.3 Intensity fluctuations for Hexane.....	117
A.4 Intensity fluctuations for Octane.....	118

**LIST OF SYMBOLS**

<b>A</b>	<b>Area, m<sup>2</sup></b>
<b>C</b>	<b>Concentration, mol/l</b>
<b>C<sub>ε1</sub></b>	<b>Coefficient used in k-ε calculation</b>
<b>C<sub>ε2</sub></b>	<b>Coefficient used in k-ε calculation</b>
<b>C<sub>D</sub></b>	<b>Drag coefficient</b>
<b>C<sub>p</sub></b>	<b>Specific heat or heat capacity, J/g-°C</b>
<b>d</b>	<b>Path length, m</b>
<b>D</b>	<b>Diameter, m</b>
<b>D<sub>32</sub></b>	<b>Sauter mean diameter, m</b>
<b>E</b>	<b>Energy, J</b>
<b>F</b>	<b>Momentum source term</b>
<b>F<sub>D</sub></b>	<b>Inverse of velocity response time, 1/s</b>
<b>h<sub>fg</sub></b>	<b>Latent heat, kJ/kg</b>
<b>H</b>	<b>Enthalpy, kJ/kg</b>
<b>k</b>	<b>Thermal conductivity, J/hr-cm-°C</b>
<b>k<sub>c</sub></b>	<b>Mass transfer coefficient</b>
<b>K</b>	<b>Calibration constant</b>
<b>L</b>	<b>Unabsorbed light</b>
<b>m</b>	<b>Mass, kg</b>
<b><i>m</i></b>	<b>Mass flow rate, kg/s</b>
<b>N</b>	<b>Molar flux, mol/s</b>

Nu	Nusselt number
P	Pressure, kPa
Pr	Prandtl number
Re	Reynolds number
Sc	Schmidt number
$S_h$	Heat source term
$S_M$	Mass source term
t	Time, s
T	Temperature, K
$u$	Velocity, m/s
$u'$	Fluctuating velocity component, m/s
$\bar{u}$	Mean velocity component, m/s
V	Volume, m <sup>3</sup>
w	Uncertainty
$x_j$	Location with subscript array variable j
x,y,z	Coordinates

### Greek Symbols

$\alpha$	Absorption coefficient, l/mol-m
$\epsilon$	Extinction coefficient, l/mol-m
$\phi$	Gaussian distributed random variable
$\eta$	Quantum efficiency
$\lambda$	Wavelength, nm

$\mu_{\text{eff}}$	Effective viscosity
$\mu_t$	Turbulent viscosity
$\nu$	Wave number, 1/cm
$\rho$	Density, kg/m <sup>3</sup>
$\sigma_k$	Prandtl number in k- $\epsilon$ calculation
$\sigma_\epsilon$	Prandtl number in k- $\epsilon$ calculation
$\tau$	Shear stress, N/m <sup>2</sup>

### Subscripts

a	Absorbed
bp	Boiling point
c	Continuous phase
d	Droplet
e	Emitted
f	Final
i	Initial
m	Mass
s	Droplet surface
v	Volume
vap	Vaporization

# CHAPTER 1

## INTRODUCTION<sup>1</sup>

Dispersed two-phase flows are encountered in many diverse applications such as pharmaceutical, agricultural, chemical, and aerospace applications, furnaces, and internal combustion engines. A dispersed two-phase flow consists of discrete elements (solid particles, liquid droplets or gas bubbles) surrounded by a continuous phase (gas or liquid). A spray, which is a type of dispersed two-phase flow, involves liquid droplets as the discrete phase and a gas as the continuous phase. This chapter provides an overview of the subject of the study, fuel sprays for spark ignition engine applications.

### 1.1 Motivation

When the number of automotive vehicles was small in the first half of the twentieth century, designers assumed the atmosphere behaved as an infinite sink and neglected the effect of exhaust emission in it. In the second half of the century, signs of air pollution became more obvious with the growing number of vehicles, power plants, factories, and an expanding population. The amount of exhaust emission was no longer unnoticeable in the large but finite atmosphere. The role of vehicle exhaust emission is the primary concern in today's air pollution problem, especially in industrialized countries. Therefore, stringent exhaust emission standards, especially for hydrocarbon (HC) emission, have been legislated in the United States. Similar standards will also be established in Europe, Japan, and other Asian countries. Modern internal combustion engines must meet these standards without sacrificing driveability and fuel economy.

---

<sup>1</sup> The format of this dissertation is based on the *Experiments in Fluids* journal.

Designers follow two main approaches for reducing toxic engine emissions: one is to prevent non-stoichiometric combustion and the other is to employ an exhaust stream after-treatment. The fuel delivery system, particularly the fuel injectors and associated control components, is a critical link in the performance chain for stoichiometric and lean burn combustion.

In port-injected spark ignition engines, one or more fuel injectors are mounted in the intake manifold close to cylinder inlet valves. The liquid fuel is injected onto the back face of the closed valve. The high surface temperature of the inlet valve enhances the fuel evaporation. The heat transfer from valve to the fuel also helps to cool the valve. When the valve is closed, the air in the intake port is quasi-stationary and does not help mixing. The fuel mass distribution and velocity of droplets mostly govern the mixing process. The fuel vapor-air mixture is transported to the cylinder with the opening of the valve.

The combustion process is influenced not only by the air/fuel ratio but also by the uniformity of the air-fuel mixture. The precisely measured fuel and air amounts must be thoroughly mixed so that as many air molecules contact with as many fuel molecules as possible. Otherwise, the spatial and temporal non-homogeneities of the mixture will prevent uniform burning inside the cylinder and cause exhaust emission of unburned hydrocarbons (HC) and carbon monoxide (CO), see Lenz (1992). In order to determine the fuel mass distribution it is necessary to understand the characteristics of the spray, a statement which is as true for direct injected cylinders as it is for low pressure, port-injected engines.



## 1.2. Literature on Spray Fluid Dynamics

The characterization of a dispersed two-phase flow is essential to evaluate and improve the performance of the system, which employs this type of flow. Numerous experimental techniques have been developed to characterize discrete phase size, velocity, concentration, or mass flux. Crowe et al. (1998) divided experimental methods for dispersed two-phase flows into two main groups: integral methods (e.g., laser diffraction, light absorption) and local measurement techniques. Local measurement techniques were also divided into two main groups: probing methods (e.g., isokinetic sampling) and optical methods (e.g., Particle Image Velocimetry (PIV), Phase Doppler Anemometry (PDA), Planar Laser Induced Fluorescence (PLIF)). Only optical measurement techniques are suitable for spray measurements due to their non-intrusive nature and high spatial resolution. Since the main interest of this study is the fuel spray, techniques other than optical methods will not be explored.

The Phase Doppler Anemometer (PDA) is perhaps the most widely used technique in spray studies among optical methods; see the discussion on PDA in Section 2.1.1. However, PDA does not readily provide information on the temporal and spatial spray characterization. Brown and Kent (1983) pointed to the potential of Planar Laser Induced Fluorescence (PLIF) for measuring spatial distribution of liquid mass in sprays and reported semi-quantitative results. The Planar Laser Induced Fluorescence has been extensively used to determine two-dimensional distributions of species concentrations in cold or reacting gaseous flow fields since the 1980s. The Planar Laser Induced Fluorescence image resolution and signal to noise ratio were significantly improved with the development of the charge-coupled device (CCD) camera; see Paul et al. (1990). Van

Cruyningen et al. (1990) quantified the possible error sources for the propagating signal through the PLIF experiment and described image correction steps. The details of the PLIF species concentration measurements can be found in the study of Greenhalgh (1994). After gaining more quantitative characterization, PLIF received recent attention from spray researchers due to the direct proportionality of resulting signal to the droplet volume. The application of the technique in the liquid spray is based on the measurement of fluorescent intensity from the fluorescent dye doped droplets excited within a laser light sheet; see the detailed description of the technique in Section 2.1.2. Talley et al. (1996a,b) showed that the proportionality is well established for the dilute spray, but additional considerations are necessary for the dense spray. The technique can provide quantitative information on the performance of fuel injectors by determining the temporal and spatial spray mass distribution (Bayraktar et al. (2001a)). Another important characteristic in the evaluation of the injector performance is the ratio of the droplet ensemble volume to the surface area in a distribution, referred to as the Sauter mean diameter (SMD). The Sauter mean diameter was measured by combining fluorescent and elastic-scattered light measurements; see Sankar et al. (1999), Le Gal et al. (1999), and Greenhalgh (2000). The effects of different parameters on the accuracy of the combined technique were evaluated by Domann and Hardalupas (2000). The PLIF technique is also useful in the examination of liquid droplet presence in the fuel vapor-air mixture. Meyer (1998) employed the PLIF technique in an optically accessible engine to obtain the amount of liquid droplets entering the cylinder during the start-up and warm-up conditions.

Gasoline is the conventional fuel for spark ignition engines. However, since the composition of gasoline may vary from batch to batch or summer to winter, simple hydrocarbons such as n-Heptane are generally preferred in PLIF studies. The choice of fluorescent dye is of crucial importance for quantitative PLIF measurements because dye molecules yield laser induced fluorescence. High quantum efficiency and non-toxicity are very desirable characteristics for a fluorescent dye candidate. The selected dye should also be highly soluble in the working fluid. Ketone-type compounds as the working fluid and 3-pentanone as a fluorescent dye have been indicated to be suitable in PLIF application of fuel vapor concentration measurements; see Neij et al. (1994) and Ghandhi and Bracco (1996). Many different fluorescent dye-working fluid combinations were used in PLIF applications of liquid fuel spray mass distribution and SMD determination. Generally, the excitation wavelength of the laser in the experimental set-up is the most important factor in the selection of an appropriate dye. Le Gal et al. (1999) excited p-Terphenyl (PTP) doped kerosene spray by using an Nd:YAG 4<sup>th</sup> harmonic laser; Talley et al. (1996a) illuminated fluorescein doped Methanol spray via an Argon Ion laser and Sankar et al. (1999) illuminated Stoddard solvent spray via an Nd:YAG 4<sup>th</sup> harmonic laser. The most suitable dye according to the laser excitation wavelength can be identified by referring to absorption and emission spectral information. However, there is limited spectral information on the fluorescent dye-working fluid combinations suitable for the fuel spray studies in the literature. Bayraktar et al. (2001b) reported absorption and emission spectra of various fluorescent dye-working fluid combinations in the near-ultraviolet region. The quantum efficiency, which is defined as the number of emitted fluorescent photons with respect to the number of absorbed excitation photons, was

indicated as one of the selection criteria for a fluorescent dye candidate, see Neij (1994). However, no particular quantum efficiency information suitable for fuel spray studies has been encountered in the literature. In the past the relative fluorescence quantum efficiency method was used for quantum efficiency measurements, see Berlman (1965). New quantum efficiency measurement methods were developed recently; see Mello et al. (1997), Fischer and Georges (1996), and Georges et al. (1996). An attempt was made to adapt the method developed by Mello et al. (1997) in this study, see Section 2.4 for further details.

The dispersed liquid spray problem is highly complicated due to the mass, momentum, and energy exchange processes between phases, the interaction of closely spaced neighboring droplets, the effect of gas phase turbulence on the droplet motion, the droplet shape distortion, internal circulation of the liquid in the droplet, and so on. In addition to experimental studies, many computational studies have been conducted to better understand this complicated flow phenomenon. Sirignano (1993) reviewed spray equations for the multi-continua, discrete-particle, and probabilistic approaches in his comprehensive study. In the discrete-particle approach, liquid phase equations are solved in a Lagrangian reference frame, and gas phase equations are solved in an Eulerian reference frame. The discrete-particle approach provides higher resolution than the multi-continua approach, but the total number of droplets that can be solved is limited. The discrete-particle approach was frequently employed in the numerical modeling of sprays; see Wild et al. (1988), Gosman and Ioannides (1983), and Muralidhara et al. (2000). This approach is valid when the spacing between droplets is sufficient, e.g., in the dilute spray

case. The internal circulation of liquid in the droplet is neglected and the droplet shape is assumed as perfectly spherical during the solution.

In the characterization of a fuel delivery system, experimental methods and computational modeling should be treated hand-in-hand. Designers generally identify the best fuel delivery system approach by combining experimental data and numerical model results; see for example Godrie and Zellat (1994). A detailed review of the literature on experimental methods is presented in Chapter 2.

### **1.3. Specific Objectives of the Research**

The purpose of this work is to determine the space and time resolution of the fuel injector spray mass distribution. An experimental method, Planar Laser Induced Fluorescence, was developed to obtain quantitative information on the spray mass distribution from a low-pressure, port fuel injector. The Planar Laser Induced Fluorescence (PLIF) was adapted to investigate the extent of the spray oscillation as functions of the operating pressure and injector timing. The application of the PLIF in the indication of the spray oscillation and injector stability was emphasized. The main attraction of the PLIF technique is the proportionality of the fluorescent light intensity to the volume of the droplet. The choice of the fluorescent dye is very important for maintaining the proportionality between the emitted intensity by the fluorescent dye within a droplet and the droplet volume. However, the spectral information on the fluorescent dye-working fluid combinations for fuel spray studies is very limited in the literature. Emphasis was given to develop a database for the fuel spray PLIF studies. The absorption and emission spectra of various fluorescent dye-working fluid combinations

were determined for this purpose. The detailed information of the PLIF technique and the description of the conducted experiments are presented in Chapter 2.

In Chapter 3 the theoretical formulations and numerical method for the spray modeling are outlined. The aim of the numerical spray modeling is to demonstrate the capabilities of a CFD code, Fluent, in the dispersed two-phase flow solutions. The summary of conclusions and the discussion on the current needs in spray research are presented in Chapter 4.

## **CHAPTER 2**

### **EXPERIMENTAL INVESTIGATION**

The optical techniques for spray measurements are mainly divided into two groups: point measurement techniques and planar measurement techniques. Point measurement techniques provide pointwise information on droplet/particle size, velocity, or concentration. Planar measurement techniques are useful to indicate the global characterization of the spray as well as to make quantitative measurements. Several techniques are included in this chapter because they are the most common and current methods in spray measurements. These include: Phase Doppler Anemometry (PDA) as a point measurement technique, Particle Image Velocimetry (PIV), Raman spectroscopy, and Planar Laser Induced Fluorescence (PLIF) as planar measurement techniques.

A subsection in this chapter is devoted to the introduction of the Planar Laser Induced Fluorescence technique that was used to determine the fuel spray mass distribution in the current study. The detailed information on the PLIF experiments for spray instability characterization is given in Section 2.2. The emission and absorption experiments, which were made to create a database for PLIF experiments, are described in Section 2.3 of this chapter, and auxiliary experiments are discussed in Section 2.4.

#### **2.1. Methods Available for Spray Measurements**

##### **2.1.1. Current Techniques**

The Particle Image Velocimetry (PIV) is an optical method for measuring the local fluid velocities in an illuminated two-dimensional region. Seed particles are added

to the flow and the velocity information of the flow is extracted indirectly by observing the displacement of the particles, if uniformly dispersed seed particles throughout the fluid trace faithfully the fluid pathlines. Particles in a flow region are illuminated at least two times within a short time interval. The light source can be either a white light source such as Xenon lamp or a laser light source (continuous or pulsed laser). A conventional photographic camera or Charged Coupled Device (CCD) camera is mounted perpendicular to the light sheet. The scattered light by the particles is recorded on a single frame or on a sequence of frames. Then, images are transferred to the computer for the image analysis. The image analysis is the most time consuming process of the technique. First, the digital PIV recording is divided in small subareas, i.e., interrogation areas. The velocity of particles is obtained by determining the displacement of particles in the interrogation area between successive images and known time interval.

Since PIV technique measures the velocity of the fluid element indirectly by measuring the displacement of the seed particles, the experimenter must check very carefully if the seed particles follow the fluid elements faithfully. Small particles follow the flow better; on the other hand, larger particles scatter more light. Tiny particles are used in gas flow PIV applications. In this case, a high power light source is needed to produce enough scattering. In liquid flow PIV applications, larger particles and lower power light source can be used. The seed particles should be distributed uniformly throughout the fluid and have no effect on the fluid or flow properties for accurate measurements. Raffel et al. (1998) and Adrian (1991) described three types of image density for PIV. In the Particle Tracking Velocimetry (PTV), the scattering particle concentration is low enough to detect individual particles. The tracking method is applied



to measure the displacement of particles. In the laser-speckle velocimetry (LSV), the images of particles overlap in the image plane because of the high scattering particle concentration. Image evaluation requires statistical techniques. The medium image density technique lies between the PTV and LSV methods.

Whereas PIV has been commonly applied to the single-phase turbulent flow for a long time, the two-phase turbulent flow application such as flow of solid particles or liquid droplets or bubbles suspended in a turbulent flow is becoming popular. Perkins and Hunt (1989) investigated particle trajectories in the wake of a horizontal cylinder and in an upward pipe flow by using PTV. Their main objective was to understand how particles and bubbles respond to the structure of a turbulent flow. Govan et al. (1989) visualized the motion of glass particles in an air stream in a vertical tube. They obtained the trajectories and velocities of the particles and found that the particle motion is strongly dependent on inlet conditions. Hassan et al. (1992) observed the rising air bubbles in a tank filled with transparent mineral oil. The velocity vectors were measured for both bubbles and the surrounding seeded liquid.

The Laser Doppler Velocimetry (LDV), the Phase Doppler Velocimetry (PDV), and the Phase Doppler Anemometry (PDA) were frequently used in spray studies. The Laser Doppler Velocimetry is an optical point measurement technique that is used to measure the velocity of the flow. The Phase Doppler Velocimetry is a variation of LDV. It is possible to measure both the diameter and the velocity of spherical particles/droplets simultaneously by using PDV. The Phase Doppler Anemometry is an extension of PDV. The velocity, size, and refractive index of spherical particles can be measured by using PDA. The particle concentration can also be obtained with this technique. The physical

basis of the three techniques is same. There are only slight differences in the measurement set-up depending on the application purposes. The applications of PDA measurements are powder production, bubble dynamics, sprays, and liquid atomization processes such as fuel sprays, paint coating, agricultural sprays, and pharmaceutical sprays. Figure 2.1 shows the schematic sketch of a PDA measurement set-up.

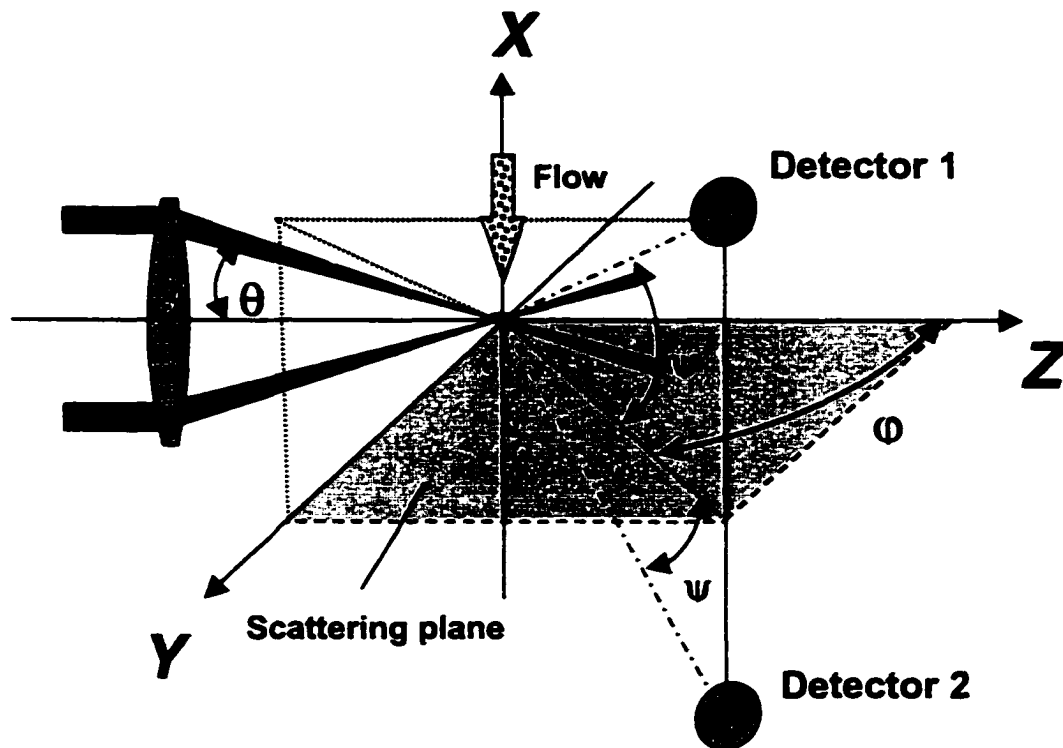


Figure 2.1 The Phase Doppler Anemometer measurement set-up, Dantec Dynamics (2001a).

The two focused laser beams with  $\theta$  beam intersection half-angle intersect at a point in the flow region. The flow may consist of liquid droplets or bubbles or solid particles. It is frequently necessary to use seed particles in order to get flow data. Seed particles are considered as moving receivers and transmitters of light waves in the flow. If seed particles penetrate a laser beam, they scatter certain amount of light. In this case, seed

particles act as “transmitters.” However, they have to act as “receivers” before scattering the light. In Figure 2.1,  $\phi$  refers to the scattering angle. In PDA systems, two detectors are used to measure the particle size and the particle velocity simultaneously. The angle  $\psi$  refers to the detector elevation angle in Figure 2.1.

In the application of PDA, the ellipsoidal measurement volume is formed by the intersected laser beams. The size of the measurement volume depends on the laser power and optical components. In the laser beam intersection region, the pattern of bright and dark planes occurs. Figure 2.2 shows the ellipsoidal measurement volume.

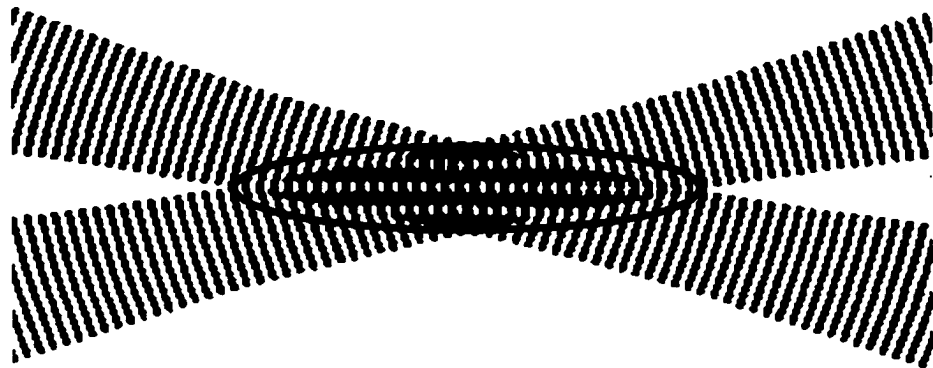


Figure 2.2 The geometry of the measurement volume, Dantec Dynamics (2001b).

When a droplet/particle penetrates the measurement volume, a diffraction pattern image is refracted to photodetectors. The photomultiplier tube or photodiode can be used to detect the scattered light intensity. The droplet/particle size information is obtained from the spacing between fringes in the pattern and the droplet/particle velocity is measured from the time for a fringe to travel past two detectors. Particles moving in either the forward or reversed direction produce identical signals and frequencies. By introducing a frequency shift into one beam relative to the other will cause the

interference fringes to appear to move at the shift frequency. Negative velocities can be distinguished with frequency shifting. For accurate measurements, seed particles must follow the flow faithfully. The characteristics that play a role in the selection of tracers are size of the tracer, specific gravity, scattering direction, ease of use, and non-toxicity. The optimum seed particle traces the flow to the desired frequency while providing a sufficient signal-to-noise ratio (SNR) to produce accurate results. The Phase Doppler Anemometry signal is not continuous, because the measurement is obtained for each droplet/particle that penetrates the measurement volume. The statistical droplet/particle data is created from measurements for that point in space. Since PDA is a point measurement technique, it is necessary to move the measurement volume (or the flow path) in order to get data for the whole field. This technique may give high spatial resolution due to the small measurement volume. It also provides high temporal resolution. It is an absolute measurement technique, i.e. no calibration is required. The technique is insensitive to temperature and pressure variations. However, PDA has some disadvantages. The data is obtained only while a droplet/particle passing through the control volume. The technique is problematic if droplets/particles are not spherical. When multiple droplets/particles exist in the measurement volume at the same time, the data cannot be used. The Phase Doppler Anemometry may not give quantitative measurements if the spray is too dense or too close to the injector tip or nozzle. Tedious data analysis is required to obtain the global characterization of the flow. Seed particles' tracking ability may be limited due to inertia and slip. The other important problem is noise. The detector system always contains noise. Some noise is generated in the electronics between the photodetector and signal processor, and part of the noise is

generated within the detector itself. The noise that is generated within the detector is called shot noise. Shot noise is the fundamental limit on the SNR.

The Phase Doppler Anemometry has an extensive application in liquid sprays. Naqwi et al. (1996) developed an adaptive hardware of PDV and applied this new PDV system to measure particle sizes in submicron and nanometer ranges. Results for spray of a pressure atomizer, droplets from single jet and six-jet atomizer, droplets from a condensation droplet generator, metal particles, and liquid droplets within a liquid medium have been reported. The size and velocity of metallic particles as small as 20 nm, transparent particles in the submicron range, and droplets with refractive index close to the surrounding medium were successfully measured. Ismailov et al. (1999) used LDA to measure centerline velocity in the fuel pipeline and used PDA to measure droplet velocity, size, and number density from a high-pressure swirl fuel injector. The authors indicated that PDA could be used for fuel spray quality evaluation especially for spray temporal characterization. Yurteri et al. (1993) used PDA to determine the spray characteristics of nozzles and the interaction between two nozzle sprays. The atomizing air pressure was reported as the most important factor for the droplet size. Results showed that the increased air pressure leads to smaller diameters and larger velocity. The effect of the intersection angle and air pressure on the droplet size was investigated for two interacted sprays. The authors indicated that during the impact of sprays, the droplet might not remain spherical and PDA could not sense this effect.

In Raman Scattering, an incident photon collides with a molecule in the initial energy level,  $E_i$ , then the molecule absorbs  $\Delta E_a$  amount of energy and immediately emits  $\Delta E_e$  amount of photon energy. When the energy absorbed by the molecule is unequal to

the emitted energy, the final energy level of the molecule,  $E_f$ , is different than in the initial energy level. If the exiting photon energy is lower than the incident one, the phenomenon is called Stokes scattering. If the exiting photon energy is higher than the incident one, the phenomenon is called anti-Stokes scattering. In any case, the energy difference must be  $E_f - E_i = \Delta E_m = \Delta E_e - \Delta E_a$ .

Variants of Raman spectroscopy are stimulated Raman spectroscopy (SRS), stimulated inverse Raman spectroscopy (SIRS), Photoacoustic Raman spectroscopy (PARS), Raman-induced Kerr effect spectroscopy (RIKES), and hyper Raman spectroscopy. In SRS, a high intensity laser source (pulsed or continuous wave) is employed to coherently excite molecules. The stimulated Raman spectroscopy has an extensive application in hostile environments such as combustion. Two essential properties can be obtained by using SRS in combustion studies, namely the species concentration and the temperature of the flame. The stimulated Raman spectroscopy is also a valuable technique in the determination of evaporation rate for an injected spray prior to combustion. Swindal et al. (1996) investigated droplet evaporation, including the effect of neighboring droplets, and the shape distortions of flowing droplets in the quiescent atmosphere by using SRS. The technique was also employed to capture the images of spray from a hollow-cone nozzle.

Three important light scattering characteristics were discussed in the use of lasing emission and SRS. First, the curved surface between the liquid and the surrounding air may act like a lens and may concentrate the incident radiation to a small region near the shadow side of the droplet. When an input resonance (resonant mode of the droplet) differs from the input wavelength, the input radiation is stored inside the droplet. This

phenomenon is called morphology-dependent resonances (MDRs). Second, if emitted rays within the droplet strike the droplet interface at an angle larger than the critical angle, rays are reflected many times around the droplet circumference. If rays return to their initial point with their initial phase, they are trapped within the droplet and the droplet becomes an optical cavity for that particular wavelength. Third, if a molecule is located in the (MDRs) region, the probability of emission at discrete wavelengths is higher.

### 2.1.2. Planar Laser Induced Fluorescence

The laser sheet techniques are very suitable for spray diagnostics since they provide information about the two-dimensional characterization of the spray. The laser sheet is generated by employing the cylindrical lenses. A rectangular element of the laser sheet is imaged onto the array detector by using an optical lens system. Figure 2.3 shows the two-dimensional digital imaging of a laser sheet.

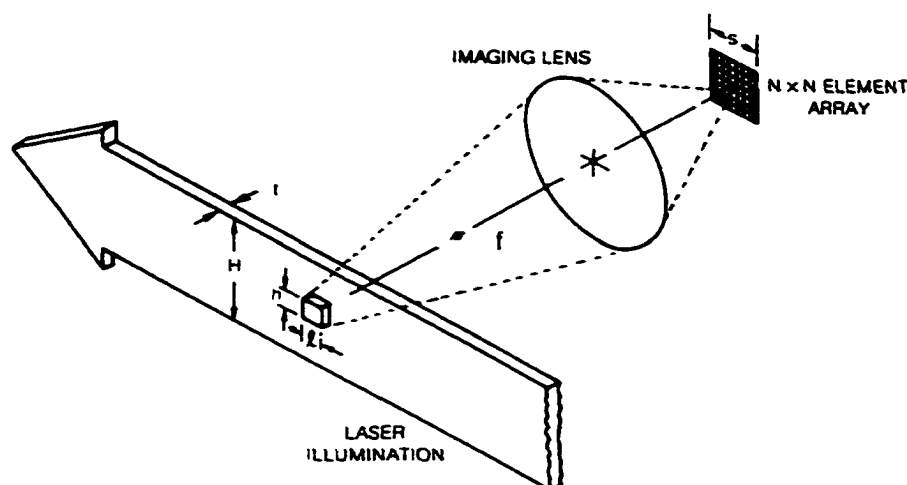


Figure 2.3 The digital imaging of a laser sheet, Eckbreth (1988).

The Planar Laser Induced Fluorescence (PLIF) is a laser sheet technique. The method frequently employs a small amount of fluorescent dye dissolved in the fluid. A laser sheet about 1 mm thick is generated, the extent of which preferably covers the whole spray; however, the light sheet may be designed to section the spray orthogonal to the spray axis. The incident laser light excites the dissolved fluorescent dye in droplets. The fluorescent dye first absorbs the incident light and then spontaneously emits with a different wavelength. In other words, the emitted fluorescence is red-shifted. A recording system, the Charged Coupled Device (CCD) camera, and an appropriate bandpass filter are required in the measurement system. Each pixel in the CCD array detects the total intensity from all droplets in the measurement volume.

The measurement volume,  $\delta V$ , consists of the small area imaged by the camera optics and has the thickness of the laser sheet. An average liquid mass concentration in the measurement volume is defined as

$$\bar{\rho}_m = \frac{\delta m}{\delta V} \quad (2.1)$$

where  $\delta m$  is the liquid mass present in the measurement volume. Talley et al. (1996a) described the discrete phase density  $\rho(x,y,z)$ , through the following equation when the area imaged by the camera optics is sufficiently small and the statistical sample is sufficiently representative of the spray

$$\bar{\rho}_m = \rho(x, y, z) = \int_0^{\infty} \frac{\pi}{6} \rho_l D^3 n(D|x, y, z) dD \quad (2.2)$$



where  $D$  is the droplet diameter,  $\rho_l$  is the density of the pure liquid, and  $n(D|x, y, z)dD$  is the number of droplets per unit volume with diameters between  $D$  and  $D+dD$ , as a function of position  $(x, y, z)$ .

The total light emission per unit laser sheet area for unsaturated excitation,  $N_c^*$ , is defined as follows:

$$N_c^* = \{ \textit{Photons Incident per unit Height} \} \\ \times \{ \textit{Photons Absorbed per unit Length} \} \\ \times \{ \textit{Photons Emitted per Photon Absorbed} \} \quad (2.3)$$

The last term is the quantum efficiency in the above equation. It is assumed that the number of absorbed photons is proportional to the number of fluorescence molecules for a small and uniform dye concentration within droplets. The number of fluorescence molecules is proportional to the average amount of liquid mass if the dye concentration is constant and uniform. The number of incident photons per pixel of a camera,  $N_{pp}$ , is given by the following equation,

$$N_{pp} = \{ \textit{Emission per unit Area} \} \times \{ \textit{Area} \} \times \{ \textit{Calibration Constants for Optics} \} \quad (2.4)$$

where the first term is introduced by Equation (2.3) and the second term, area, refers to the small area imaged on the laser sheet by the camera optics. The digital signal level for a pixel,  $N_D$ , is given by,

$$N_D = \{Incident\ Photons\} \times \{Camera\ Calibration\ Constants\} \quad (2.5)$$

In other words, the gray level registered as output from a CCD camera by a pixel element is defined as follows:

$$G = K' \bar{I} \delta m = K \bar{I} \rho \quad (2.6)$$

where  $K'$  and  $K$  are the proportionality constants containing all optics and electronic transfer functions (calibration constants), and the quantum efficiency;  $\bar{I}$  is the average laser sheet intensity;  $\delta m$  is the average amount of liquid mass;  $\rho$  is the discrete phase density given by Equation (2.2).

The Planar Laser Induced Fluorescence has been mainly implemented to obtain the liquid mass distribution of sprays. Another LIF application, combustion, will not be treated here. In engine-related research, workers have employed PLIF measurements in cold flow to evaluate the effect of different parameters on the fuel spray and seek ways to improve and control air-fuel mixing. For example, Baritaud and Heinze (1992) investigated the effect of compression on the air-fuel mixture in a port-injected engine by using PLIF. Experiments were also made by changing the injection timing relative to the timing of the intake valve. The effect of injection phasing on the mixture distribution was reported. Dawson and Hochgreb (1998) employed the PLIF technique with an optically accessible engine to visualize fuel entering the cylinder during the cold start. Images were captured from the inlet valve region. The authors investigated the distribution of the fuel entering the cylinder as a function of time and crank angle.

The Planar Laser Induced Fluorescence technique has also been used in conjunction with the Mie scattering technique for obtaining information on Sauter mean diameter (SMD) in spray studies. The main attraction of the PLIF in liquid fuel spray studies is that the resulting intensity signal is proportional to the mass of fuel droplets illuminated by the laser sheet as illustrated in Equation (2.6). However, this proportionality is only valid under certain conditions. Talley et al. (1996a) summarized the effects that limit the accuracy of the PLIF technique. The most important effect is known as secondary scattering. This effect arises when the once-scattered light leaves the laser light sheet and strikes other molecules outside of the laser sheet region. In this case, a fluorescence signal may reach the camera from the molecules outside of the laser sheet sample volume. Besides, the emitted fluorescence may be re-absorbed or scattered by other droplets in the path between the sample volume and the detector. Secondary scattering effects should be minimized when obtaining quantitative information from the PLIF technique. These effects are more critical for dense spray PLIF applications. The discussion on dense spray applications of PLIF can be found in the study of Talley et al. (1996b). Other effects, that may limit the accuracy of the technique, will be emphasized in the subsequent paragraphs of this section. At this point, it is appropriate to briefly define Mie scattering. When the size of particles in a medium is on the order of the incident light wavelength and the refractive index of particles differs considerably from the surrounding medium, the scattering from particles is called Mie scattering. Mie scattering is an elastic scattering process. In other words, no net energy exchange occurs when the incident photons strike the particles. Therefore, the scattered light frequency is the same as its incident light frequency. Mie scattering does not depend upon the

molecular number density or temperature. The Mie scattering technique is based on the proportionality of the particle size to the scattering distribution and the intensity. If light is elastically scattered by molecules or small particles with diameters much smaller than the laser light wavelength, the elastic scattering is called Rayleigh scattering. In this text, the emphasis will only be given to the use of the Mie scattering technique in conjunction with the PLIF technique.

The combination of PLIF and Mie scattering techniques has been referred to by using different names such as Laser Sheet Dropsizing (LSD), Planar Laser Scattering (PLS), Planar Droplet Sizing (PDS). All of these names, used by different researchers, express the same idea. The combined technique is useful for measuring droplet Sauter mean diameter, e.g., see Le Gal et al. (1999). The Sauter mean diameter is defined as the ratio of the particle or droplet ensemble volume to the surface area in a distribution. If the recording system of the LSD technique involves only one CCD camera, the fluorescent and scattering intensity can be distinguished by using two bandpass filters in front of the camera. One filter transmits the fluorescence emission and the other filter transmits the scattered light. For the successful implementation of the technique, the central wavelengths of the filters should not interfere with each other. When two CCD cameras with appropriate bandpass filters are employed, one camera may detect the scattered light around the incident laser light wavelength, and the other camera may detect the fluorescence intensity from a known emitter. The Stokes shift is useful to distinguish emitted light from the scattered light. The Stokes shift refers to the difference between the peak fluorescent wavelength and the incident excitation wavelength.

When the droplet diameter is much greater than the laser wavelength and morphology dependent resonance (MDR) effects are negligible, the light signal from a droplet is given by:

$$S = CD^\alpha \quad (2.7)$$

where  $C$  is a constant and  $\alpha$  is an index of dependence. The elastically scattered light intensity is proportional to the square of the droplet diameter (droplet area). The PLIF intensity is proportional to the cube of the droplet diameter (droplet volume) in the ideal case, but certain conditions need to be satisfied. If the molecules of a droplet are not equally illuminated, the whole volume of the droplet cannot contribute to the PLIF signal. There are two ways to maintain equal illumination throughout the volume: either very low dye concentration can be used or weakly absorbing dye can be employed. The low dye concentration method is employed in the current experiments, promoting what may be termed a saturation spectroscopy technique. Equations (2.6) and (2.7) are similar if  $\alpha = 3$  and Equation (2.7) is multiplied by the liquid droplet density, where Equation (2.7) is understood to represent the emitted signal for a control volume.

The ratio of the LIF intensity to the elastic light scattering (Mie scattering) intensity gives the LSD signal, e.g., see Sankar et al. (1999).

$$\frac{I_f(x, y)}{I_s(x, y)} = \ell D_{32}(x, y) \quad (2.8)$$

where  $\ell$  is a calibration constant and  $D_{32}(x,y)$  is the spatial SMD. Since the LSD signal is directly proportional to the SMD, the SMD information at each point can be obtained throughout the spray field.

Yeh C.-N. et al. (1996) have proposed the LSD technique to measure the two-dimensional SMD distribution in transient dense sprays. The authors indicated that the droplet diameter decreases with distance from the inlet orifice to a minimum value along the central axis of the spray. In the radial direction, larger droplets were mostly observed in the periphery of the spray. Le Gal et al. (1999) compared the LSD technique results with the PDA technique results for the spray from a pressure-swirl atomiser and obtained very good agreement. The authors indicated that the LSD data set for the pressure-swirl atomiser was obtained within three hours. If PDA were employed to map the entire spray, it would take much longer time. The Laser Sheet Dropsizing provides the information on the two-dimensional characterization of the spray within a shorter time period since the data acquisition is faster for it.

The Laser Sheet Dropsizing method has recently become popular as an alternative to PDA in SMD measurements. The selection between the combined technique (LSD) and the PLIF technique depends on the application purpose. If the main goal is the determination of the fuel spray mass distribution, the PLIF technique is the only tool among current methods. The details of the PLIF measurements for the present study are given in Section 2.2.

## 2.2. Spray Instability Characterization of Port Fuel Injectors Using PLIF

An experimental investigation of the liquid spray pattern changes was carried out for three geometrically similar four-hole split-stream port fuel injectors. For the selected low pressure fuel injectors considered here, the fluid exits the orifice plate as liquid jets, which subsequently break up into ligaments and droplets. Recirculation zones and turbulent eddies adjacent to the orifice plate holes within the fuel injector can impart lateral velocity components to the emerging jet. As these internal flow fields evolve, the issuing jet and spray structure may oscillate or “wobble.” The purpose of this set of experiments is to show the application of the PLIF to estimate the extent of the spray oscillation as functions of operating pressure and injector timing.

The injectors tested were variants of the DEKA IV family made by Siemens Automotive, Newport News, Virginia, USA. The picture of a DEKA IV injector is shown in Figure 2.4.



Figure 2.4 The picture of a DEKA IV injector.

The nominal static flow rate was 2.50 g/s and the dynamic flow rate was 4.38 mg/pulse, using a 2.5 ms pulse width and a 20 ms period, at 300 kPa (gauge) system pressure. The injector-opening transient is completed in 1.25 ms for 300 kPa. The injector needle lift was 90  $\mu\text{m}$  and the coil resistance was 11  $\Omega$ . Figure 2.5 shows the sectional view of the injector tip.

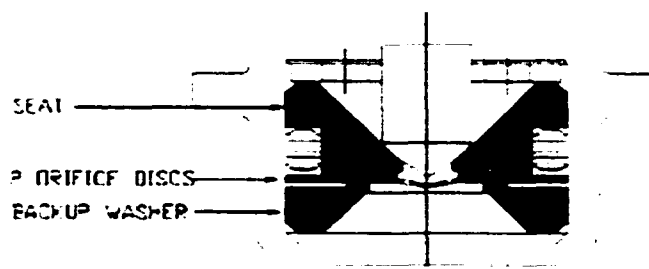
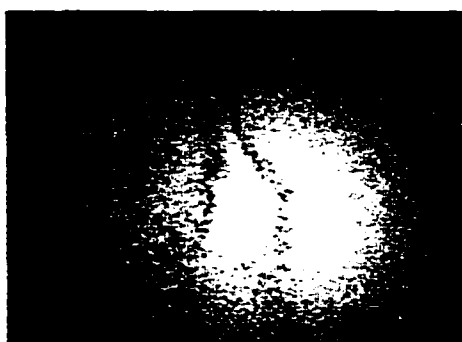


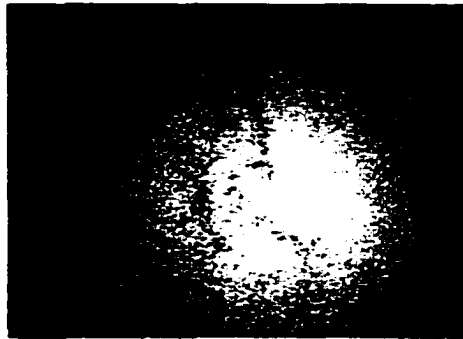
Figure 2.5 Sectional view of the DEKA IV injector tip.

Examples of this spray oscillation are shown in the shadowgraph images in Figures 2.6(a)-(c) for the injector with the worst wobble characteristics (injector III), under static flow conditions. Static flow refers to the flow condition when the injector needle is fully lifted. Even for the static flow condition, the jet oscillation of the right stream in Figures 2.6(a)-(c) is particularly evident.

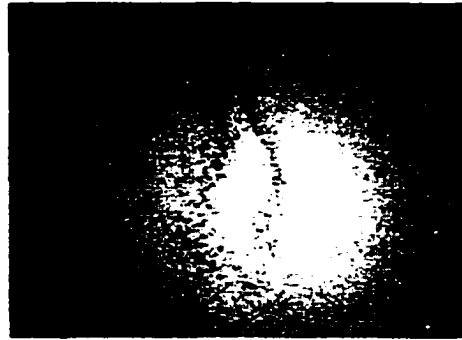


(a)





(b)



(c)

Figure 2.6 Shadowgraph images for the injector with the worst wobble characteristics under static flow condition (injector III).

The shadowgraph images shown imply a timed sequence during static flow. It should be noted that the actual jet trajectory is a complex, three-dimensional path, which is imaged here as a two dimensional projection. As the injector needle is lifted a complex flow pattern is established internally, and free jets emerge from the orifices. Changing the internal spacer plates, the orifice disks size and diameter ratios, influences the internal flow field, the jet atomization characteristics and the ensuing spray pattern. To observe the effect of small geometrical differences on the spray pattern, three DEKA IV injectors were tested under dynamic flow conditions. The internal geometry of injectors was identical except for tolerance differences. The exit orifice disks of these injectors have four holes, as shown in Figure 2.7, with the right set of holes made larger to increase the

flow rate on that side, with the intention of a 60/40 mass split. The two jets on each side combine to form a single jet resulting in a split stream pattern.

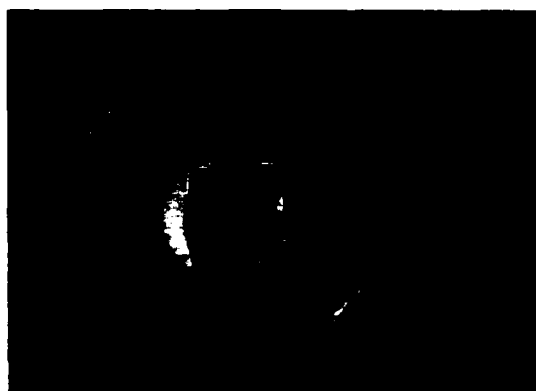


Figure 2.7 The exit orifice disk at the injector tip (the view from the bottom of the injector).

A system to acquire laser induced fluorescence images was constructed using commercially available components. A schematic of the experimental layout is shown in Figure 2.8, and the various subsystems are described below.

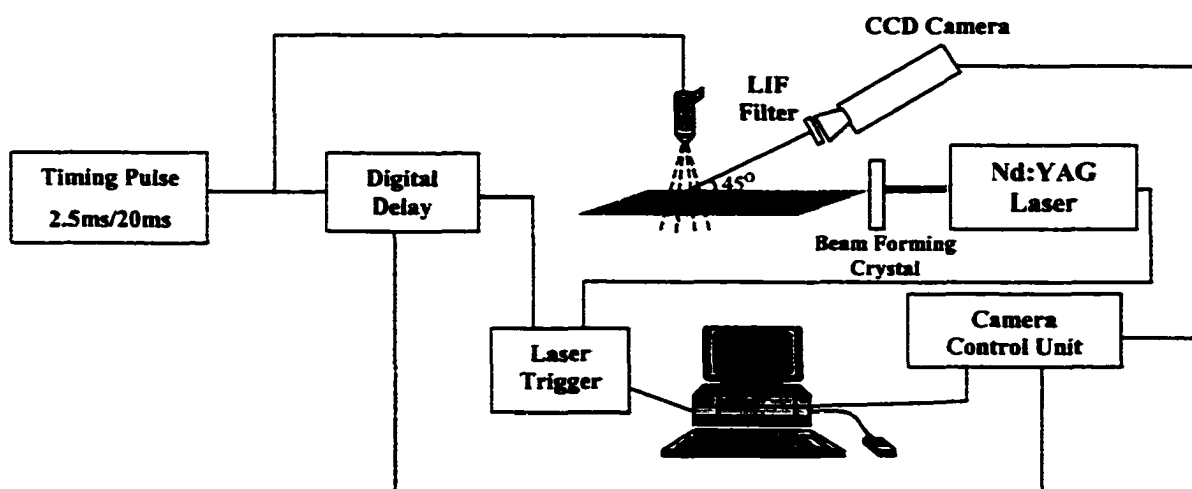


Figure 2.8 Experimental set-up.

An intensified camera made by Xybion Corp. (ISG350) was used for these measurements. The intensifier was operated at a readout voltage of 4.95 Volts. The camera was operated in the gated inhibit mode, allowing precise control of the camera exposure time, which was set at  $1 \mu\text{s}$  for these measurements. The camera lens used was a Nikon micro 60 mm f#2.8, a band-pass filter (Melles Griot 03FTV008), having a center wavelength of 550 nm and full width at half maximum (FWHM) of 10 nm, was used to block the primary scattered laser light. The camera is positioned 25 cm away from the center of the laser light sheet with a  $45^\circ$  view angle. The images were acquired on a PIII-500 Intel PC running the Microsoft NT operating system under the National Instruments LabView instrumentation software package. The frame grabber board (PCI1408) was made by National Instruments. Programs in LabView were developed to acquire a sequence of fifty images synchronized to an external trigger. These images were stored as bitmap files for further processing. The laser used in this study was a diode pumped, Nd-Yag made by Lightwave Electronics (Model 210G). This device, frequency doubled, Q-switched, operating at 532 nm, is capable of pulsed ( $\sim 20\text{ns}$ ) and continuous wave operation. The working fluid was n-Heptane, and the fluorescent dye used was UNISOL Liquid Yellow F1, from the UCM Corporation. The dye concentration was  $5 \times 10^{-3} \pm 1\%$  molal. The horizontal cross section imaged was 50 mm below the injector tip. The laser light sheet was formed using a Lasiris uniform light sheet generator, #SLH-501L-30. Turning mirrors were used to guide the laser beam to the beam forming optic. The laser light sheet, set orthogonal to the injector centerline, was 12 cm across by 1 mm thick, positioned 50 mm below the injector tip. The total laser beam energy was measured as  $620 \pm 5\% \mu\text{J/pulse}$  using a Moletron J25 pyroelectric detector, and the light sheet

uniformity was measured as  $70\pm 3\%$   $\mu\text{J}$  across the beam profile. Beam stops are used to block the light sheet edges. Custom circuitry was used to generate the injector timing pulse train. The fluid delivery system was based on an air-over accumulator reservoir, pressurized by shop air controlled by a precision Bellofram regulator.

The experimental procedure adopted was to select the desired operating pressure, select the desired trigger delay time and acquire a sequence of images. Fifty PLIF images at each of three operating pressures and nine time delays were acquired for the three selected injectors. These test conditions are summarized in Table 2.1.

Table 2.1 Pressure and trigger delay test matrix, uncertainty in pressure  $\pm 0.1$  kPa; uncertainty in time  $\pm 0.1$   $\mu\text{s}$

Test Pressure (kPa)	100	300	500
Trigger delay times (ms)	6.00	4.25	3.50
	6.25	4.50	3.75
	6.50	4.75	4.00
	6.75	5.00	4.25
	7.00	5.25	4.50
	7.25	5.50	4.75
	7.50	5.75	5.00
	7.75	6.00	5.25
	8.00	6.25	5.50

### 2.2.1. Discussion of Results

The particular results of interest are emphasized in this section; namely, the unstably dispersed spray passing through the laser light sheet spaced 50 mm below the injector

orifices, and the data demonstrating the ability of the PLIF procedure to measure the mass distribution accumulating from an injection event.

Figure 2.9 shows the unsteady spray patterns in the light sheet plane with pressure differential of 100 kPa for the three injectors tested, viz., injector I, injector II, and injector III. The trigger delay times after the start of injection are shown under the middle figure of each row. At each trigger delay time, a sequence of fifty images was taken. The spray pattern shown for each delay time was obtained by averaging the fifty images. The sequence of delay time images records the spatial variation in spray cross-section as the spray mass passes through the light sheet.

The injectors were randomly taken from the same assembly line and were called injector I, II, and III for comparison of their spray characteristics. As it can be seen from Figure 2.9, injector I provides well-targeted, distinguishable spray streams. However, injectors II and III display a varying degree of spray instability from targeted (injector II) when passing through the sampling plane, to randomly distributed in time and space (injector III). Besides bad targeting characteristics, injector III fails to maintain two separated spray streams. A consistent result is observed with increasing driving pressure for each injector and for all delay times; see Figures 2.10 and 2.11. The fluorescent intensities observed in the sample plane increase, and this is consistent with the hypothesis of increasing intensities being proportional to increasing spray mass. The results suggest that fuel spray targeting can be effected by even very small internal geometry differences within tolerance. By using PLIF as a testing procedure after the manufacturing process, the spray instability can be rapidly detected, and unstable injectors could be easily distinguished.

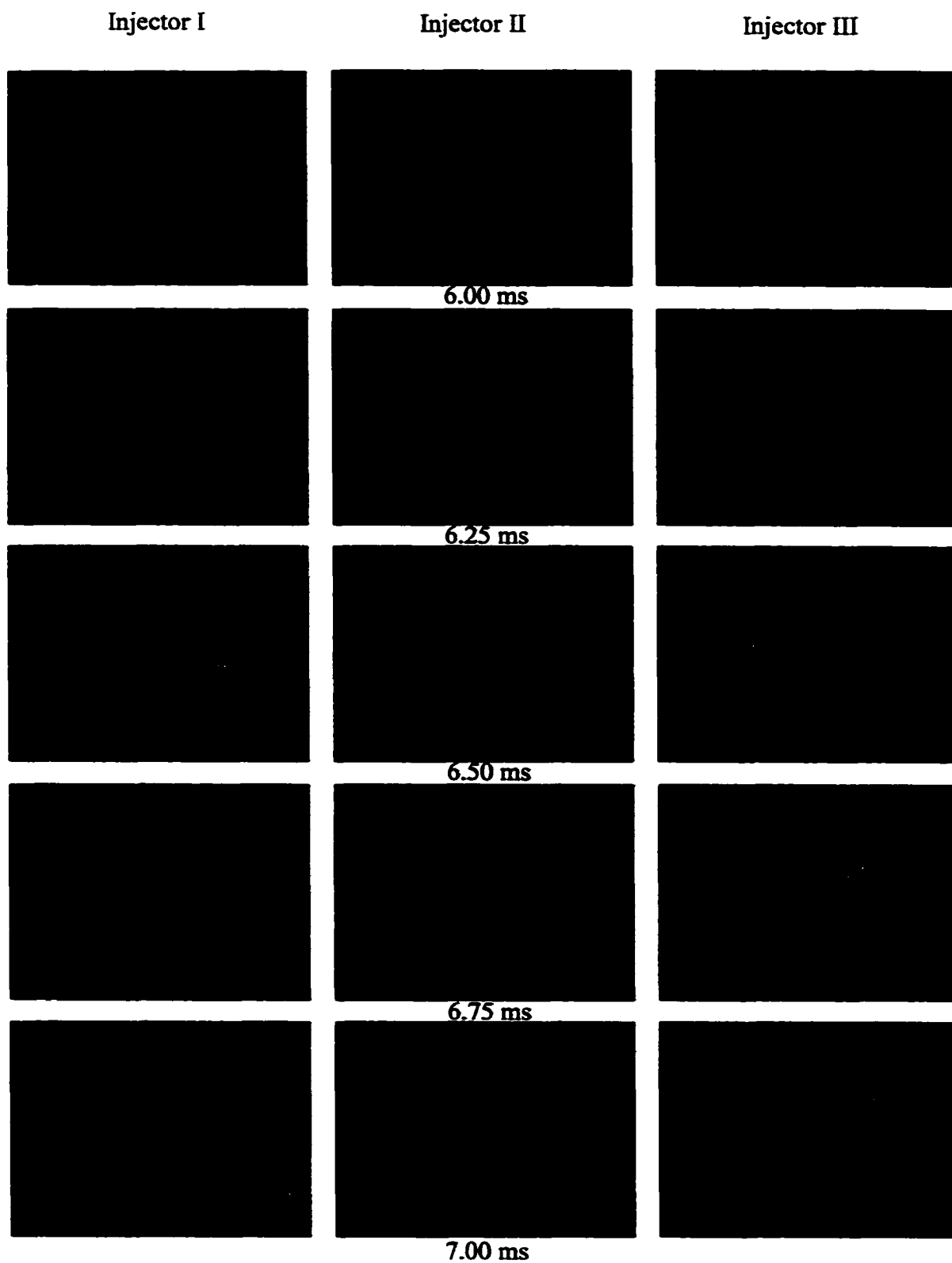


Figure 2.9 Time sequence of spray patterns at 100 kPa for three injectors.

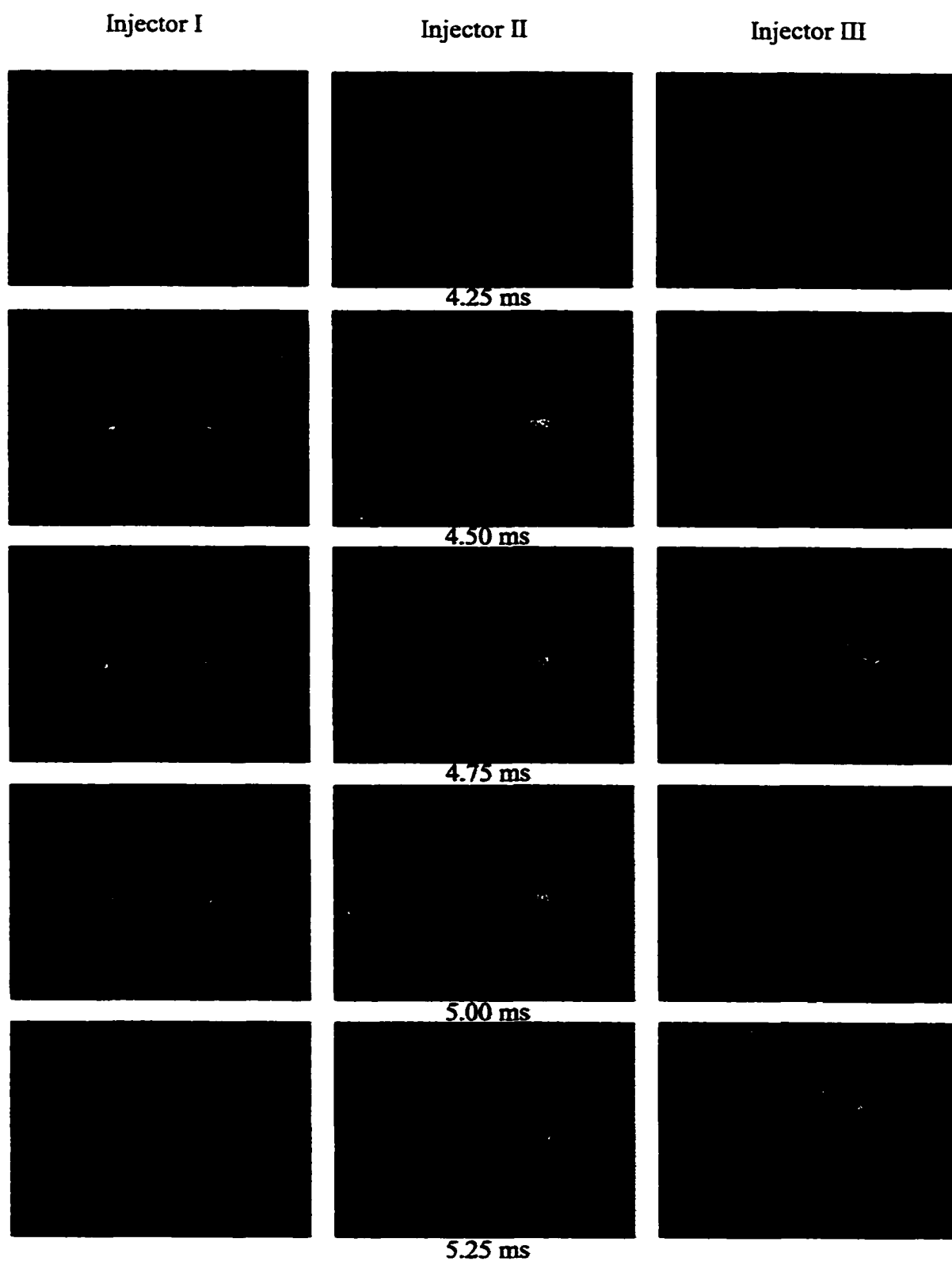


Figure 2.10 Time sequence of spray patterns at 300 kPa for three injectors.

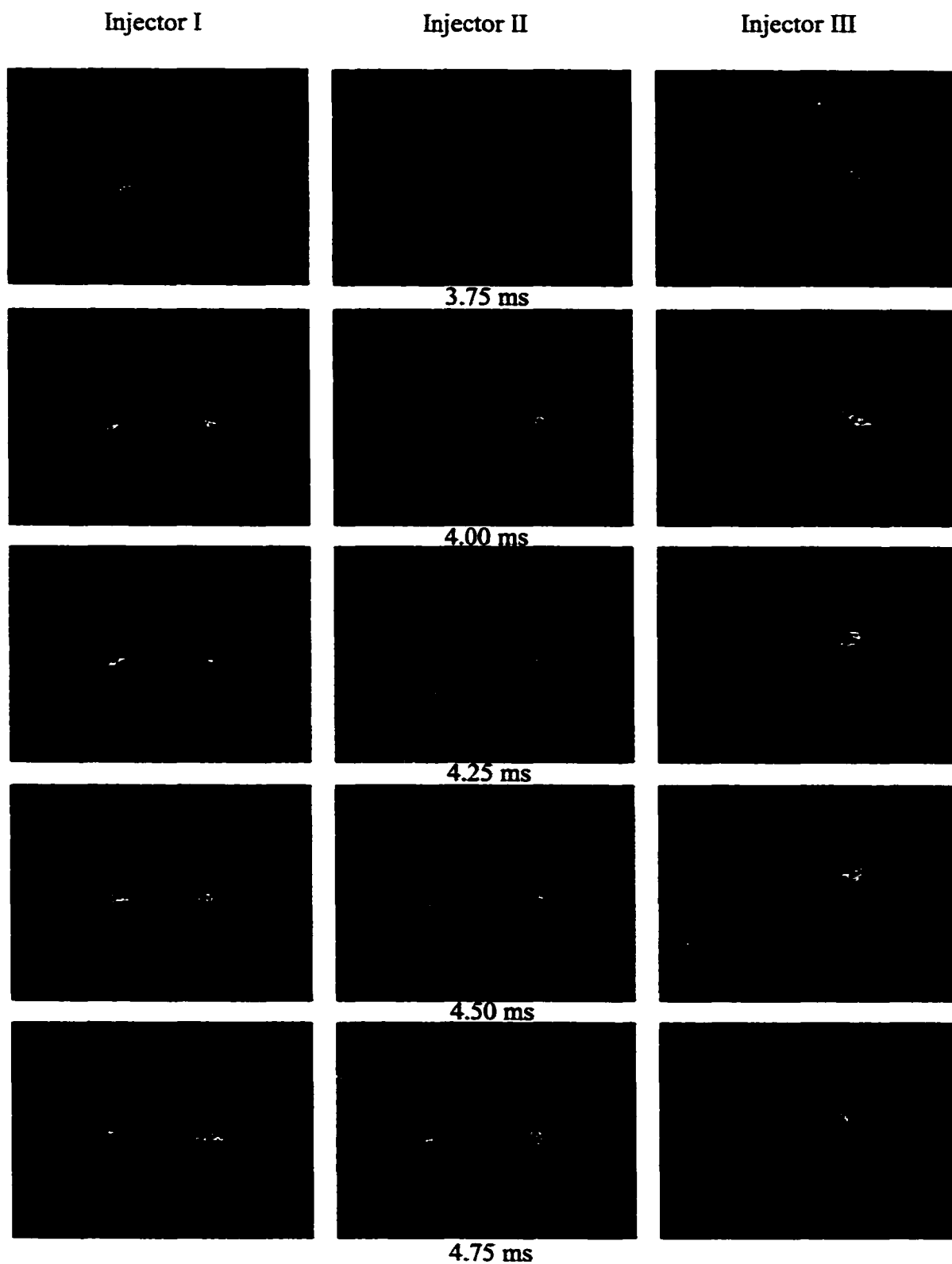
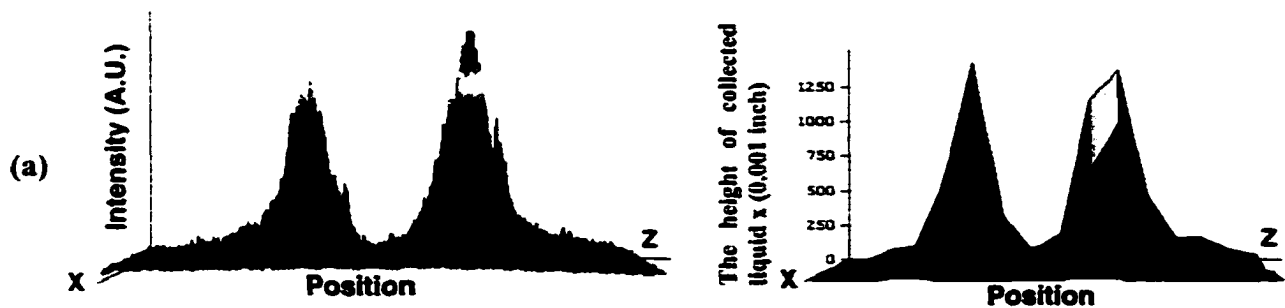


Figure 2.11 Time sequence of spray patterns at 500 kPa for three injectors.



There was available a two-dimensional spray accumulator for high-resolution fuel injector spray measurements. The device, situated below the fuel injector, uses an optical absorption technique to measure the volume of fluid collected over each detector of a 16x16 array. The three selected injectors were tested using this device, which yielded a measure of planar mass flux distribution. To compare the PLIF data with the mass flux accumulator the PLIF average images are summed over the trigger delay time sequence. This provides a measure of the total mass passing through the laser light sheet during an injection event. The comparative results are shown in Figure 2.12, with accumulator results on the right and PLIF results on the left-hand side. The injector pressure differential was 300 kPa for both PLIF and accumulator tests. The mass distribution is measured effectively in the pixel plane of the fluorescent images, the well-targeted injector in the top row (injector I) and the unstable injector at the bottom (injector III). The PLIF mass axis is drawn as a relative scale. The vertical axis of the accumulator shows the height of the collected fluid in the array cells. The PLIF method does capture the accumulated mass distribution peaks for each of the three injectors. The double peaked mass distribution is found for the two well-targeted injectors, and the single peak is found for the unstable injector including the correct position for the peak in the sample plane. The PLIF method can be used to interpret if the injector is providing the desired spatial fuel mass distribution.



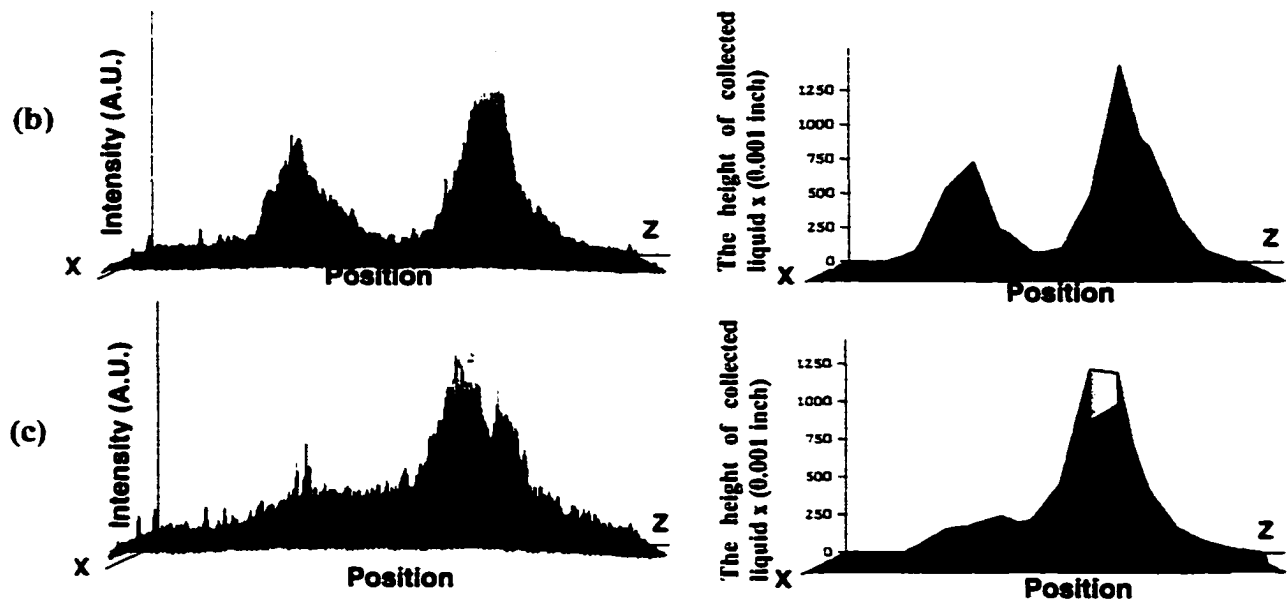


Figure 2.12 PLIF mass distribution compared with the accumulator results for (a) injector I, (b) injector II, (c) injector III.

These experiments have demonstrated a refined, time-dependent technique for evaluating liquid fuel spray mass distribution as provided by low-pressure fuel injector designs. The results particular to the fuel injectors studied may be summarized in four points:

- (1) An unstable “wobble” was clearly observed in the static injector spray field as recorded in shadowgraph images.
- (2) The spray instabilities observed were apparently due to small, internal geometry differences between the three injectors.
- (3) Ensemble average PLIF fluorescent intensity images were able to display the evolving structure of spray mass distributions.
- (4) The PLIF results are shown to provide semi-quantitative spray mass distributions when compared to another mass flux measuring technique.

### **2.3. Fluorescence and Absorption Spectra of Dyes for Use in Fuel Spray Studies**

Spectroscopy is a technique utilizing optical instruments to measure the absorption, emission, or scattering of electromagnetic radiation by atoms or molecules. It was noted that there is very limited information about the absorption and emission properties of dye-fluid combinations for fuel spray applications and the selection of the suitable combinations according to the laser type. Methods of absorption and emission spectroscopy were applied to different dye-hydrocarbon combinations to characterize various fluorescent dye and working fluid combinations, and to select optimal laser excitation and fluorescent emission wavelengths for later droplet and spray experiments. Specifically, the database is expanded by the reporting of absorption and fluorescence spectra and other relevant properties of the fluid combinations.

#### **2.3.1. The Selection of the Laser Dyes and Working Fluid**

Gasoline is the obvious fluid for spark ignition automotive engine applications, but it suffers from several drawbacks for quantitative PLIF use. Gasoline is a complex mixture of aliphatic and aromatic compounds, the blending of which varies from manufacturer to manufacturer. The manufacturers also vary the composition of gasoline from summer to winter. Gasoline exposed to the atmosphere is continuously changing its chemical composition, as lighter constituents preferentially evaporate over heavier compounds. Gasoline contains numerous additives, which exhibit degrees of fluorescence complicating the interpretation of the PLIF signal; see Itoh et al. (1995). For these reasons, it was decided to work with a pure fluid. A simple aliphatic hydrocarbon such as n-Octane or n-Heptane would be a suitable candidate. Since n-Heptane is an automotive standard (SAE J1832), and since part of the purpose of this work is to identify solvent

effects on PLIF spectra, n-Hexane, n-Heptane, and n-Octane were selected as fluid candidates. In order to make comparisons with published results, a fourth fluid, Cyclohexane, was chosen as a reference. All four solvents were obtained from Fisher Scientific, and were of spectroscopic grade. The four pure fluids exhibit negligible fluorescent signals when excited by photons in the visible-to-ultraviolet (UV) spectral range. The dyes, POPOP, Anthracene, BBQ, LD390, PPO, and Naphthalene, were frequently used in the studies on the dye lasers, but Toluene, Methanol or Dioxane have also been used as solvents in previous studies, e.g., Kotzubanov et al. (1968) and Bos (1981). Telle and Huffer (1981) used BBQ-Cyclohexane solution and Zeigler and Hudson (1980) used PPO-Cyclohexane solution in the development of the dye lasers. However, they did not report the absorption and emission spectra of these solutions.

Selection of the fluorescent dye is a critical element of a quantitative PLIF system. An ideal dye candidate would be highly soluble, have strong absorption and emission coefficients, a large Stokes shift, see Berlman (1965), and minimal toxicity effects. Since this work is intended for an industrial application, it is highly desirable that a commercially available (pulsed) laser light source be used, i.e., the selected dye should be pumped with an off the shelf laser. Noting the fact that the candidate working fluids are non-polar, aliphatic hydrocarbons, the chosen dyes should also be non-polar to improve solubility. Other factors are relevant to the dye selection process; for example, it is more expensive to work in the UV realm (quartz optics needed); and, frequency quadrupling of an Nd-YAG laser is less efficient and more expensive than frequency tripling. It is preferred for the dye to be pumped in the near UV, and the emission to be in the visible-to-near UV range, allowing the use of inexpensive optics made of BK-7 type

glass. After perusal of the dyes commercially available (Exciton Inc. and Lambda Physik Inc.), a selection matrix of laser sources and possible dyes was assembled, as shown in Table 2.2. Included in this table are two common substances, Anthracene and Naphthalene, which are not laser dyes, but do fluoresce, and occur naturally in gasoline. Nitrogen lasers have limited power, and can be excluded from consideration. The dye DMT was excluded as being too far in the UV, and TMQ,  $\alpha$ -NPO, and PBBO were excluded as overlapping other dyes. The DPS and Stilbene 420 were excluded after mixing the solutions indicated negligible solubility in the chosen fluids. The samples of PPO, BBQ, LD390, and POPUP were obtained from Exciton Inc.; Adrich Chemical provided the Anthracene and Naphthalene materials.

Table 2.2 Laser excitation-dye combinations

Laser	Wavelength (nm)	DMT	Naphthalene	TMQ	PBO	PBBO	LD390	$\alpha$ -NPO	PBBO	DPS	POPUP	Stilbene 420	Anthracene
KrF Excimer	248	x			x	x							
Nd-Yag 4th harmonic	266			x	x	x							
XeCl Excimer	308			x	x	x		x	x	x	x	x	
N <sub>2</sub>	337			x	x	x	x	x	x	x	x	x	
XeF Excimer	351					x				x			
Nd-Yag 3rd harmonic	355					x	x			x		x	

Excitation wavelength from absorption profile in Berlman (1965),

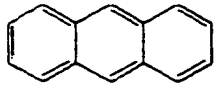
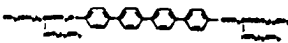
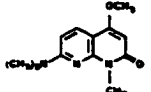
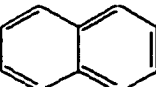
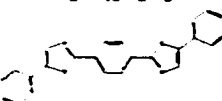
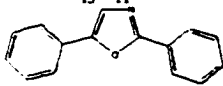
Selected dyes,

X Excitation wavelength from commercial datasheets, see Exciton Inc. (1992).

Table 2.3 shows the dye properties and solvent combinations. When the solutions of POPOP were prepared in Cyclohexane, n-Hexane, n-Heptane, and n-Octane, it was observed that POPOP did not dissolve in the solvents completely. Since the same

concentration for all POPOP solutions could not be obtained, only the POPOP-Cyclohexane solution results are reported in this study. Before giving details of experimental setup and experiments, general safety concepts for dyes/solvents and solutions are introduced in the next section.

Table 2.3 Fluorescent dye properties and solvent combinations

Dye	CAS number <sup>2</sup>	Chemical formula & Chemical Structure	Synonyms	Molecular weight	Solvent	Concentration x 10 <sup>-3</sup> [mol/l]
Anthracene	120-12-7	$C_{14}H_{10}$ 	-	178.23	Cyclohexane	1
					Octane	1
					Heptane	1
					Hexane	1
BBQ	18434-08-7	$C_{48}H_{66}O_2$ 	4,4'-Bis-(2-butyl-oxy)-p-quaterphenyl	675.05	Cyclohexane	1
					Octane	1
					Heptane	1
					Hexane	1
LD390	57980-10-6	$C_{12}H_{15}N_3O_2$ 	7-dimethylamino-1-methyl-4-methoxy-8-azaquinolone-2	233.27	Cyclohexane	1
					Octane	1
					Heptane	1
					Hexane	1
Naphthalene	91-20-3	$C_{10}H_8$ 	-	128.18	Cyclohexane	1
					Octane	1
					Heptane	1
					Hexane	1
POPOP	1806-34-4	$C_{24}H_{16}N_2O_2$ 	1,4-Di[2-(5-phenyloxazolyl)]benzene	364.4	Cyclohexane	0.1
PPO	92-71-7	$C_{15}H_{11}NO$ 	2,5-Diphenyloxazol	221.26	Cyclohexane	1
					Octane	1
					Heptane	1
					Hexane	1

<sup>2</sup> CAS number is the Chemical Abstracts Service registry number assigned by the Chemical Abstracts and serves as a unique identifier for the compound.

### **2.3.1.1. Important Concepts in Handling, Storing, and Disposing of Dyes, Solvents, and Solutions**

Most of the time, the exact toxicity information of dyes is not well known. Some dyes might have mutagenic and carcinogen effects according to animal experimentation data. Therefore, most dyes should be considered dangerous chemicals and all safety precautions should be taken when handling dyes. General safety concepts are emphasized in handling, storing, and disposing of dyes/solvents and solutions in this section.

When prepared solutions contain very small quantities of dyes, the worker must be concerned not only with the possible health hazards of dyes but also the possible health hazards of solvents. Since almost all solvents are extremely flammable liquids, a small fire extinguisher should be installed near the working area. Solvents must be kept away from ignition sources and oxidizing materials.

Solvent and dye should be mixed at least thirty minutes to dissolve the dye completely. To obtain homogenous solutions, a magnet-stirrer may be added to the mixture and the container is mounted on a swirling magnetic field table. After mixing, no floating dye particle should exist in the mixture. Once mixed, solutions should be stored in unbreakable containers and labeled clearly with the name of dye, solvent, the concentration of solution, and the most important hazards of the mixture.

Safety eyewear and impervious gloves must always be worn during experiments. An eyewash fountain should be located within a walking distance of 100 feet from the working area. It is strongly recommended to have a safety shower in the working area. Disposable laboratory coat or coveralls must be worn when handling and mixing dyes or cleaning up spills.

Work areas should be cleaned carefully after experiments. Gloves and safety eyewear should be worn when cleaning up spills. If the spill is small (less than 500 ml), it can be cleaned up with a noncombustible absorbent material. If the spill is more than 500 ml, area health and safety personnel should be called for assistance. People should be kept out of the area where a spill occurred. If a worker is exposed to dye powders, health and safety personnel should be notified immediately.

Waste solutions should be kept in approved waste containers and labeled. Appropriate types of waste containers can be learned from the Environmental, Safety and Health (ES&H) team in most university or industrial laboratories.

Dyes and dye solutions should be transported in double containers. Containers should be impact-resistant. An absorber material should be inserted in the space between the inner and outer containers. Both containers should be sealed and labeled.

Other important concepts can be summarized as follows:

- Workers should learn possible toxicity and flammability specifications of dyes/solvents from Material Safety Data Sheets (MSDS).
- Where dyes are in use, workers should not eat, drink, smoke, or store food, beverages, and smoking materials.
- Caution signs should be posted at entrances and in work areas.
- If dyes are in powder form, respirators should be used and a laboratory fume hood should exist in the area where dyes are handled.
- When dye solutions are handled, mechanical pipeting aids should be used.
- Solvent and solution containers should be closed firmly.
- Solvents and solutions should be stored in a cool, dry, and well-ventilated place.



- Hands must be washed after handling dyes/solvents and solutions.
- Articles contaminated with dyes should be stored separately from those that are not.

### **2.3.1.2. The Toxicity and Health Hazard Information of Current Dyes/Solvents**

This section summarizes possible hazard information of current solvents and dyes. The information for solvents was gathered from Occupational Safety and Health Administration (OSHA) website (<http://www.osha.gov/>), Lewis (1992), and Brackmann (1985). The information for dyes was gathered from manufacturers' material safety data sheets (MSDS), <http://hazard.com/msds/> website, and Lewis (1992). Detailed information on hazards, medical test data, first aid, ecological effects or disposal considerations can be obtained from National Institute for Occupational Safety and Health (NIOSH), Occupational Safety and Health Administration, manufacturers' MSDS, Ecological and Toxicological Association of Dyes and Organic Pigments Manufacturers (ETAD) or Lewis (1992).

All solvents in this study are extremely flammable liquids and should be kept away from heat sources, sparks, or open flames. Since solvents' vapors are denser than air, they may travel along the ground. Vapors may be ignited at a distant location. Solvent containers should be stored in a well-ventilated place. Vapor/air mixtures explode above a temperature flash point. Especially, n-Hexane and n-Octane give very dangerous fire and explosion hazard when exposed to heat. Current solvents release toxic gases in a fire. Cyclohexane, n-Heptane and n-Hexane should be kept away from strong oxidizers. Static discharges may ignite Cyclohexane.

The inhalation of solvents' vapors and skin contact with solvents should be avoided. Cyclohexane may irritate eyes and mucous membranes. High doses of Cyclohexane inhalation may cause dizziness, nausea, vomiting, and poor coordination. Cyclohexane is a fat solvent and thus chronic Cyclohexane exposure to skin may cause a dry, scaly, fissured skin. Short-term inhalation of n-Octane may cause irritation, nausea, difficulty in breathing, headache, drowsiness, and symptoms of drunkenness. High doses of n-Octane inhalation may cause nerve damage. Irritation and blisters may occur due to the skin contact with n-Octane; it is also an eye irritant. Short-term inhalation exposure to n-Heptane may cause dizziness, nausea, incoordination, stupor, loss of appetite, and a gasoline taste in the mouth. Redness and blistering occur in case of skin contact. High airborne concentrations of n-Heptane cause eye irritation. Drying, cracking, and dermatitis may be observed when the skin is repeatedly contacted with n-Heptane. Short-term exposure to n-Hexane may cause dizziness, nausea, confusion, headache, and irritation of the eyes, nose, throat and skin. Gastrointestinal irritation with nausea, vomiting and diarrhea may occur due to ingestion of n-Hexane. Long-term inhalation may produce central nervous system depression including muscle weakness, visual disturbances, or hallucinations.

The dust deposition of current dyes in dry powder form should be prevented, since finely dispersed particles may form explosive mixtures in air. Adequate ventilation should be provided in the working area to keep airborne concentrations low. Current dyes are combustible substances when exposed to heat or ignition sources. Toxic gases such as carbon dioxide, carbon monoxide, or nitrogen oxides could be released in a fire.

The toxicological properties of POPOP are not well known. It is essential to take all safety precautions in handling of this substance. Inhalation, digestion, skin, and eye contact should be avoided. POPOP may cause eye irritation and digestive track irritation. Skin irritation or dermatitis may be occurred due to the repeated contact with POPOP. The health hazards of chronic POPOP exposure have not been fully investigated. Skin and eye contact with Anthracene and Naphthalene should be avoided. Anthracene and Naphthalene may cause eye irritation, skin sensitization and irritation, or an allergic reaction. Ingestion of these substances may cause gastrointestinal irritation with nausea, vomiting, and diarrhea; inhalation of these substances may cause respiratory track irritation. Carcinogen effects for Anthracene are not well known. The material safety data sheet from Aldrich Chemical indicates Anthracene as a possible tumor promoter in cases of chronic exposure. It is strongly recommended to use NIOSH approved respirators when handling Anthracene. The substances PPO, BBQ, or LD390 may cause eye, skin, and respiratory track irritation. In case of ingestion of these substances, gastrointestinal irritation with nausea, vomiting, and diarrhea may occur. Chronic exposure to PPO may cause liver and kidney damage.

Very low dye concentrations in solutions might minimize possible health effects. Current solvents should not be disposed of in the sink. Solvents' or dyes' waste should be stored in appropriately labeled containers and disposed by specialized contractors handling hazardous chemical waste. These dangers indicate the care that must be taken when designing and implementing the experiments.

### **2.3.2. The Development of the Experiment and the Instruments of the Experimental Setup**

The experimental apparatus for the absorption and emission measurements was based on a 0.5 meter focal length Czerny-Turner type imaging spectrograph made by Acton Research Corp. (SpectraPro 500I). A 1200 groove/mm dispersion grating with a 300 nm blaze angle was used in this work. The manufacturer claims a 0.15 nm band pass performance using a 100  $\mu\text{m}$  slit width for this system. A 16 bit data collection system (Acton SpectraCard SC-1), photomultiplier tube (Hamamatsu R928), computer controlled high voltage power supply (Acton PHV-400), and a sample chamber (Acton SC-447) were also used. A light source with significant UV output is required for these measurements. A Xenon arc lamp (Olympus ILX-6300), modified for use with an enhanced UV bulb (ILC300), was used for this purpose.

Spectrometer system calibration was performed using a PenRay Hg lamp (MS-416). Absolute wavelength alignment was verified to be within 0.1 nm for the Hg lines between 296.5 nm and 435.8 nm. Measurements were made of the system spectral resolution as a function of spectrometer slit settings, at wavelengths of 253.7, 365.0, and 435.8 nm. The spectral resolution, full width at half-maximum (FWHM), was greater than 0.1 nm for a 10  $\mu\text{m}$  slit width, 0.2 nm for a 50  $\mu\text{m}$  slit width, and 0.25 nm for 100  $\mu\text{m}$  slit width, at these wavelengths.

The experimental configuration shown in Figure 2.13 was used for the optical absorption measurements. In this figure, PMT refers to the photomultiplier tube. Light from the Xenon lamp was brought to the entrance slit, through the monochromator and exit slits, then focused on the quartz sample cuvette.

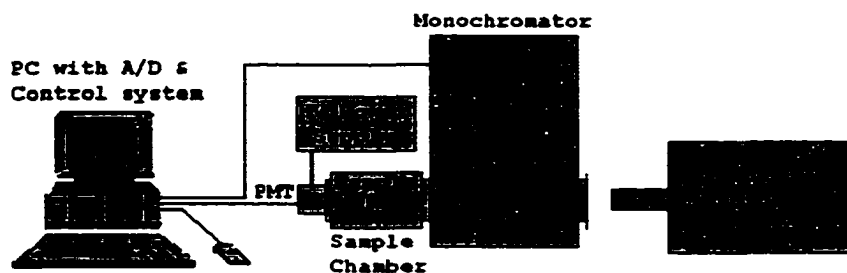


Figure 2.13 Experimental setup for the optical absorption measurements.

The experimental procedure was based on a radiometric technique, which measures the change in light intensity passing through the sample cuvette when filled with pure solvent ( $I_0$ ) as compared to the cuvette filled with the solvent plus fluorescent dye ( $I$ ). The transmittance of light passing through a solution is given by Beer Lambert law; see Wayne (1970),

$$\log_{10} \left( \frac{I_0}{I} \right) = \epsilon Cd \quad (2.9)$$

where,  $C$  is the molar dye concentration,  $\epsilon$  is the extinction coefficient, and  $d$  is the optical path length. Using this technique, a measurement involved scanning the monochromator through a wavelength region when the sample cuvette was filled with the pure solvent, then repeating this process for the solvent plus dye solution. The logarithmic ratio of these intensity scans, divided by the (known) concentration and optical path length, gives the molar extinction coefficient. For these absorption measurements, the entrance and exit slit settings were  $10 \mu\text{m}$ , and the photomultiplier tube was operated at 650 V. A 1000 ms integration time was used for the SC-1 A/D

board, and the wavelength range covered was 250–400 nm. In order to estimate the uncertainty in the incident light intensity, ten scans on a pure solvent filled cuvette were made and the data was used in an uncertainty analysis.

The absorption spectra experimental setup was re-configured by adding a second monochromator, as shown in Figure 2.14, in order to measure emission spectra. This unit, made by Instruments SA Inc. (H-10 type), was used to provide a quasi-monochromatic light source from the UV lamp. Measurements of the spectrum of the light from the ISA spectrometer, using a 0.5 mm slit width, indicated a FWHM of less than 4 nm, for selected wavelengths of 248, 266, 308, 313, 351, 355, and 365 nm. These wavelengths represent commercially available laser and Hg lamp lines, and serve as excitation sources for the fluorescent samples.

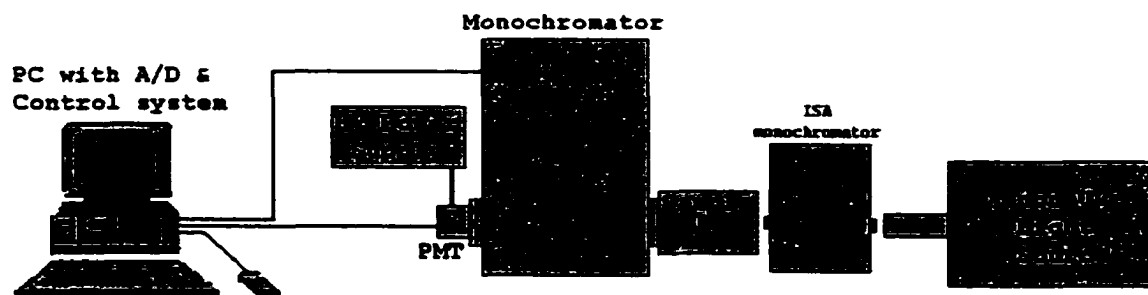


Figure 2.14 Experimental setup for the emission measurements.

Emission spectra are sensitive to the excitation wavelength. Examination of the measured absorption spectra led to the following test matrix of dye/excitation wavelengths shown as Table 2.4.

Table 2.4 Corresponding values for absorption maxima and excitation wavelengths

Dye	Absorption Maximum (nm)	Excitation Wavelength (nm)
Naphthalene	275	266
PPO	302	308
BBQ	307	308
LD390	355	351, 355
Anthracene	356	351, 355
POPUP	360	351, 355

The dyes, Naphthalene, PPO, POPUP and Anthracene were also tested in Cyclohexane at excitation wavelengths of 265, 313, 365, and 365, respectively, in order to compare with results in Berlman (1965).

### 2.3.3. Discussion of Results

#### 2.3.3.1. Absorption Measurements

Figures 2.15-2.20 show the absorption spectra for POPOP, Anthracene, BBQ, LD390, PPO, and Naphthalene, respectively. The molar dye concentrations in the Figures are  $10^{-4}$  [M] for POPOP and  $10^{-3}$  [M] for the other five dyes. The molar dye concentration of POPOP–Cyclohexane is less than the molar dye concentrations of the other solutions, because POPOP did not dissolve completely in the solvent. The concentration value for POPOP–Cyclohexane solution was obtained by evaporating the solvent from the solution and by weighting the residual dye mass. The vertical axes in the Figures indicate the extinction coefficient, which carries the dimensions, liter solvent per moles dye per centimeter path length.

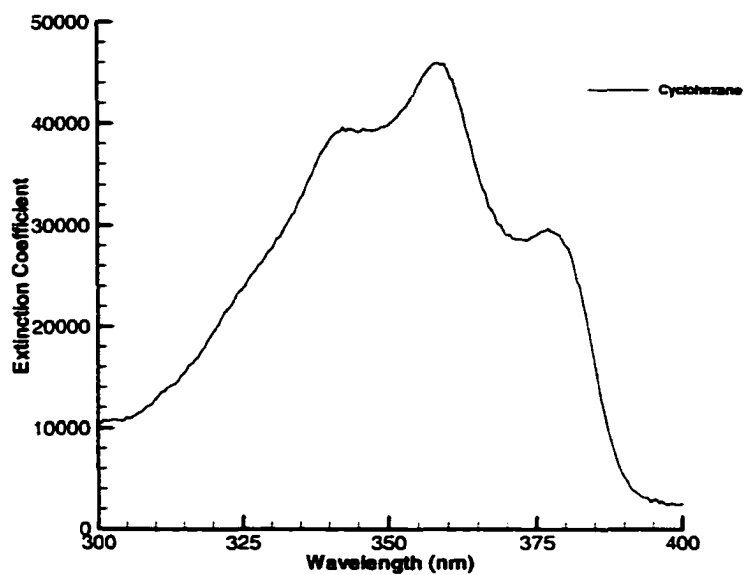


Figure 2.15 Absorption spectra for POPOP.

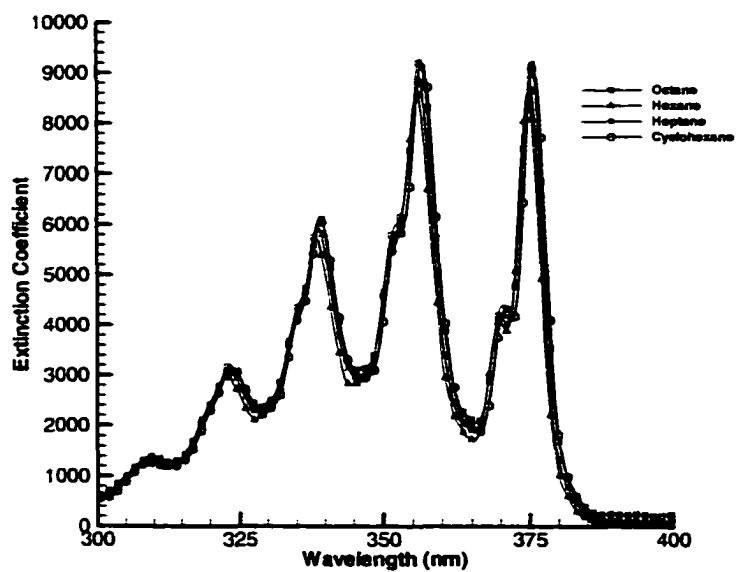


Figure 2.16 Absorption spectra for Anthracene.



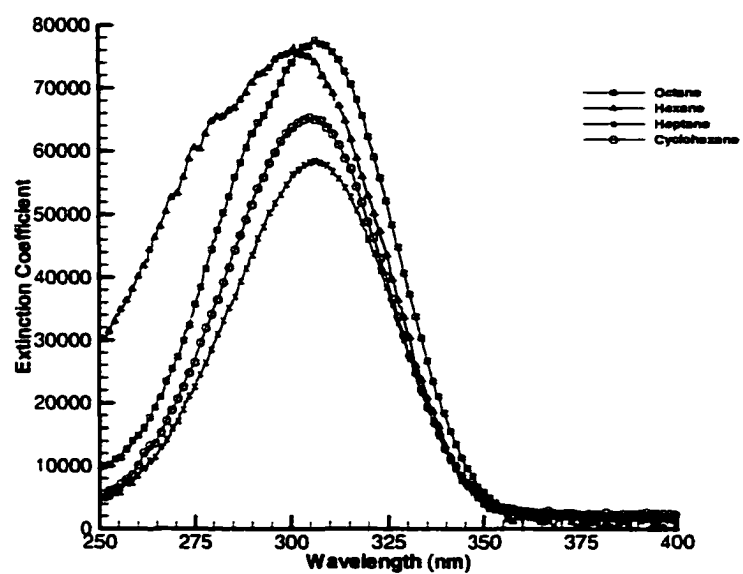


Figure 2.17 Absorption spectra for BBQ.

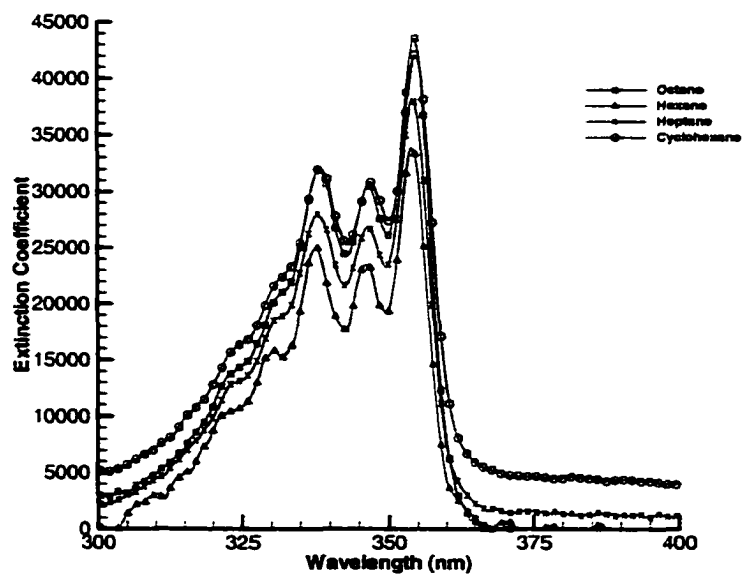


Figure 2.18 Absorption spectra for LD390.

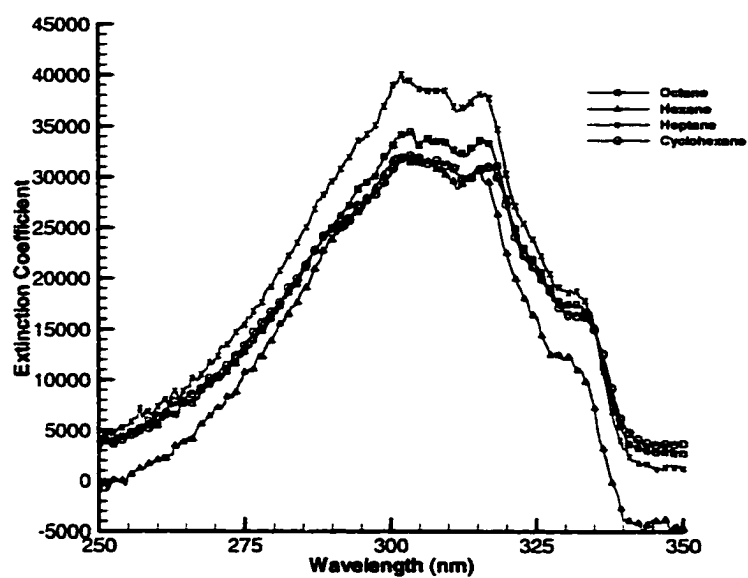


Figure 2.19 Absorption spectra for PPO.

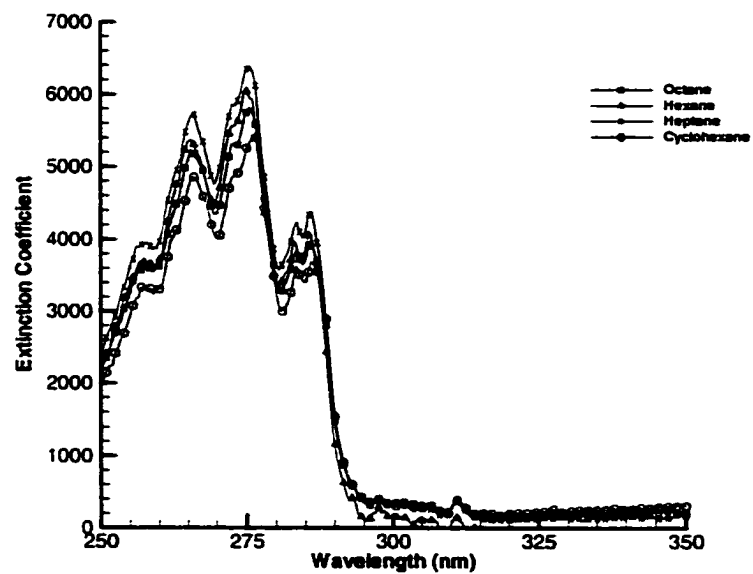


Figure 2.20 Absorption spectra for Naphthalene.

The fraction of transmitted light through an absorbing system is found by the relation

$$\frac{I}{I_0} = e^{-\alpha Cd} = 10^{-\epsilon Cd} \quad (2.10)$$

where  $\alpha$  is the absorption coefficient and  $e$  is the base, 2.71828. The relation between absorption and extinction coefficients is  $\alpha=2.303\epsilon$ . The extinction coefficient is calculated from the Beer Lambert law as follows:

$$\epsilon = \frac{1}{Cd} \log_{10} \frac{I_0}{I} \quad (2.11)$$

Since the extinction coefficient peak is around 355 nm wavelength for POPOP, Anthracene and LD390 in the Figures, these dyes are suitable for Nd-Yag 3rd harmonic laser applications. There is an obvious solvent effect<sup>3</sup> for BBQ, LD390, and PPO in that the extinction coefficient values are decidedly different for the four solvents used. The dyes, BBQ and PPO, are suitable for XeCl Excimer laser excitation, because their extinction coefficient peak is around 308 nm wavelength. BBQ gives the highest extinction coefficient values among six selected dyes. Naphthalene is a suitable dye for Nd-Yag 4th harmonic laser applications, because it has the extinction coefficient peak around 266 nm. The extinction coefficient values are low and the solvent effect is not very obvious for Naphthalene.

---

<sup>3</sup> Possible causes for the solvent effect are discussed in Berlman (1965), p11.

Error magnitudes in the dye concentration and intensities during the experiments are inevitable; therefore, an uncertainty analysis is presented. In the extinction coefficient calculation, three uncertainty sources should be taken into account: uncertainty from intensity, uncertainty from concentration, and uncertainty from path-length. The relative uncertainty in the extinction coefficient measurements is determined by applying a general uncertainty analyses to Equation (2.8) above, e.g., see Coleman and Steele (1999).

$$\frac{w_{\epsilon}}{\epsilon} = \left[ \left( \frac{l}{2.303 \log \frac{I}{I_0}} \right)^2 \left[ \left( \frac{w_I}{I} \right)^2 + \left( \frac{w_{I_0}}{I_0} \right)^2 \right] + \left( \frac{w_C}{C} \right)^2 + \left( \frac{w_d}{d} \right)^2 \right]^{1/2} \quad (2.12)$$

where the fractional concentration uncertainty,  $\frac{w_C}{C}$ , is calculated by

$$\frac{w_C}{C} = \left[ \left( \frac{w_m}{m} \right)^2 + \left( \frac{w_V}{V} \right)^2 \right]^{1/2} \quad (2.13)$$

In the equation (2.13),  $m$  is the mass of the dye,  $w_m$  is uncertainty of mass,  $V$  is the volume of the solution and  $w_V$  is the uncertainty of volume. It should be noted that the incident intensity uncertainty,  $w_{I_0}$ , value is obtained from the measured incident intensities,  $I_0$ , as a function of wavelength. The graphs of measured incident intensities for each solvent can be found in Appendix A. By assuming that the fractional incident intensity uncertainty,  $\frac{w_{I_0}}{I_0}$ , equals to the fractional intensity uncertainty,  $\frac{w_I}{I}$ , Equation (2.12) becomes

$$\frac{w_{\epsilon}}{\epsilon} = \left[ 2 \left( \frac{I}{2.303 \log \frac{I}{I_0}} \right)^2 \left( \frac{w_{I_0}}{I_0} \right)^2 + \left( \frac{w_C}{C} \right)^2 + \left( \frac{w_d}{d} \right)^2 \right]^{1/2} \quad (2.14)$$

The dominant term in Equation (2.14) is the intensity uncertainty for all dyes except Naphthalene. The maximum fractional extinction coefficient uncertainty for Naphthalene is 4.8%, whereas the fractional extinction coefficient uncertainty for the other five dyes is less than 2.8%. Extinction coefficient data were found for some of the dyes under study, and Berlman (1965) indicates results with a 10% experimental error.

Figure 2.21 shows the comparison of present absorption spectra with Berlman's results for POPOP, Anthracene, BBQ, and Naphthalene in Cyclohexane. In the Figures, the line with symbols shows Berlman's results and the solid line shows the present spectra results. As it can be seen from Figure 2.21, the graphs of the present results and Berlman's results are quite similar. The maximum percent difference is about 13% (Figure 2.21(d)), and the Berlman's results are thought to be accurate within  $\pm 10\%$ . It should be noted that the concentration values of the solutions in this study and Berlman's study are not same. The concentration values for the present study can be seen in Table 2.2 and the concentration values for Berlman's study can be seen in Table 2.4.

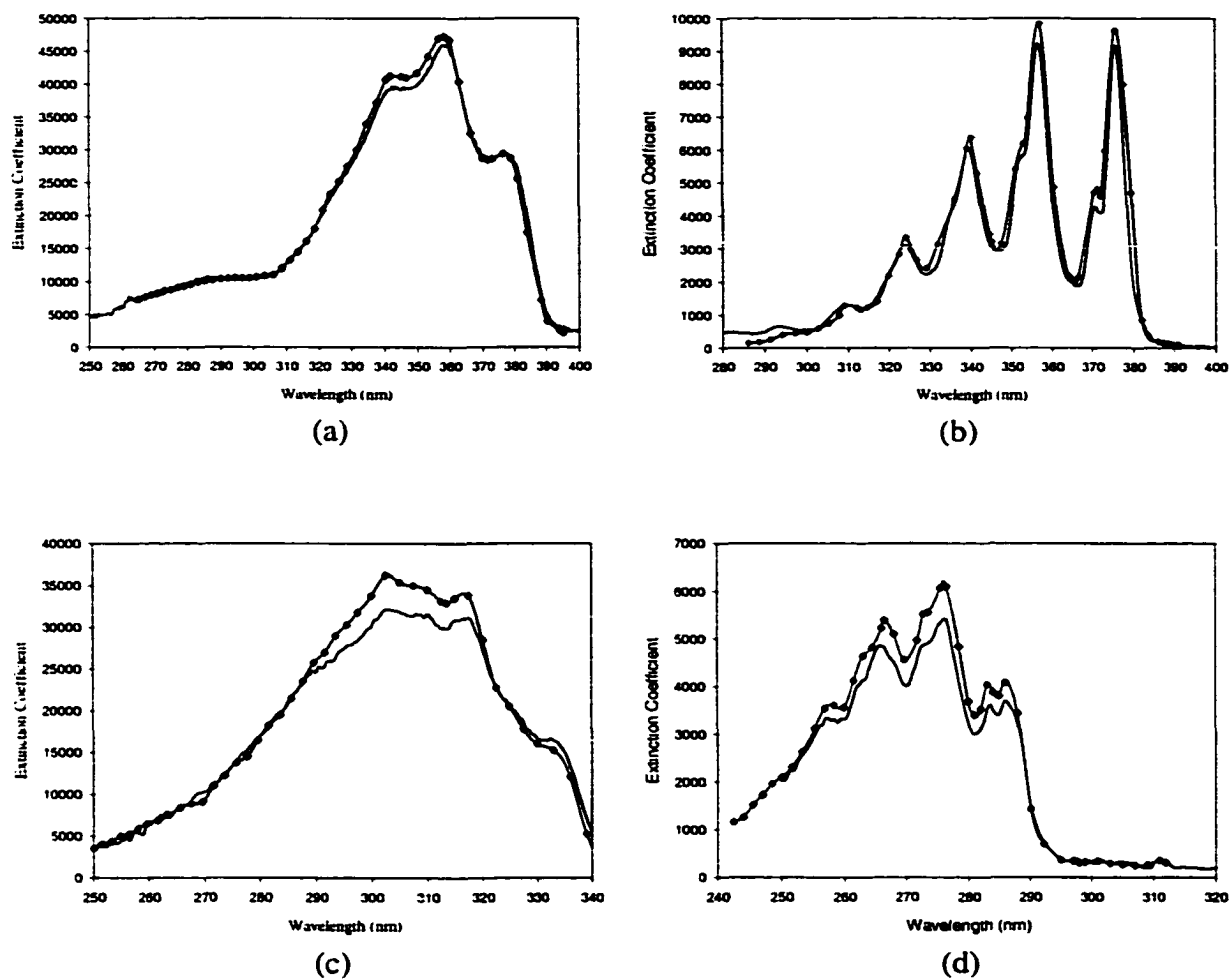


Figure 2.21 The comparison of present absorption spectra results with Berlman's results for (a) POPOP in Cyclohexane, (b) Anthracene in Cyclohexane, (c) PPO in Cyclohexane, (d) Naphthalene in Cyclohexane. The line with symbols shows Berlman's results and the solid line shows the present spectra results.

### 2.3.3.2. Emission Measurements

Figures 2.22-2.27 show emission spectra, intensity with arbitrary units (A.U.) versus wavelength, for POPOP, Anthracene, BBQ, LD390, PPO, and Naphthalene, respectively. The solvent effects, indicated in the absorption results discussion, are again displayed in the emission spectra. The peaks on the left side in Figures 2.22 and 2.26 occur due to the residual excitation photons at the excitation wavelengths. However, the position of the emission peaks does not depend on the excitation wavelengths. All dyes exhibit distinct separation between the excitation wavelength and the wavelength of emission peak. This separation provides for the simplification in the excitation wavelength filtering during the PLIF application.

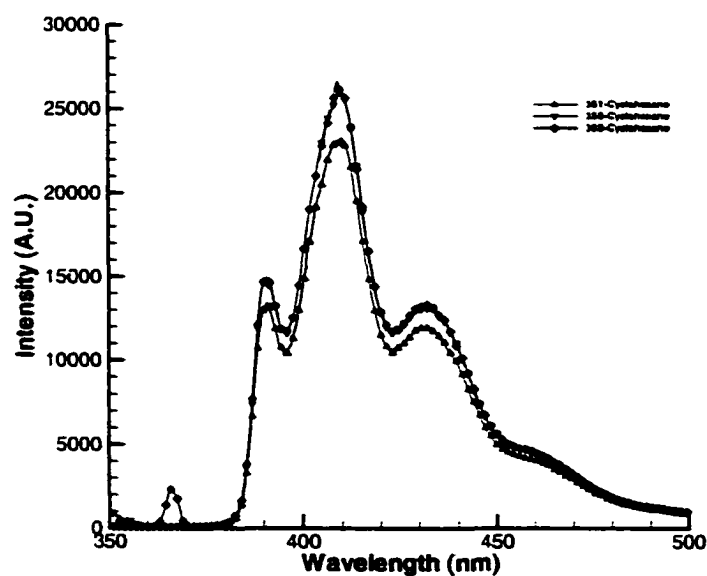


Figure 2.22 Emission spectra for POPOP.

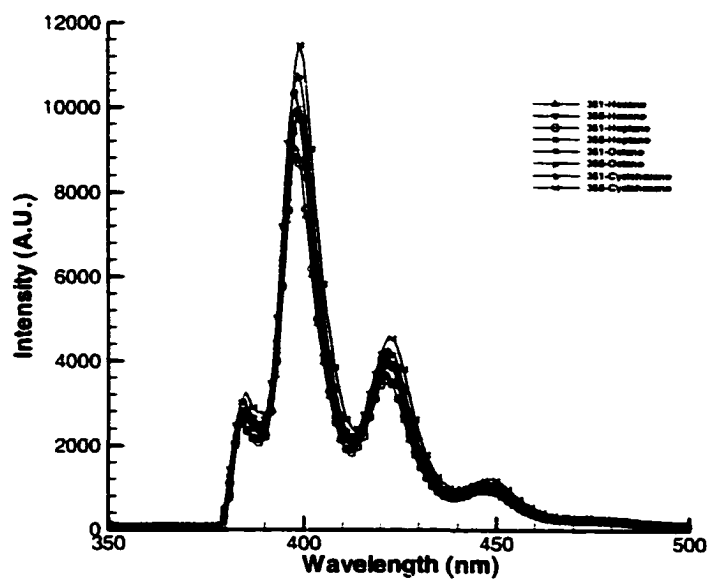


Figure 2.23 Emission spectra for Anthracene.

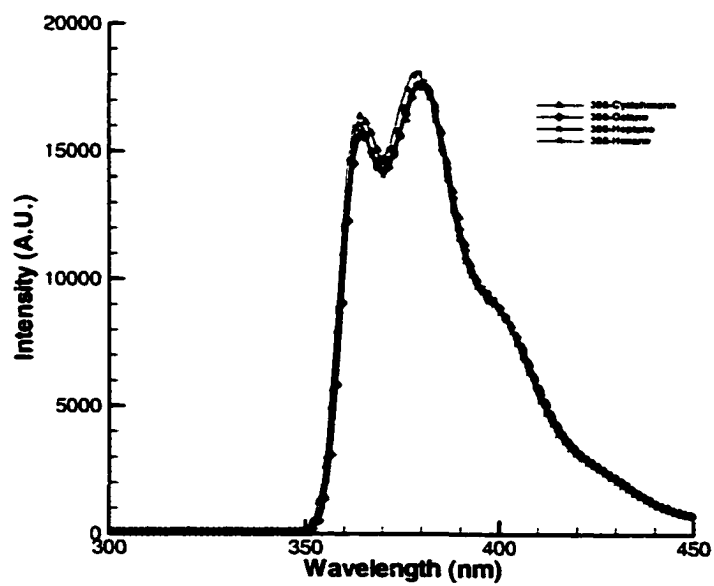


Figure 2.24 Emission spectra for BBQ.



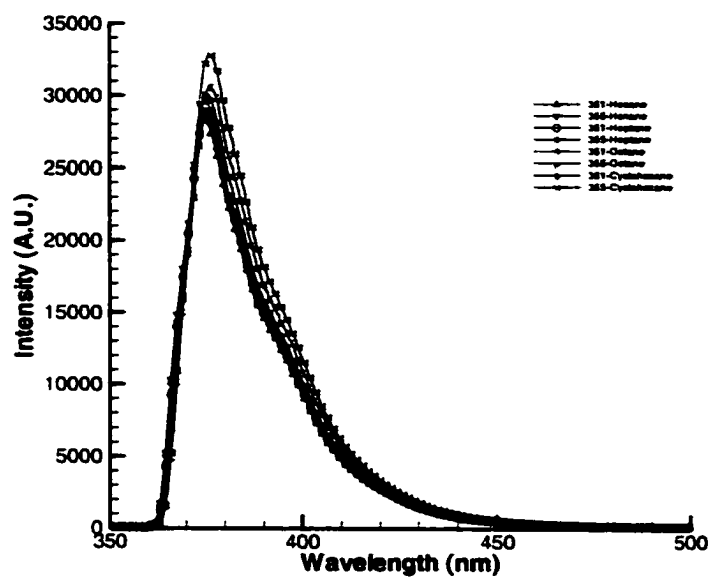


Figure 2.25 Emission spectra for LD390.

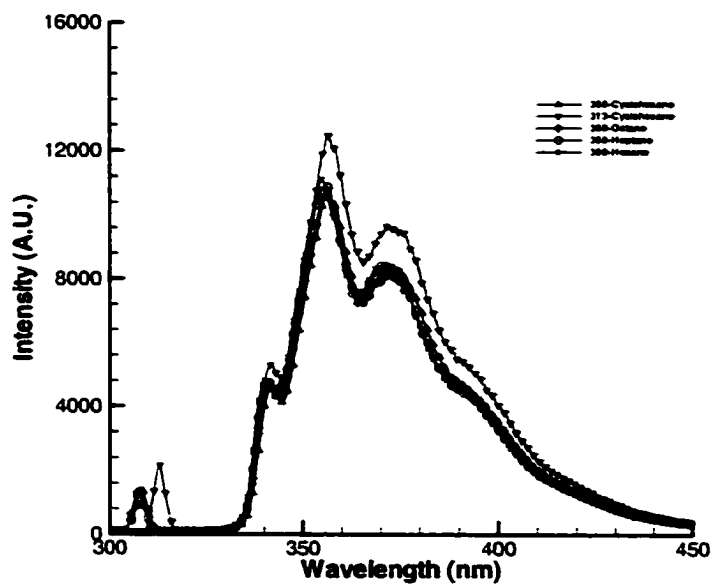


Figure 2.26 Emission spectra for PPO.

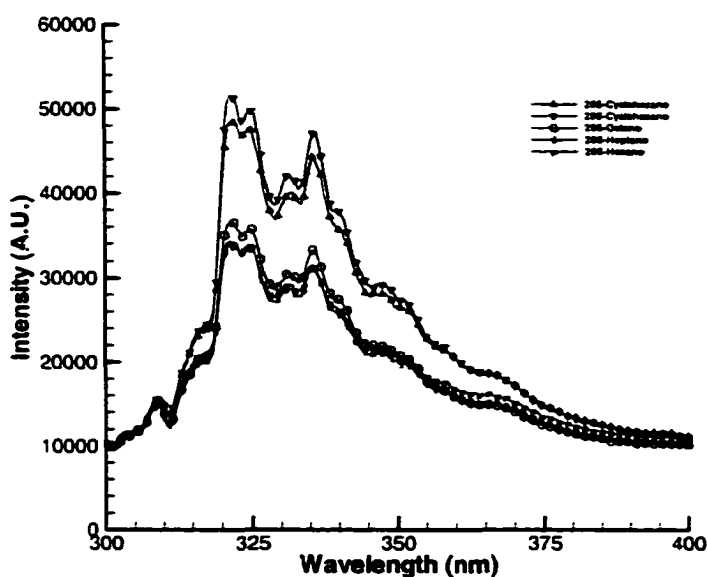


Figure 2.27 Emission spectra for Naphthalene.

Table 2.5 shows for comparison centroid wavelength values of the emission spectra with Cyclohexane as the solvent in the present study with centroid wavelength values in Berlman's study. As can be seen from the following table, the present centroid wavelength values are very close to Berlman's values. The centroid wavenumber value is defined as,

$$\nu_{cg} = \frac{\int \nu f(\nu) d\nu}{\int f(\nu) d\nu} \quad (2.15)$$

where  $f(\nu)$  is the measured emission spectra distribution function. By assuming  $f(\nu)d\nu = f(\lambda)d\lambda$ , the centroid wavelength is derived as follows:

$$\lambda_{cr} = \frac{\int f(\lambda)d\lambda}{\int \frac{1}{\lambda} f(\lambda)d\lambda} \quad (2.16)$$

Table 2.5 Comparison of centroid wavelength for the emission spectra

Dye	$\lambda_{cg}$ values in Berlman's study (nm), Berlman (1965)	$\lambda_{cg}$ values in the present study (nm)
PPO $\lambda_{exc}= 313$ nm	372.4 ( $C=0.902 \times 10^{-3}$ [M])	371.4
POPOP $\lambda_{exc}= 365$ nm	419.4 ( $C=0.027 \times 10^{-3}$ [M])	419.6
Naphthalene $\lambda_{exc}= 265$ nm	336.1 ( $C=7.333 \times 10^{-3}$ [M])	342.1
Anthracene	404.7 ( $\lambda_{exc}= 253.7$ nm) ( $C=1.683 \times 10^{-3}$ [M])	405.8 ( $\lambda_{exc}= 351$ nm and 355 nm)

The Stokes shift definition is based on the fact that the emitted light is composed of wavelengths longer than those of the absorbed light. A large Stokes shift is a good property for a fluorescent dye, since the signals can be more easily separated by detectors. If the Stokes shift is small, the self-absorption of the emitted photons decreases the fluorescent output intensity. Two different Stokes shift formulas are encountered in the literature (Berlman (1965) and Doroshenko et al. (1996)): one is the difference between the wave number of the line of symmetry and the wave number of the centroid value; and the other is the difference between the absorption band maxima wave number and the emission band maxima wave number. The latter formula was preferred in the present study. Table 2.6 shows the Stokes shift values of the present spectral results. Since the small Stokes shift values were obtained for LD390 and Anthracene, the use of these dyes may cause self-absorption problem.

Table 2.6 Stokes shift values

<b>Dye</b>	<b>Solvent</b>	<b>Stokes Shift (cm<sup>-1</sup>)</b>
Anthracene	Cyclohexane	2987.834
	Heptane	2964.259
	Hexane	2972.163
	Octane	2956.388
BBQ	Cyclohexane	6559.514
	Heptane	6257.500
	Hexane	6968.902
	Octane	6310.638
LD390	Cyclohexane	1613.000
	Heptane	1581.921
	Hexane	1546.318
	Octane	1577.586
Naphthalene	Cyclohexane	5217.685
	Heptane	5193.441
	Hexane	5259.437
	Octane	5193.440
POPOP	Cyclohexane	3542.717
PPO	Cyclohexane	5007.360
	Heptane	5062.092
	Hexane	4998.482
	Octane	4859.042

#### 2.4. Auxiliary Experiments: Droplet Generator and Quantum Efficiency

Exploratory experiments were designed to further the goal of finding a methodology to completely measure spray mass distribution. Only preliminary results were obtained, and these are reported here for completeness.

The single droplet experiments were planned to obtain droplet lensing information by visualizing individual droplets. The experimental layout for single droplet experiments is shown in Figure 2.28. Water was used as a working liquid in the preliminary

experiments. Figure 2.29 shows the jet breakup and droplet distortion for 50  $\mu\text{m}$  and 100  $\mu\text{m}$  orifice sizes.

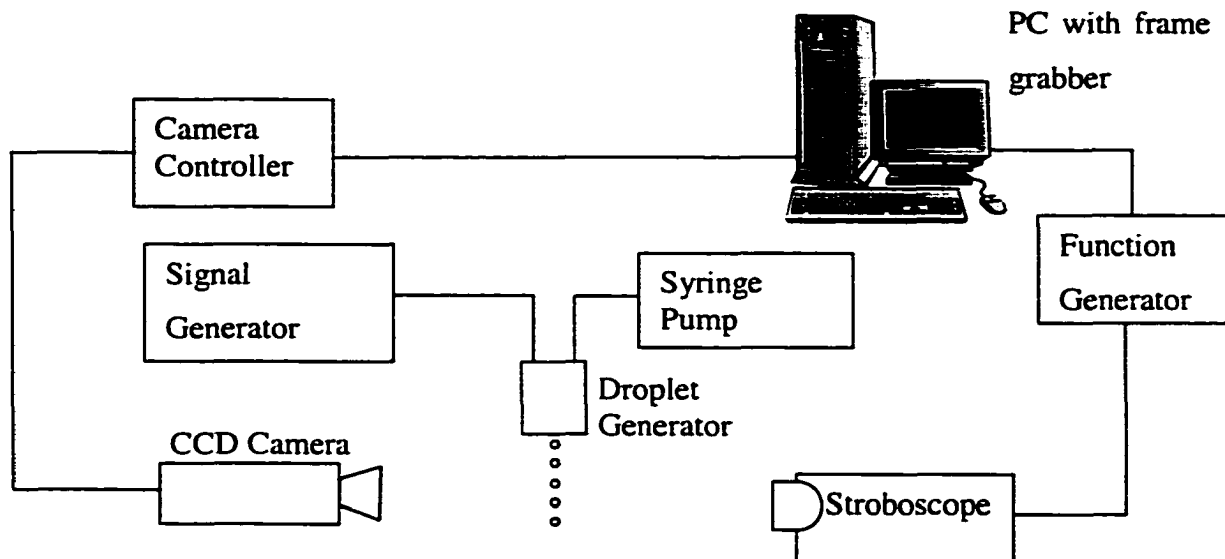


Figure 2.28 Schematic figure of the experimental setup for single droplet experiments.

Drop formation was obtained by using a monodisperse drop generator (Aerometrics MDG-100). The monodisperse drop generator has a piezoelectric element to generate acoustic waves, which drive the jet breakup. The droplet size was controlled by using different orifice sizes and by changing operating frequency of piezoelectric element. A syringe pump (kdScientific Inc., KDS 100) supplied a constant volumetric flow rate of liquid to the drop generator. Images were captured by an intensified camera (Xybion Corp., ISG350). The camera controller unit made by CoHU, Inc. (CoHU MPC) was used to control the intensified camera and the function generator made by Stanford Research Systems (DS345) was used to synchronize a stroboscope (Monarch Instruments, MVS 2612).

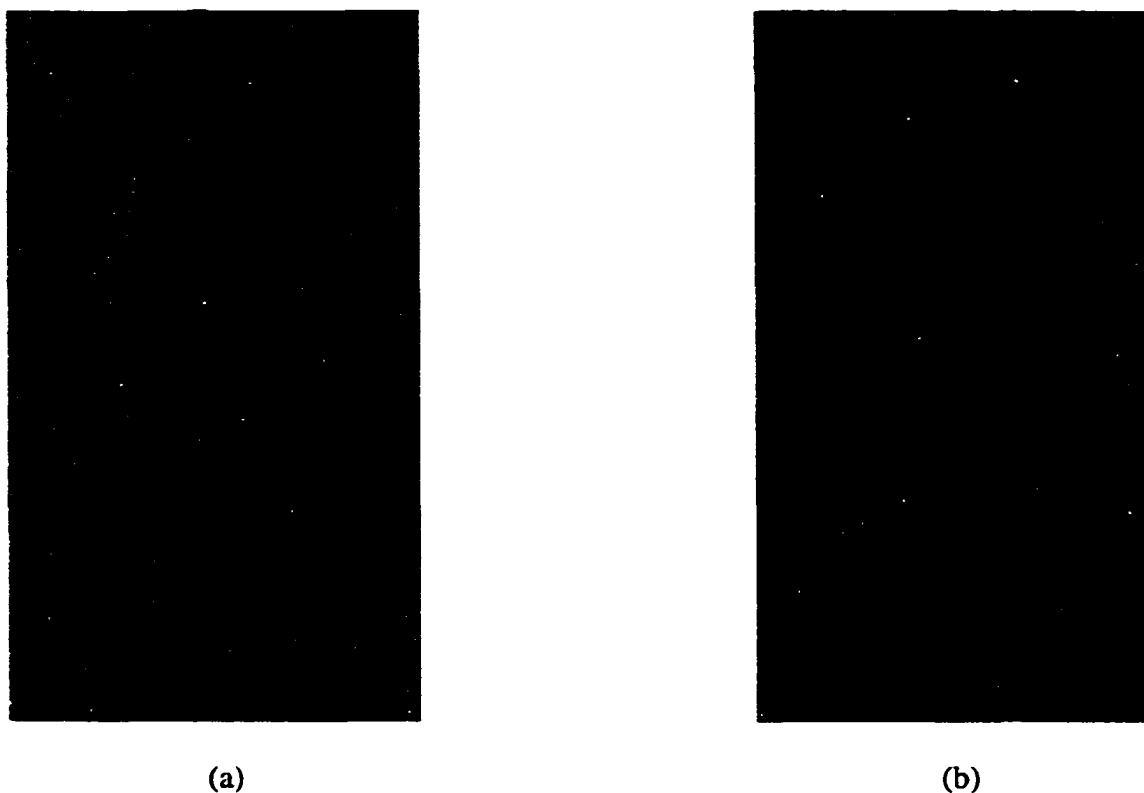


Figure 2.29 Visualization of water droplets (a) 50  $\mu\text{m}$  orifice size, (b) 100  $\mu\text{m}$  orifice size.

The motivation of quantum efficiency measurements was the lack of quantum efficiency information for fuel spray studies. The quantum efficiency (or the quantum yield) is defined as the ratio of the number of emitted fluorescent photons to the number of absorbed excitation photons. In the application of the PLIF technique, it is very desirable to use solutions with high quantum efficiency, hence minimizing the dye concentration.

A 6-inch diameter integrating sphere manufactured by Labsphere (IS-060-SL) was used for quantum efficiency experiments. The integrating sphere, which is a hollow sphere coated with a highly reflecting material, spatially integrates the input light flux.

The manufacturer claims that the reflectance of inner surface coating is 99% in the 350 nm to 1800 nm spectral region. Other components of the experimental setup were a Xenon arc lamp (Olympus ILX-6300), an achromatic lens, a photomultiplier tube made by Acton Research Corp. (PD438), and two monochromators: one made by Instruments SA Inc. (H-10 type) and the other one made by Acton Research Corp. (SpectraPro 500I). Experimental components are shown in Figure 2.30. The space between the Xenon arc lamp and the integrating sphere was covered during the experiments to prevent the intrusion of outside light. Figure 2.31 shows the schematic figure of the integrating sphere. The integrating sphere includes a diffusely reflecting baffle between the sample and the exit port to prevent the direct illumination of the photomultiplier tube by sample emissions.

The output of the Xenon arc lamp passed through the first monochromator to achieve wavelength selection. Since the inlet port of the integrating sphere was small, an achromatic lens was used to focus the light. A quartz sample cuvette was mounted across from the inlet port.

The photoluminescence (PL) quantum efficiency measurement method, which was defined by Mello et al. (1997) to measure quantum efficiency of highly scattering samples, was intended to provide quantum efficiency measurements for dye-liquid hydrocarbon solutions. Since Mello et al. (1997) reported a quantum efficiency value of Rhodamine 6G-ethanol solution as a standard, experiments were made by using Rhodamine 6G-ethanol solution in order to compare results before making experiments with dye-liquid hydrocarbon solutions.

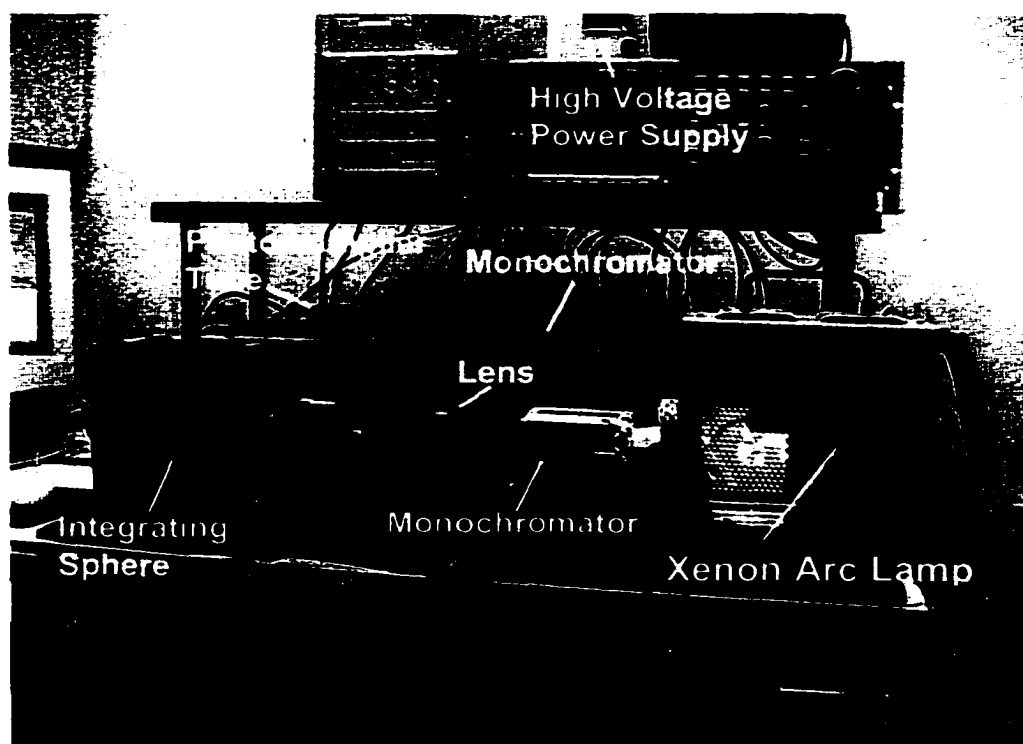


Figure 2.30 Quantum efficiency measurements experimental setup.

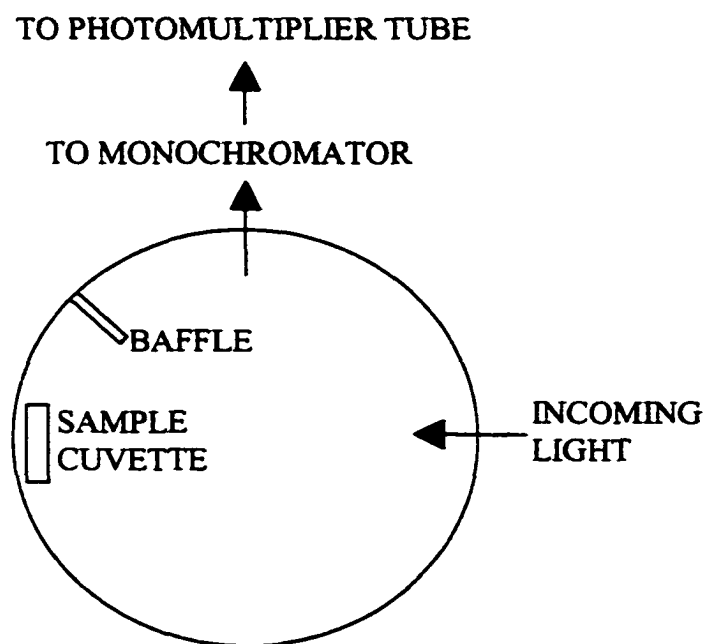


Figure 2.31 Schematic figure of the integrating sphere.



The PL quantum efficiency experimental procedure involved three stages. First, an empty sample cuvette was mounted onto the integrating sphere. The diffusely reflected incoming light was scanned by the second monochromator and detected by the photomultiplier tube. This stage is called experiment (a). For the second step, the sample cuvette was filled with  $10^{-4}$  [M] Rhodamine 6G solution and mounted into the integrating sphere. The incoming light was focused onto the sphere wall. The second step is called experiment (b). For the third step, the incoming light was focused on the solution filled sample cuvette. The third step is called experiment (c). The emitted and unabsorbed light was also scanned by the second monochromator and detected by the photomultiplier tube in the last two steps. For these PL quantum efficiency measurements, the entrance and exit slit settings were 800  $\mu\text{m}$ , and the photomultiplier tube was operated at 772 V. A 100 ms integration time was used for the data collection system (Acton Research SpectraCard SC-1). The excitation wavelength was 532 nm and the 450-650 nm wavelength range was scanned. Figure 2.32 shows the obtained spectra of Rhodamine 6G-ethanol solution for experiments (a), (b), and (c). The ordinate of the graph represents the product of the intensity and wavelength. The value of intensity by wavelength is proportional to the number of photons within a given wavelength interval. The sharp peak in each case refers to the detection of the excitation light. Emission profiles are the broader profiles at longer wavelengths. In each case, the amount of unabsorbed light is proportional to the area under the excitation profile. This area is called as L in subsequent equations. The amount of emitted light is proportional to the area under the emission profile in experiments (b) and (c). The area under the emission profile is called as P in subsequent equations.

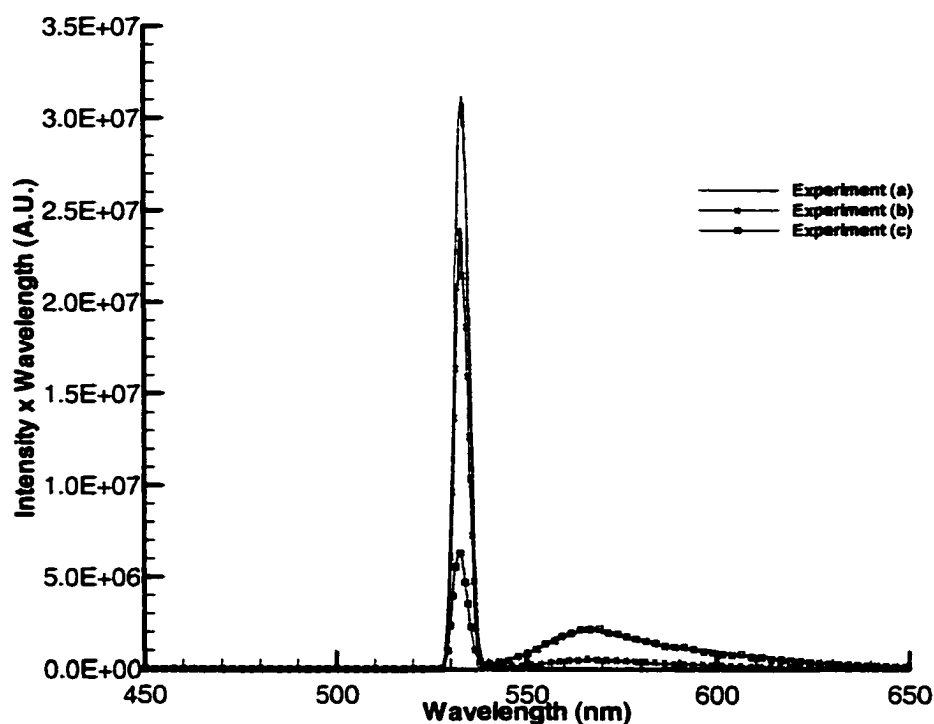


Figure 2.32 The spectra of  $10^{-4}$  [M] Rhodamine 6G solution. Experiment (a): the cuvette is empty; experiment (b): the cuvette is filled with the solution and the laser beam is focused onto the sphere wall; experiment (c): the cuvette is filled with the solution and the laser beam is focused on the cuvette.

The following quantum efficiency equation was derived by Mello et al. (1997),

$$\eta = \frac{P_c - (1 - A)P_b}{L_a A} \quad (2.17)$$

where  $P_c$  is the amount of emitted light in the experiment (c),  $P_b$  is the amount of the emitted light in the experiment (b),  $L_a$  is the amount of unabsorbed light in the

experiment (a). The fraction,  $A$ , of the absorbed light, the absorbance of the sample, was defined by the following equation,

$$A = \left( 1 - \frac{L_c}{L_b} \right) \quad (2.18)$$

where  $L_c$  is the amount of unabsorbed light in the experiment (c) and  $L_b$  is the amount of unabsorbed light in the experiment (b).

Mello et al. (1997) reported the PL quantum efficiency value for a  $10^{-6}$  [M] Rhodamine 6G-ethanol solution as  $65 \pm 5\%$ . Fischer and Georges (1996) measured quantum yield of Rhodamine 6G in ethanol by using a thermal lens spectrometry method for different concentrations. They reported the quantum yield of Rhodamine 6G-ethanol solution as 94% for low concentrations (up to  $2 \times 10^{-4}$  [M]). Georges et al. (1996) reported quantum yield values ranging from 93 to 95% for Rhodamine 6G-ethanol solution. A preliminary PL quantum efficiency value was obtained for a  $10^{-4}$  [M] Rhodamine 6G in ethanol solution in the set-up just described. The value,  $91.5 \pm 3.6\%$ , is not consistent with the result reported by Mello et al. (1997). The percent error is based upon the uncertainties associated with the numerical determination of the areas under the curves in Figure 2.32-not accumulated experimental error. My value is closer to those reported by Fischer and Georges (1996) and Georges et al. (1996); the discrepancy has not been resolved.

A molecule in an excited electronic state can decay to lower energy levels through radiative relaxation (emission) or non-radiative processes. An excited molecule follows

the pathway, which minimizes the lifetime of the excited state. Non-radiative processes are always in competition with fluorescence and they reduce the amount of fluorescence. These processes are vibrational relaxation, internal conversion, intersystem crossing, and external conversion. The vibrational relaxation time is significantly shorter than the average lifetime of an electronically excited state. Therefore, solution samples almost immediately lose the excess vibrational energy by the vibrational relaxation process. Collisions between the vibrationally excited molecules and the solvent cause the loss of excitation energy as heat instead of as emitted light. As a result, fluorescence from solution occurs from the lowest vibrational level of the excited state, even though molecules in a solution are elevated to any vibrational level during an electronic excitation process. The internal conversion process is the non-radiative transition between states of the same multiplicity. The loss of energy by internal conversion process is more probable than fluorescence if the vibrational levels of the two states overlap. The intersystem crossing term is employed when a change in multiplicity of the molecule occurs. The external conversion processes are the deactivation of an excited electronic state due to the interaction and energy transfer between the excited molecule and the solvent. Further information on non-radiative processes can be found in references by Skoog and West (1971), Straughan and Walker (1976), and Eckbreth (1988).

The quantum efficiency for fluorescent process is written as:

$$\eta_F = \frac{\text{Number of emitted fluorescent photons}}{\text{Number of absorbed excitation photons}} \quad (2.19)$$

The quantum efficiency can also be defined in terms of rate constants:

$$\eta = k_{rad} \tau = \frac{k_{rad}}{k_{rad} + k_{nonrad}} \quad (2.20)$$

where  $\tau$  is the radiative lifetime of the excited level and  $k_{nonrad}$  is the rate constant associated with the nonradiative decay. The quantum efficiency for fluorescent process is written in terms of rate constants as follows:

$$\eta_F = k_F \tau_F = \frac{k_F}{k_F + k_{IC} + k_{EC} + k_{ISC}} \quad (2.21)$$

where subscript F refers to the fluorescence process; subscripts IC, EC, and ISC refer to internal conversion, external conversion, and intersystem crossing, respectively.  $\tau_F$  is the fluorescence lifetime (or fluorescence decay time).

Since a large number of rate constants are involved in the evaluation of the quantum efficiency, calibrating a PLIF experiment is a challenging task.

## 2.5. Summary of Spectral Results

The principle results in Sections 2.3 and 2.4 include following points:

- (1) The uncertainty magnitude of the absorption spectra experiments is within 4.8%.
- (2) The present spectral results agree with Berlman's absorption spectra results within 13%. Berlman (1965) reported his experimental error as 10%.

- (3) The centroid wavelength values, which were obtained from the present emission spectral results, agree with the centroid wavelength values in Berlman's study.
- (4) An additional data point for quantum efficiency of Rhodamine 6G-ethanol solution was determined as  $91.5 \pm 3.6\%$ . This value agrees with the value reported by Fischer and Georges (1996) and Georges et al. (1996), but does not agree with the value reported by Mello et al. (1997).

# **CHAPTER 3**

## **SPRAY MODELING – DISCRETE AND CONTINUOUS PHASES**

### **THEORY AND NUMERICS**

The dispersed two-phase flow treated in this study involves discrete elements (liquid droplets) surrounded by a continuous phase (gas phase). The flow field for the continuous phase was described by using the Eulerian equations of motion. The Lagrangian approach was used to track individual droplet packets along trajectories through the flow field. The interaction between the two phases was taken into account by means of source terms. The theoretical formulations and numerical method are briefly outlined in this chapter.

These modeling results are presented for the main purpose of demonstrating the capabilities of one particular dispersed two-phase flow code. Also, two cases are solved, and the results are interpreted, similar to the spray experiments reported in Chapter 2, which have provided the boundary conditions for the model.

#### **3.1. Dispersed Two-Phase Flow Modeling**

The nature of the dispersed two-phase flow is quite complicated since there is a close interaction between the two phases. The motion of the discrete phase is influenced by the motion of the continuous phase. Similarly, the continuous phase is influenced by the motion of the droplets in the flow field. The CFD (computational fluid dynamics) code Fluent, Fluent Inc. (1998), which was employed to solve the two-phase flow

problem in this study, solves the dispersed two-phase flow problems by assuming that the discrete phase is sufficiently dilute. In this case, droplet-droplet interactions and droplet volume fractions in the continuous phase can be neglected. The code uses the Lagrangian approach to simulate the discrete phase motion. The use of the Lagrangian approach provides the interpretation of the balance of forces acting on the droplets that move along individual trajectories. The general form of the conservation equations for the dilute spray can be found in the study of Gosman and Ioannides (1983).

The solution procedure involves two-step approach. First, continuous phase flow is calculated separately. Second, the dispersed phase trajectory calculations are made. Then, continuous phase source terms are updated according to the trajectory calculations. Two-step calculations are continued until the converged solution is obtained.

If the discrete phase is not dilute (i.e., the discrete phase volume fraction is not negligible in the continuous phase), the trajectory calculations become computationally very large. It is very expensive to calculate every droplet trajectory for a large number of droplets or droplet packets. Numerical stability problems may arise due to the increased coupling between the discrete and continuous phases if the two-step solution method is introduced to systems with high to moderate discrete phase volume fractions.

The standard  $\kappa$ - $\epsilon$  model was employed for the continuous phase turbulence representation. The stochastic approach may be used to determine the effect of turbulence on the trajectory of droplets; see discussion in Section 3.1.2.



### 3.1.1. Continuous Phase Governing Equations

The Eulerian equations solved for the continuous phase mean motion can be written as follows (Hinze (1959)):

Conservation of mass

$$\frac{\partial}{\partial x_i}(\rho u_i) = S_m \quad (3.1)$$

Conservation of momentum

$$\frac{\partial}{\partial x_i}(\rho u_i u_i) = -\frac{\partial P}{\partial x_i} + \frac{\partial}{\partial x_i}((\tau_{ij})_{eff} - \overline{\rho u'_i u'_j}) + F_i \quad (3.2)$$

Conservation of energy

$$\frac{\partial}{\partial x_i}(u_i (\rho E + p)) = \frac{\partial}{\partial x_i} \left( k_{eff} \frac{\partial T}{\partial x_i} + u_i (\tau_{ij})_{eff} \right) + S_h \quad (3.3)$$

where  $S_m$  is the mass added to the continuous phase from the dispersed phase;  $F_i$  is the momentum source due to the droplet motion through the continuous phase domain (e.g., drag force);  $S_h$  is the heat source caused by the droplet interaction (e.g., vapor diffusion). Source terms in conservation of mass, momentum, and energy equations for the continuous phase represent the interaction with the discrete phase. In other words, the source terms in the continuous phase governing equations appear due to the effects of discrete phase motion in the flow field, and they provide the coupling between the two phases.

The term  $(-\rho \overline{u'_i u'_j})$  in the conservation of momentum equation corresponds to the effects of turbulence. The stress tensor,  $(\tau_{ij})_{eff}$ , is defined as

$$(\tau_{ij})_{eff} = \mu_{eff} \left[ \left( \frac{\partial u_j}{\partial x_i} + \frac{\partial u_i}{\partial x_j} \right) - \frac{2}{3} \delta_{ij} \frac{\partial u_k}{\partial x_k} \right].$$

The effective dynamic viscosity,  $\mu_{eff}$ , is the sum

of sum of molecular and turbulent viscosities. The term E denotes the total energy,

$$E = h - \frac{p}{\rho} + \frac{u_i^2}{2},$$

in Equation (3.3). The effective conductivity term in conservation of

energy equation,  $k_{eff}$ , is defined as  $k_{eff} = k + k_t$ , where  $k_t$  is the turbulent thermal

conductivity. The  $\frac{\partial}{\partial x_j} (\mu_i (\tau_{ij})_{eff})$  term in the conservation of energy equation represents

viscous dissipation.

Turbulent kinetic energy,  $\kappa$ , and turbulent dissipation rate,  $\varepsilon$ , are obtained from the closure equations (Launder and Spalding (1974)):

$$\frac{\partial}{\partial x_i} (\rho u_i \kappa) = \frac{\partial}{\partial x_i} \left[ \left( \mu + \frac{\mu_t}{\sigma_\kappa} \right) \frac{\partial \kappa}{\partial x_i} \right] + G_\kappa - \rho \varepsilon \quad (3.4)$$

and

$$\frac{\partial}{\partial x_i} (\rho u_i \varepsilon) = \frac{\partial}{\partial x_i} \left[ \left( \mu + \frac{\mu_t}{\sigma_\varepsilon} \right) \frac{\partial \varepsilon}{\partial x_i} \right] + C_{1\varepsilon} \frac{\varepsilon}{\kappa} G_\kappa - C_{2\varepsilon} \rho \frac{\varepsilon^2}{\kappa} \quad (3.5)$$

where  $G_\kappa$  refers to the generation of turbulent kinetic energy due to mean velocity gradients and is defined as,

$$G_k = -\rho \overline{u'_i u'_j} \frac{\partial u_j}{\partial x_i} \quad (3.6)$$

In Equation (3.5),  $C_{1\varepsilon}, C_{2\varepsilon}$  are constants and  $\sigma_k, \sigma_\varepsilon$  are the Prandtl numbers for  $\kappa$  and  $\varepsilon$ , respectively. The turbulent viscosity,  $\mu_t$ , is calculated from:

$$\mu_t = \rho C_\mu \frac{\kappa^2}{\varepsilon} \quad (3.7)$$

where  $C_\mu$  is a constant. The following values were used for model constants:

$$C_{1\varepsilon} = 1.44, C_{2\varepsilon} = 1.92, C_\mu = 0.09, \sigma_k = 1.0, \sigma_\varepsilon = 1.3$$

### 3.1.2. Discrete Phase Governing Equations

Since the droplet-droplet interaction and gravitational force are neglected, the drag force governs the motion of droplets. The equation of droplet motion in a Lagrangian reference frame can be written as follows for per unit droplet mass (Elghobashi and Truesdell (1992)):

$$\frac{du_{id}}{dt} = F_D(u_i - u_{id}) \quad (3.8)$$

where  $u_c$  is the continuous phase velocity component and  $u_d$  is the droplet velocity component. The inverse of velocity response time,  $F_D$ , is defined as (Elghobashi and Truesdell (1992)):

$$F_D = \frac{18\mu_c}{\rho_d D_d^2} \frac{C_D Re}{24} \quad (3.9)$$

where subscript c represents continuous phase and subscript d represents droplet.  $D_d$  refers to the droplet diameter. The relative Reynolds number,  $Re$ , is calculated from:

$$Re = \frac{\rho_c D_d}{\mu_c} |u_d - u| \quad (3.10)$$

where  $u_d$  is the droplet velocity and  $u$  is the continuous phase velocity. The drag coefficient,  $C_D$ , is calculated as follows (Morsi and Alexander (1972)):

$$C_D = a_1 + \frac{a_2}{Re} + \frac{a_3}{Re^2} \quad (3.11)$$

Values of constants,  $a_i$ , are given by Morsi and Alexander (1972). The droplet velocity is obtained by integrating Equation (3.8) in time. The instantaneous droplet location along the trajectory is predicted by

$$\frac{dx_i}{dt} = u_{id} \quad (3.12)$$

Trajectories are obtained by solving Equations (3.8) and (3.12) in each coordinate direction. When a sufficient number of droplets (or droplet packets) are tracked individually through the flow domain by solving above equations, the average nature of the flow is determined.

The heat transfer from the continuous phase to the discrete phase is calculated according to the three cases in Fluent, Fluent Inc. (1998). The first case is applied when the droplet temperature is less than the vaporization temperature of the liquid,  $T_{vap}$ . If the droplet temperature exceeds the vaporization temperature of the liquid, the second case is initiated and the evaporation begins. The second case is applied until the boiling point temperature,  $T_{bp}$ , is reached. The third case is initiated if the droplet temperature reaches the boiling point temperature. A uniform temperature within the droplet and negligible radiation heat transfer are assumed for the heat transfer calculations. The vaporization temperature, which does not represent any physical characteristic, is set to activate the second heat transfer case.

Since the vaporization temperature was chosen lower than the spray injection temperature for the current spray modeling, the first heat transfer case was not initiated. The third case did not play any role in the heat transfer calculations either, because the droplet temperature did not reach to the boiling point temperature in the current model. The boiling rate equations can be found in the reference of Kuo (1986).

In the second heat transfer case, the vapor concentration gradient between the droplet surface and the bulk gas governs the rate of vaporization. The molar flux of the droplet vapor,  $N$ , is calculated as (Bird et al. (1960)):

$$N = k_c (C_s - C_\infty) \quad (3.13)$$

where  $k_c$  is the mass transfer coefficient,  $C_s$  is the vapor concentration at the droplet surface, and  $C_\infty$  is the vapor concentration in the bulk gas. The mass transfer coefficient is calculated by the following correlation, which is derived by Ranz and Marshall (1952):

$$Nu_{AB} = \frac{k_c D_d}{D_v} = 2.0 + 0.6 Re^{1/2} Sc^{1/3} \quad (3.14)$$

where  $D_v$  is the diffusion coefficient of the vapor in the continuous gas phase and  $Sc$  is the Schmidt number. The change in the droplet mass with the time is calculated with the help of the molar flux of the droplet vapor:

$$\Delta m_d = N A_d M \Delta t \quad (3.15)$$

where  $A_d$  is the surface area of the droplet and  $M$  is the molecular weight. The rate of change in the droplet temperature for the second case is due to the convective and latent heat transfer. The heat transfer between the droplet and the continuous phase is computed from (Fluent Inc. (1998)):

$$m_d c_p \frac{dT_d}{dt} = h A_d (T_\infty - T_d) + \frac{dm_d}{dt} h_{fg} \quad T_{\text{vap}} < T_d < T_{\text{bp}} \quad (3.16)$$

where  $h$  is the convective heat transfer coefficient,  $\frac{dm_d}{dt}$  is the rate of evaporation, and  $h_{fg}$  is the latent heat.

A coupled two-step solution method may be implemented to take into account the mass, momentum, and heat exchange between the discrete phase and the continuous phase. The numerical solution begins with the continuous phase iterations. One discrete phase iteration is performed after every specified number of continuous phase iterations. For example, one discrete phase iteration was performed per twenty continuous phase iterations for the current study. While a droplet passes through each control volume, the changes in the mass, momentum, and thermal energy of the droplet are examined. The evaluation of exchange terms between phases is outlined in the subsequent paragraphs. Figure 3.1 depicts the exchange of mass, momentum, and heat between the discrete and continuous phases.

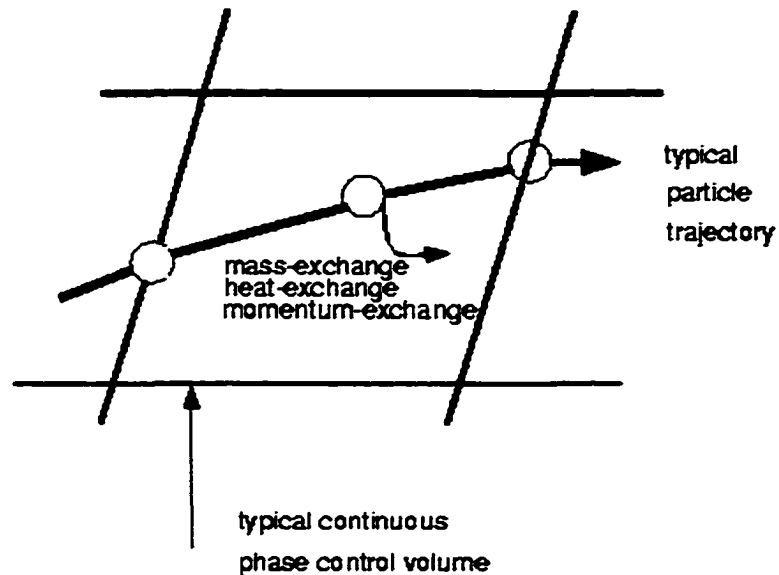


Figure 3.1 Mass, momentum and heat exchange between the discrete and continuous phases, Fluent Inc. (1998); reprinted from the Fluent manual with the permission of Fluent, Inc.

The continuous phase source terms are updated according to the interphase exchange quantities determined during the discrete phase iterations, and the continuous phase flow is recalculated. The discrete phase iteration is performed in the modified continuous phase flow field. The coupled calculations are carried on until the convergence criteria for the continuous phase is satisfied. When the continuous phase flow field residuals are reduced sufficiently, the discrete phase trajectories are established.

The mass transfer from the discrete phase to the continuous phase occurs due to the change in mass of a droplet while passing through each control volume. The mass change that appears as a source term in the continuous phase continuity equation is calculated as:

$$\Delta\omega = \frac{\Delta m_d}{m_{d0}} \dot{m}_{d0} \quad (3.17)$$



where  $\Delta m_d$  is the change in the mass of the droplet in the control volume (see Equation (3.15)),  $m_{d0}$  is the initial mass of the droplet, and  $\dot{m}_{d0}$  is the initial mass flow rate of the droplet injection being tracked.

The momentum transfer from the continuous phase to the discrete phase is due principally to the drag force. Other forces, such as brownian force or thermophoretic force, are neglected. The momentum exchange that appears as a sink term in the continuous phase momentum equation is calculated by using the following equation:

$$\Delta F = \sum \left( \frac{18\mu_c C_D \text{Re}}{\rho_d D_d^2 24} (u_d - u) \right) \dot{m}_d \Delta t \quad (3.18)$$

where  $\Delta t$  is the time step.

The heat exchange that appears as a source or sink term in the continuous phase energy equation is calculated from (Fluent Inc. (1998)):

$$\Delta Q = \left[ \frac{\overline{m}_d}{m_{d0}} c_p \Delta T_d - \frac{\Delta m_d}{m_{d0}} h_{fg} \right] \dot{m}_{d0} \quad (3.19)$$

where  $\overline{m}_d$  is the average mass of the droplet in the control volume,  $h_{fg}$  is the latent heat of the volatile, discrete phase material.

If the flow is turbulent, the random effects of turbulence on individual droplets (or droplet packets) may be simulated by employing a stochastic technique. In the development of the stochastic technique, Litchford and Jeng (1991) assumed that each

particle interacts with a series of turbulent eddies, and the fluctuating velocity is constant for a lifetime of eddy. When the stochastic technique is employed, the instantaneous continuous phase velocity is used in Equation (3.8). The mean and fluctuating components of continuous phase velocity form the instantaneous continuous phase velocity,  $u_i$ , as follows:

$$u_i = \overline{u_i} + u'_i \quad (3.20)$$

Fluctuating velocities are characterized by a Gaussian probability distribution. The values of fluctuating velocities are related with the local root-mean-square (rms) value of the velocity fluctuations for the  $\kappa$ - $\varepsilon$  model; see Fluent Inc. (1998).

$$u'_i = \phi \overline{(u_i'^2)}^{1/2} = \phi(2\kappa/3)^{1/2} \quad (3.21)$$

where  $\phi$ , is a Gaussian distributed random variable. Eddy lifetime is defined by,

$$T_L = 2C_L \frac{\kappa}{\varepsilon} \quad (3.22)$$

where the constant,  $C_L$ , equals to the value of 0.15 for  $\kappa$ - $\varepsilon$  model, and  $\kappa$  is a measure of turbulent kinetic energy and  $\varepsilon$  is the energy dissipation rate.

## 3.2. Modeling of Spray in Ambient Air

### 3.2.1. Discretization

The solution technique used in Fluent is based upon a finite volume method. In this method, the flow field is divided into small sub-volumes, called control volumes. The discretization of governing equations is performed by a reduction to finite difference equations valid for each control volume. Algebraic equations are obtained by writing variables on the cell faces in terms of neighboring cell center values.

A differencing scheme is employed to interpolate convective terms on the cell faces from the cell center values. The first order upwind scheme was chosen in this work. The first order upwind scheme determines the face values by setting equal to the cell center value in the upstream cell; see Patankar (1980). Although higher order schemes are more accurate, the first order scheme is numerically more stable.

Under-relaxation is needed to control the change of variables because the non-linear coupling between transport equations may cause instability during the solution. The value at the next iteration is calculated from the old values, as follows:

$$\phi = \phi_{old} + \alpha \Delta \phi \quad (3.23)$$

where  $\alpha$  is the under-relaxation factor and  $\Delta \phi$  is the change in the variable.

The Semi-Implicit Method for Pressure-Linked Equations (SIMPLE) proposed by Patankar (1980) was chosen among three pressure-velocity coupling algorithms in the code. First, momentum equations are solved according to a given pressure field. If the calculated velocity field does not satisfy the continuity equation, a pressure correction is

calculated from mass imbalance. Pressure and velocity values are corrected by using the pressure correction. Calculations are continued until the corrected velocity field satisfies the continuity equation.

### **3.2.2. Inputs and Boundary Conditions**

Inputs of current spray modeling were obtained from the conditions of spray experiments reported in Chapter 2. Before spray was introduced to the system, the solution domain was assumed to be filled with air at 101,325 Pa pressure and 300 K temperature. The static flow rate of Dekka IV injector, 2.50 g/s, was chosen as the injection flow rate of the spray model. The spray material was specified as n-Heptane. The temperature of the injected spray in the model was 273 K.

The spray modeling was conducted in cylindrical polar coordinates. A half of the domain was solved due to the symmetry of the flow. A hundred trajectories with the same flow rate was specified for the half domain. The trajectories were injected with the angle between  $0^\circ$  and  $10^\circ$  ( $0^\circ$  at the spray center,  $10^\circ$  at the periphery). The two-dimensional computational grid was composed of 80 x 200 elements in the axial and radial directions respectively. Figure 3.2 shows the computational grid and boundary conditions used in this study. The X-axis represents axial direction and the Y-axis represents radial direction in the figure. The spray was introduced to the domain from the bottom left corner of the geometry. The grid was concentrated in the injection region to capture the interaction between phases.

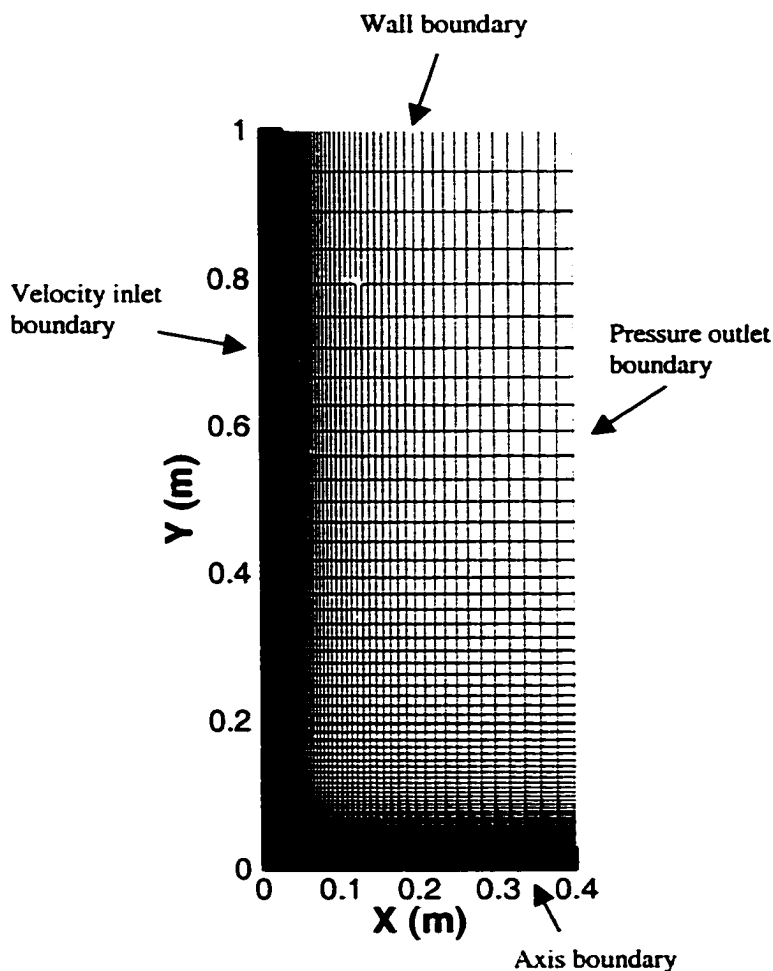


Figure 3.2 Computational grid.

Four boundary condition types were employed in this study: a velocity inlet, a pressure outlet, an axis, and a wall boundary condition. The velocity inlet boundary condition was used to direct the gas flow into the domain. The velocity of air was introduced as 0.1 m/s in the axial direction. The pressure outlet boundary condition was used where the flow direction was out of the domain. A static pressure value was specified as 101,325 Pa over the pressure outlet boundary. The turbulence intensity, which is defined as the ratio of root-mean-square of the velocity fluctuation to the mean flow velocity, was specified as 1% over both the velocity inlet and pressure outlet

boundaries. The centerline of the geometry was defined as the axis boundary type. The physical value for a variable at a point on the axis is set equal to the cell value in the adjacent cell. The wall boundary condition was chosen to close the external boundary of the physical domain. Attempts had been made to use pressure inlet boundary instead of wall boundary first. It was observed that the pressure inlet boundary accompanying velocity inlet, pressure outlet, and axis boundaries did not define the physical domain well and created convergence problems. The wall boundary is 1 m away from the axis boundary in the radial direction. Since the wall boundary is far from the spray region, the effect of wall on the spray flow should be negligible. A constant temperature condition, 300 K, was chosen over the wall boundary. Subsequent sections provide the presentation and interpretation of results for two cases.

### **3.2.3. Cases and Convergence**

By using the same input and boundary conditions described in Section 3.2.2, two cases were solved to investigate the effect of the droplet diameter. The number and angle of injected trajectories are also same for both cases. The first case involves only droplets with 100  $\mu\text{m}$  diameter. The second case employs a linear droplet diameter distribution between 40  $\mu\text{m}$  and 100  $\mu\text{m}$ . The convergence criterion was set to  $10^{-6}$  for all scaled residuals in both cases. Figure 3.3 shows residual graph for the constant droplet diameter case and Figure 3.4 shows residual graph for the linear droplet diameter distribution case. For the purpose of brevity the constant droplet diameter case will be called “case cdd” and the linear droplet diameter distribution case will be called “case lddd” throughout this chapter. The constant droplet diameter case converged after 78,172 iterations. The linear droplet diameter distribution case converged after 76,561 iterations. The oscillations

observed in graphs are due to the effect of discrete phase iterations. Note that one discrete phase iteration was performed per twenty continuous phase iterations.

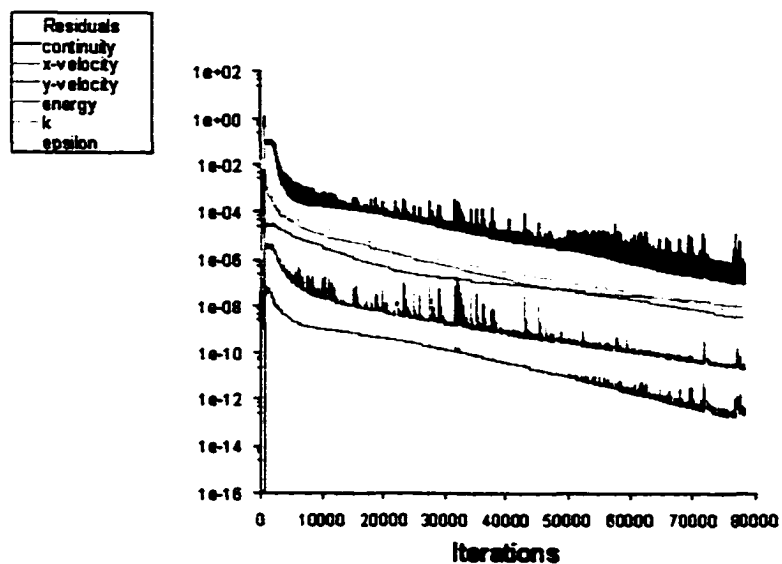


Figure 3.3 Convergence of the case cdd.

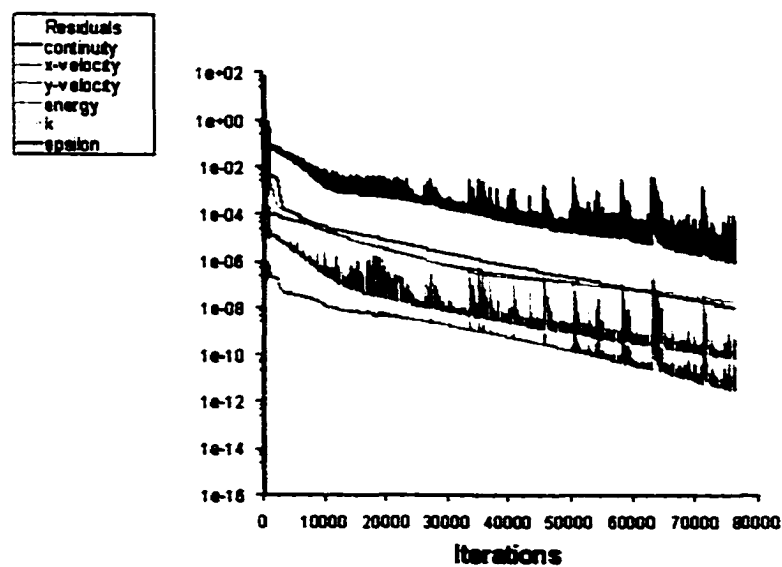


Figure 3.4 Convergence of the case lddd.

### 3.2.4. Discussion of Results

The results of numerical simulation are presented in this section. Droplet traces figures represent droplet trajectories tracked during the discrete phase solutions. Note that the discrete phase was described by using the Lagrangian approach.

Figures 3.5 and 3.6 show the droplet traces colored by the droplet velocity magnitude for the cdd case and for the lddd case, respectively. As it can be seen from particle traces figures, the injection velocity, 10 m/s, decreases rapidly along the spray edge. However, the injection velocity magnitude drops slowly along the spray axis and creates a core region close to the injection tip. Particle traces figures indicate that the core region diffuses more along the spray axis for the cdd case.

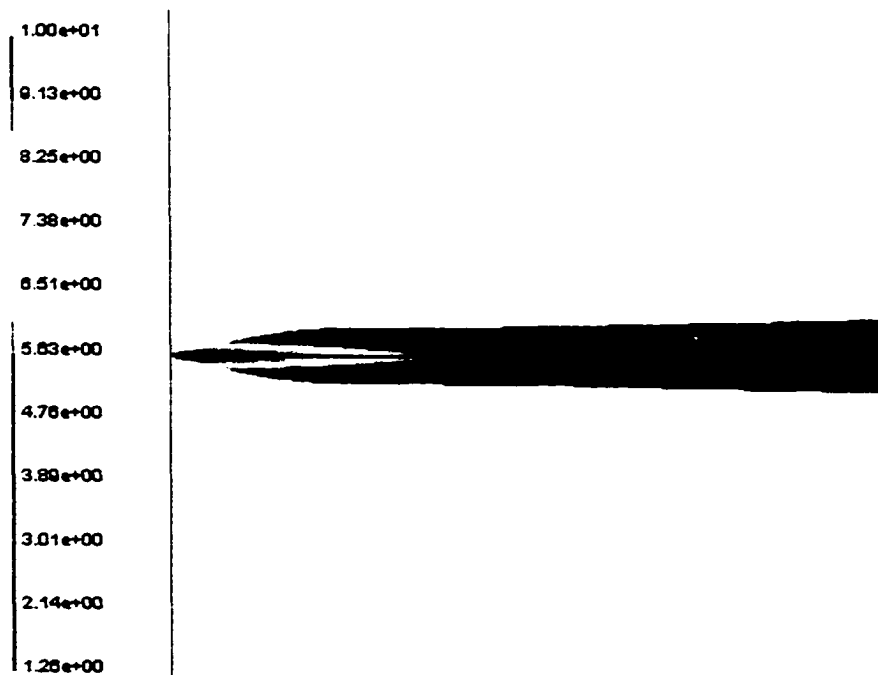


Figure 3.5 Droplet traces colored by the droplet velocity magnitude (m/s) for the cdd case.



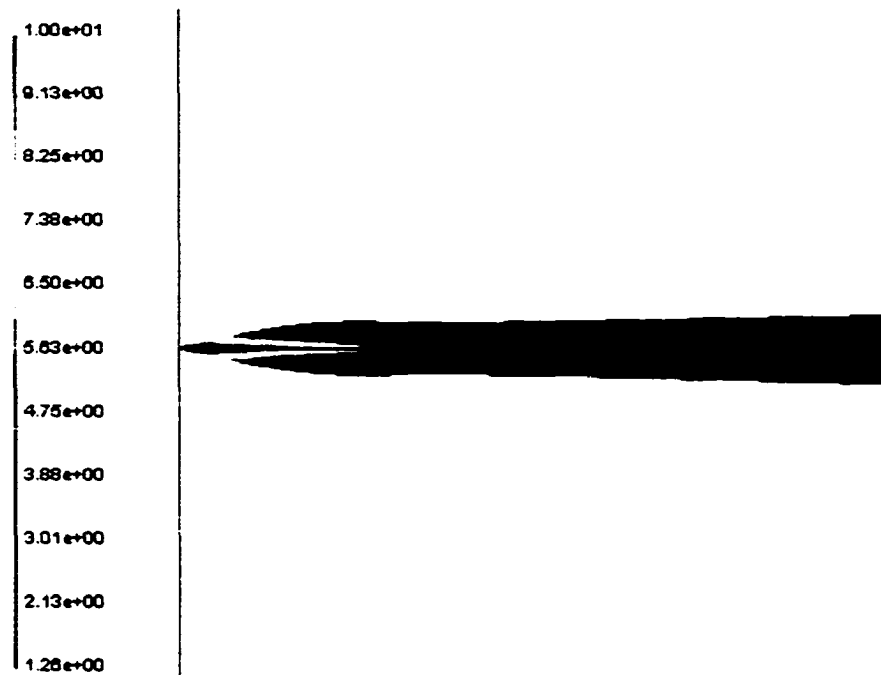


Figure 3.6 Droplet traces colored by the droplet velocity magnitude (m/s) for the lddd case.

Figures 3.7 and 3.8 show droplet traces colored by the droplet temperature for the cdd case and for the lddd case, respectively. Droplets are injected at 273 K and appear close to the injection temperature around injection tip since they move further without getting chance to heat up. The temperature of the droplets along the spray edge increases rapidly where the velocity of droplets is low. The main distinction between the cdd case and the lddd case lies at the spray center temperature. The spray center temperature rises to 280 K towards the outlet boundary for the cdd case. However, the spray center temperature increases only 2 K in the lddd case.

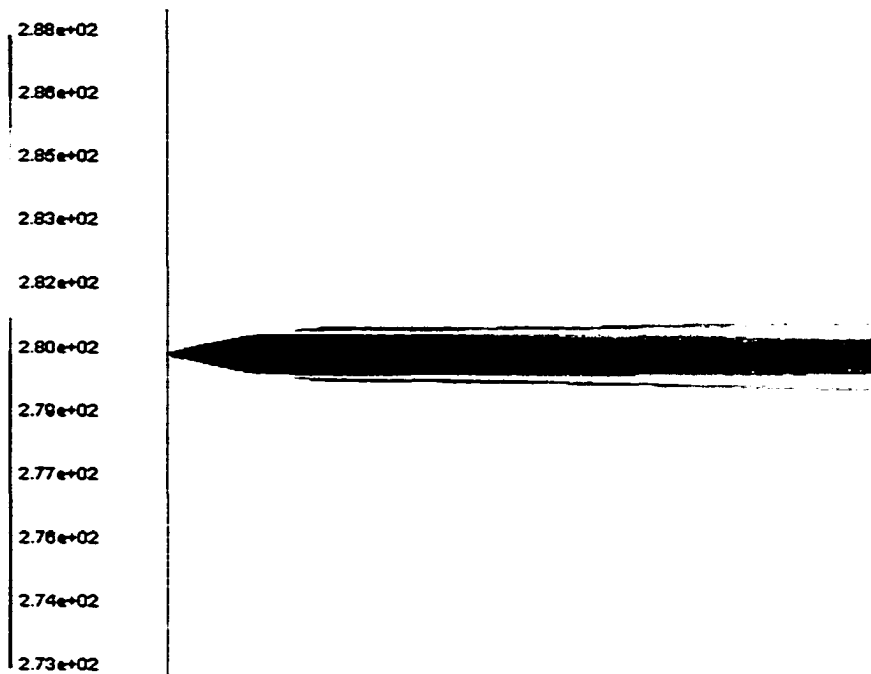


Figure 3.7 Droplet traces colored by the droplet temperature (K) for the cdd case.

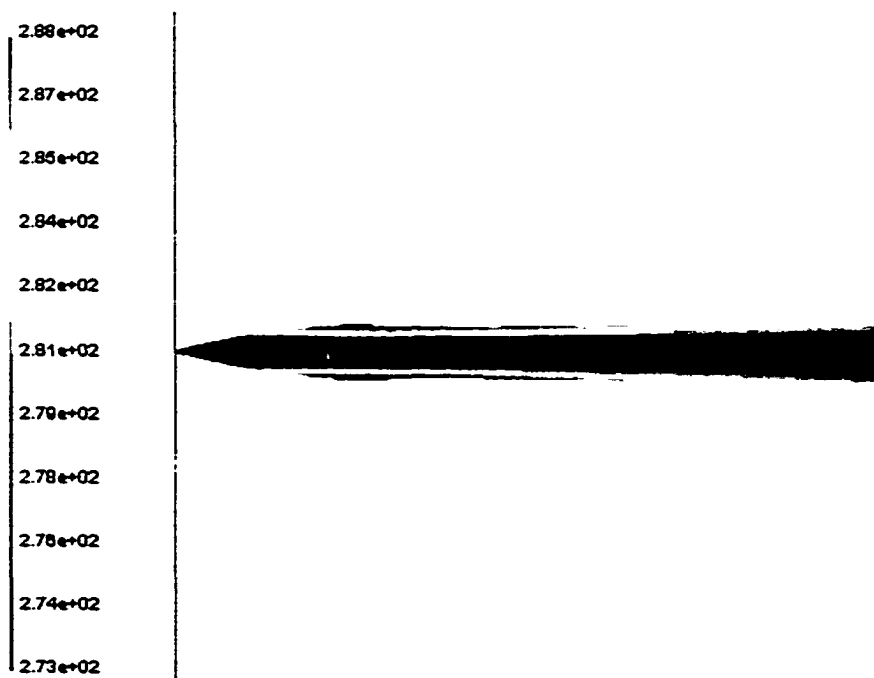


Figure 3.8 Droplet traces colored by the droplet temperature (K) for the lddd case.

Figures 3.9 and 3.10 show the velocity magnitude change in the radial position for the cdd case and lddd case, respectively. Each line in these graphs represents the velocity magnitude according to the radial position at a particular axial location. Results are shown for the four different axial locations:  $X=0.1$  m;  $X=0.2$  m;  $X=0.3$  m;  $X=0.4$  m. As it can be seen from figures, velocity magnitude values close to the spray center are higher at all axial locations for the cdd case. Spray radius is slightly larger for the cdd case. The change of the velocity magnitude in the radial direction is small at  $X=0.4$  m (at the outlet boundary) for both cases.

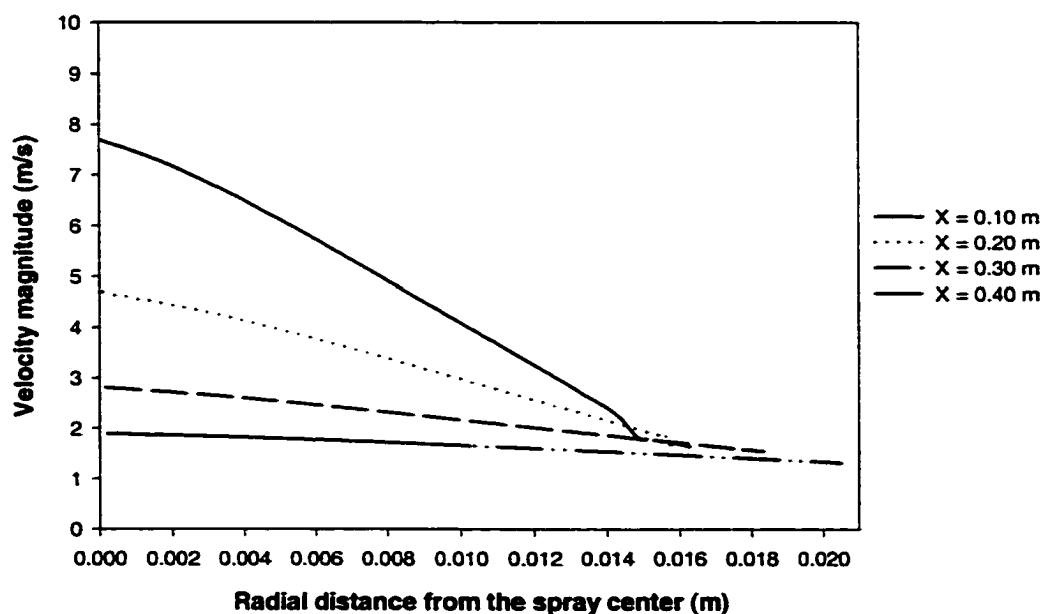


Figure 3.9 Velocity magnitude versus radial position for the cdd case.

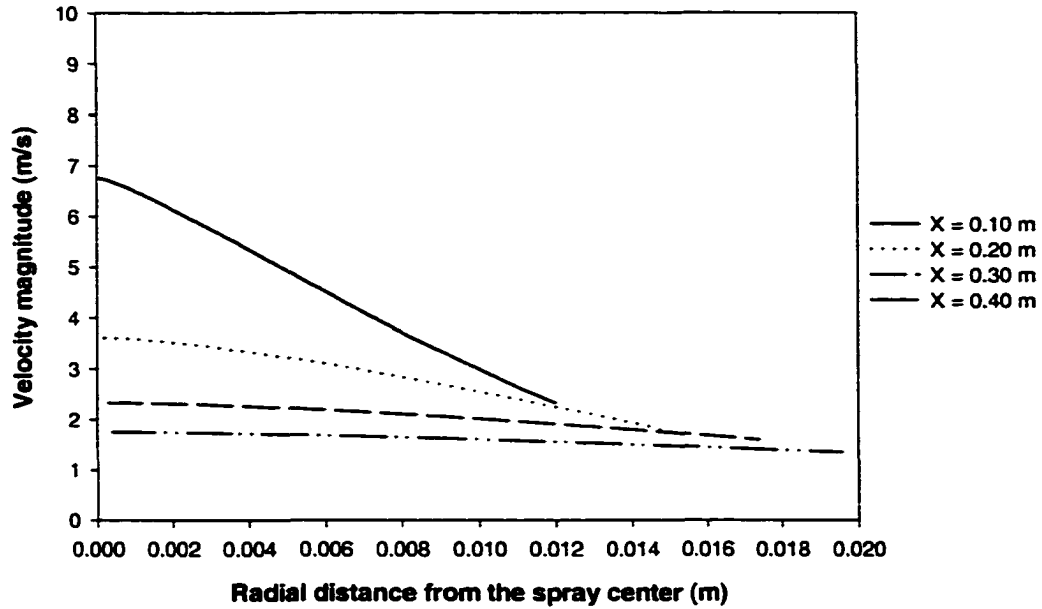


Figure 3.10 Velocity magnitude versus radial position for the lddd case.

Figures 3.11 and 3.12 show the velocity magnitude change according to the axial position for the cdd case and lddd case, respectively. Results are shown for the five different radial locations:  $Y=0.002$  m;  $Y=0.005$  m;  $Y=0.008$  m;  $Y=0.012$  m;  $Y=0.016$  m. The velocity magnitude decrease is steeper in the axial direction for the lddd case.

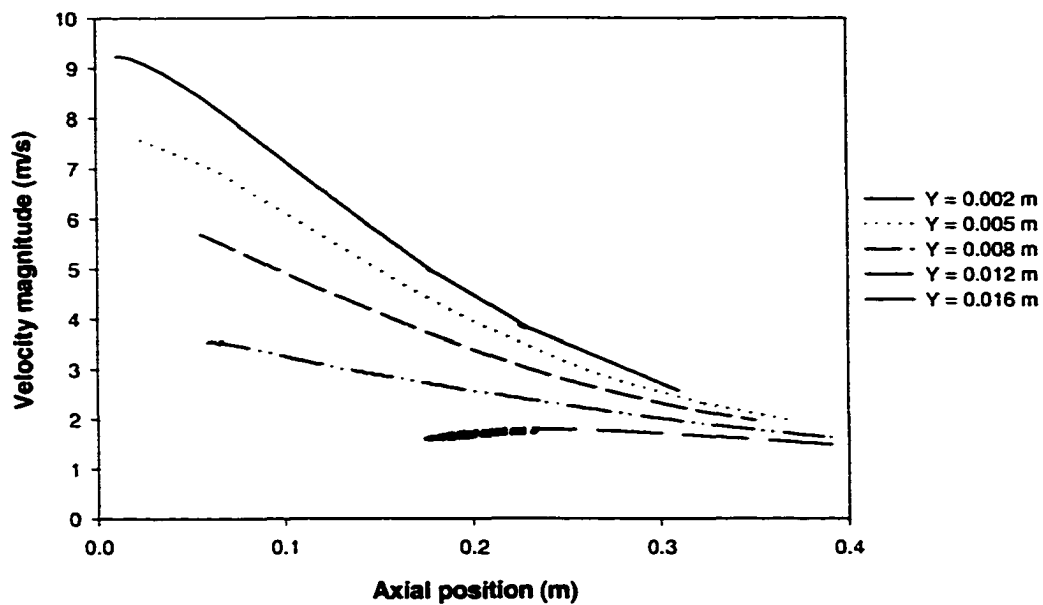


Figure 3.11 Velocity magnitude versus axial position for the cdd case.

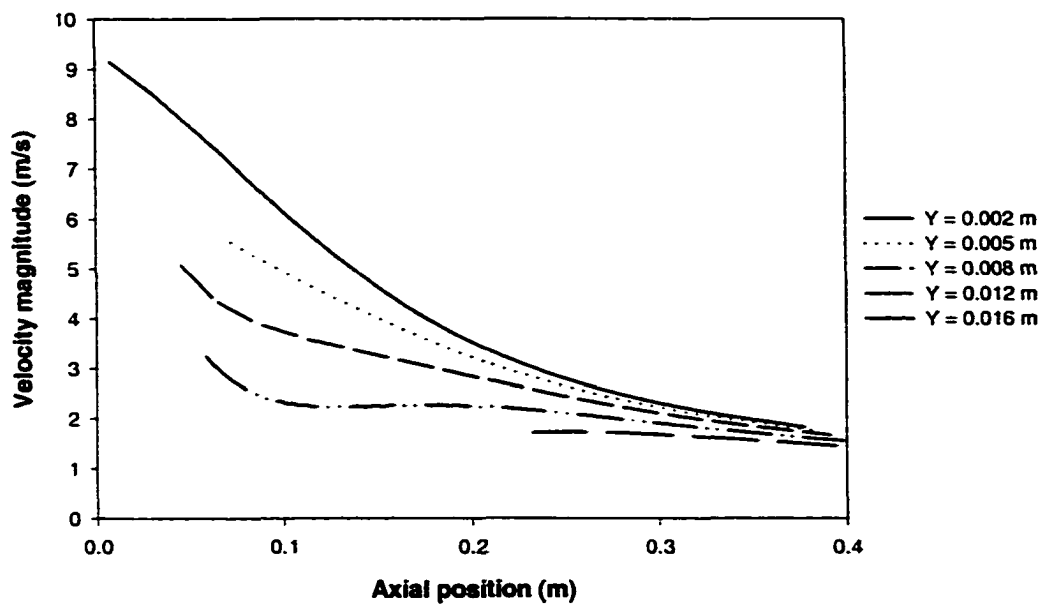


Figure 3.12 Velocity magnitude versus axial position for the lddd case.

Figures 3.13 and 3.14 show the temperature change in the radial direction for the four different axial locations. The temperature values steeply increase first, then reaches 282.5 K for all axial locations in the cdd case. The temperature values are lower at the spray center for the lddd case than cdd case. The temperature difference at  $X=0.4$  m is larger for the lddd case.

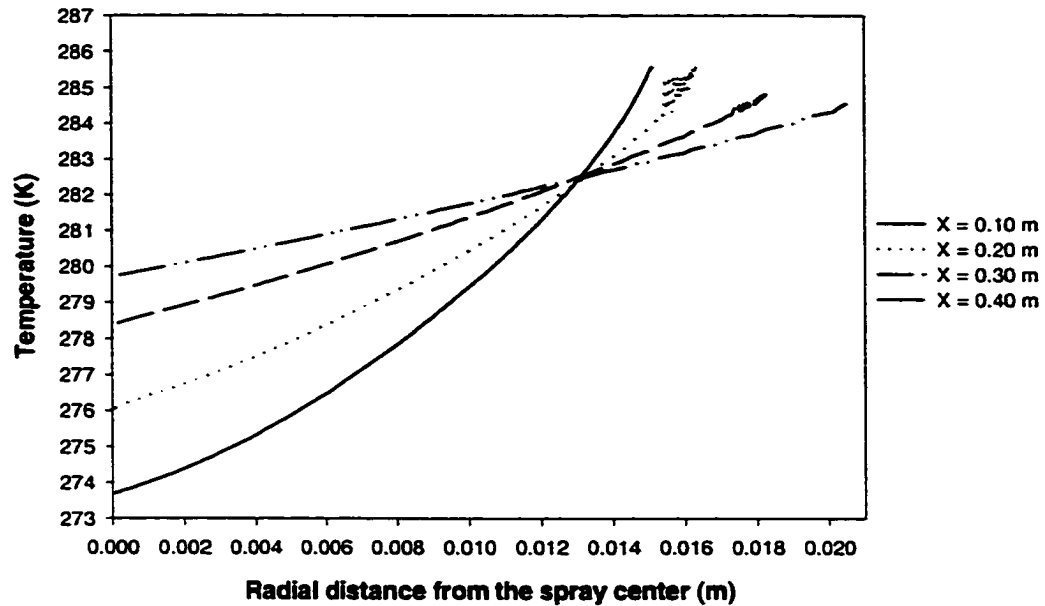


Figure 3.13 Temperature versus radial position for the cdd case.

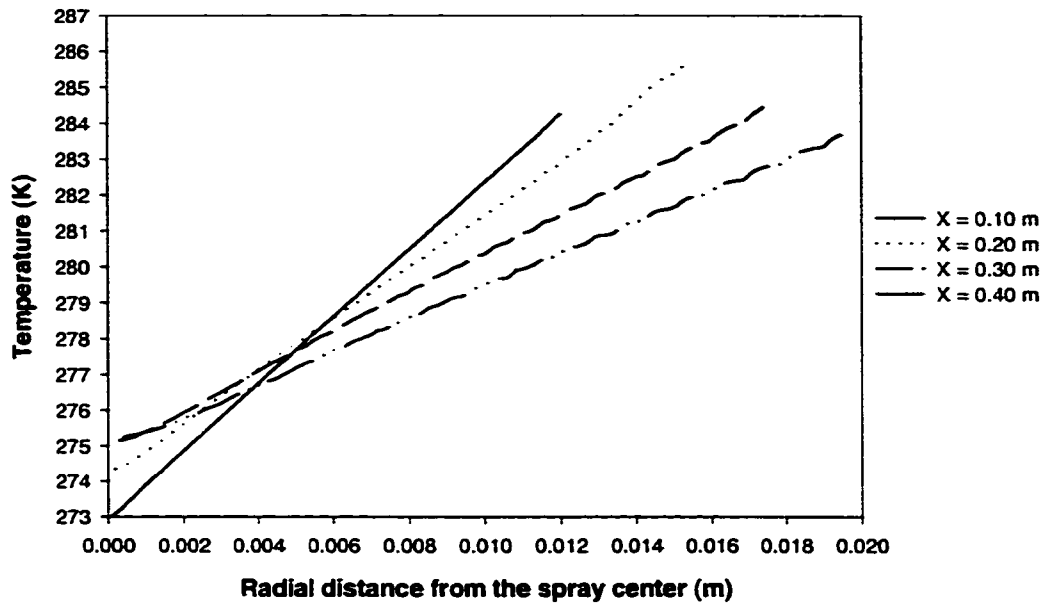


Figure 3.14 Temperature versus radial position for the lddd case.

Figures 3.15 and 3.16 show the temperature change in the axial direction for the five different radial locations. For the cdd case droplet temperature values increase in the axial direction except the  $Y=0.016$  m radial location. However, temperature values first increase then decrease for the lddd case. Since negligible evaporation is observed in the solution domain, this behavior does not seem logical.

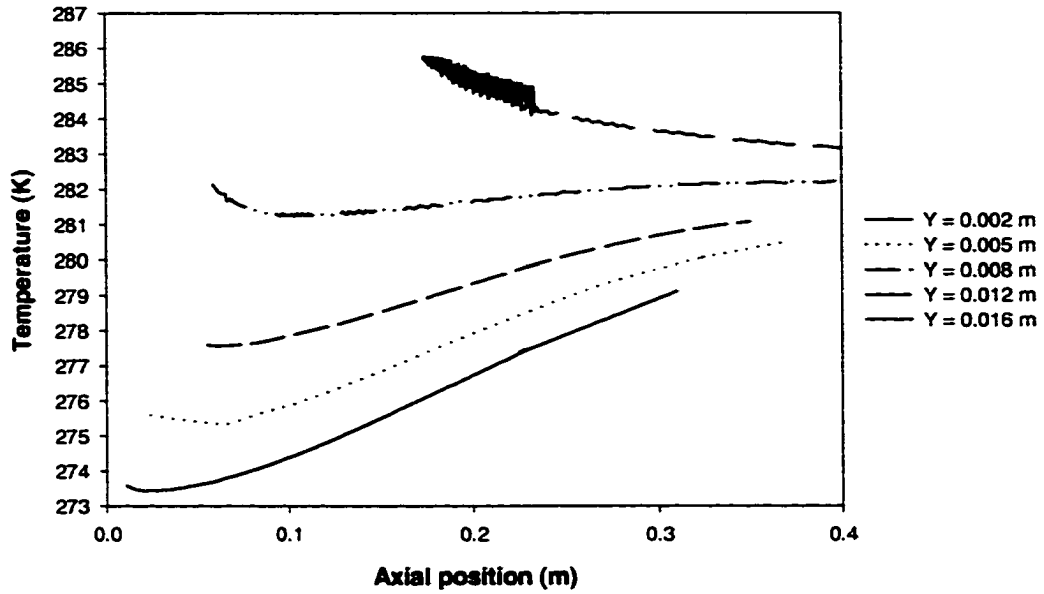


Figure 3.15 Temperature versus axial position for the cdd case.

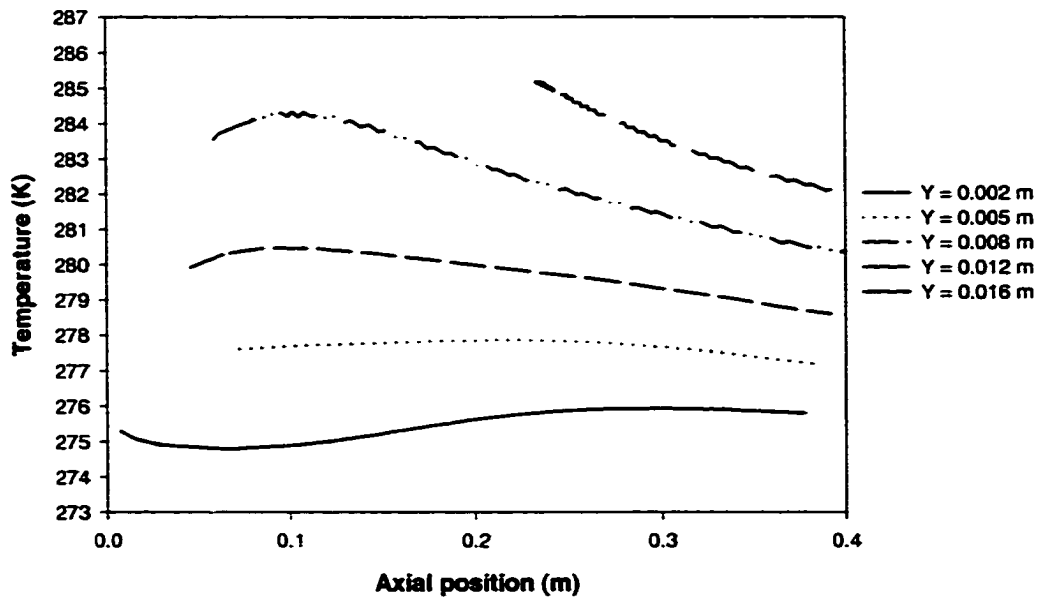


Figure 3.16 Temperature versus axial position for the lddd case.



Figure 3.17 shows the continuous phase velocity vectors for the cdd case. An enlarged figure is presented in order to show the details better. The continuous phase velocity vectors graph does not show the discrete phase. However, the graph depicts the effect of the discrete phase on the continuous phase velocity vectors. The entrainment of air is clearly observed along the shear layer.

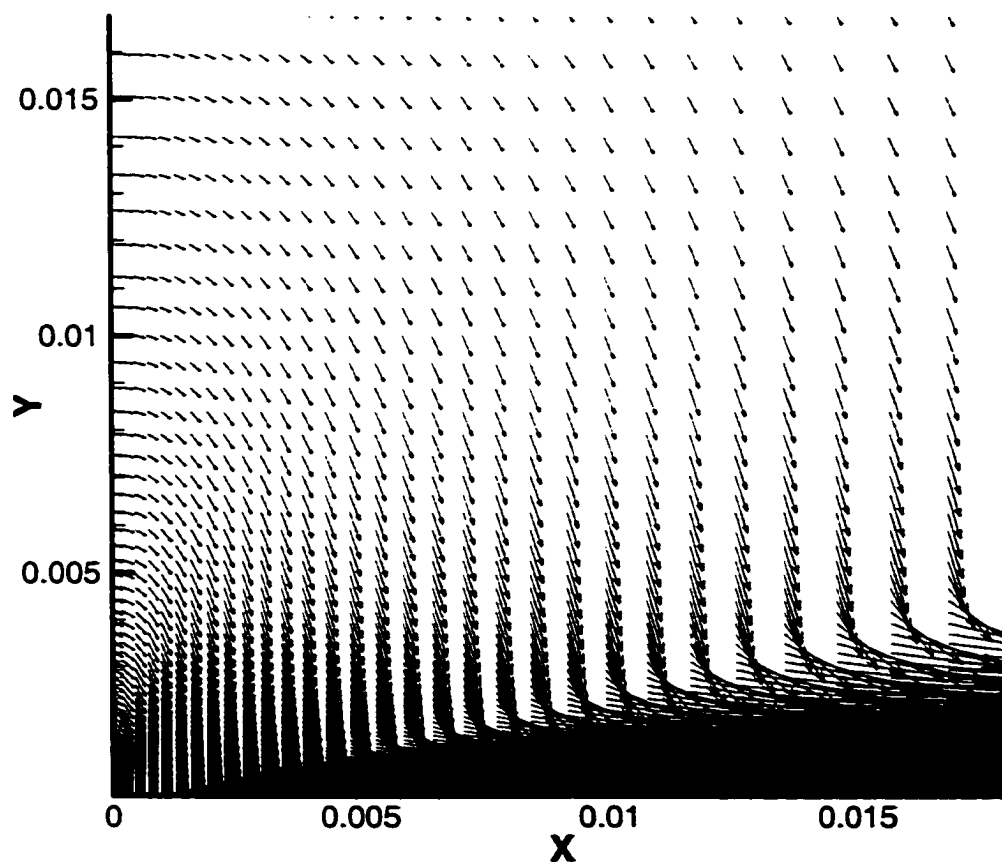


Figure 3.17 Continuous phase velocity vectors for the cdd case.

Figures 3.18 and 3.19 show droplet traces colored by the droplet residence time for the cdd case and lddd case. Maximum residence time is 0.229 s for both cases. Negligible evaporation was observed in the solution domain.

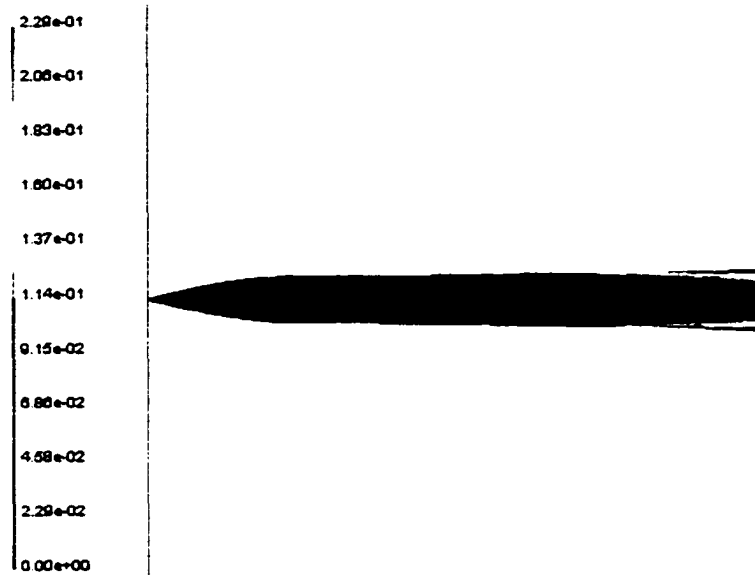


Figure 3.18 Droplet traces colored by the droplet residence time (s) for the cdd case.

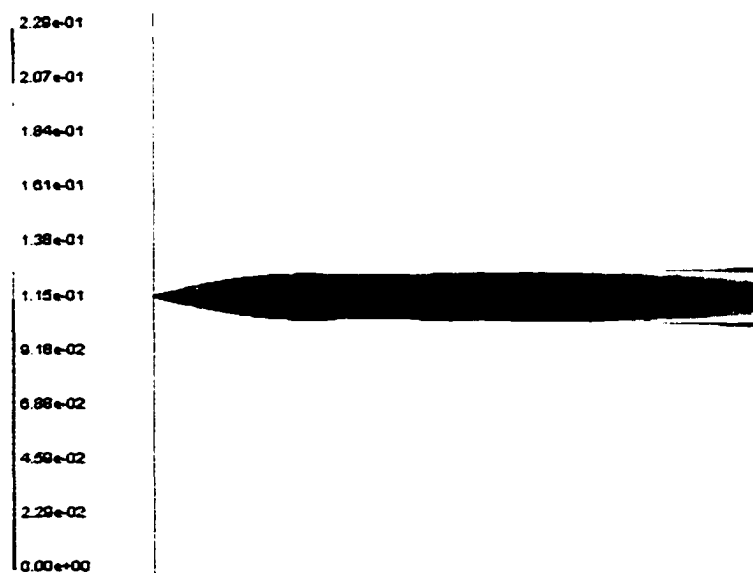


Figure 3.19 Droplet traces colored by the droplet residence time (s) for the lddd case.

One of the mass transfer mechanisms, evaporation, occurs in a spray domain if there is a transport of droplet vapor from the droplet surface to the free stream. The droplet vapor concentration difference is the driving force for the evaporation. The evaporation time of a droplet is described by Crowe et al. (1998) as follows:

$$\tau_m = \frac{D^2}{\lambda} \quad (3.24)$$

where  $D$  is the droplet diameter and  $\lambda$ , the evaporation constant, is given by,

$$\lambda = \frac{4Sh\rho_c D_v}{\rho_d} (\omega_{A,s} - \omega_{A,\infty}) \quad (3.25)$$

where  $Sh$  is the Sherwood number,  $\rho_c$  is the gas density in the free stream (continuous phase density),  $D_v$  is the diffusion coefficient,  $\rho_d$  is the droplet density,  $\omega_{A,s}$  is the vapor mass fraction at the droplet surface, and  $\omega_{A,\infty}$  is the vapor mass fraction in the free stream.

The vapor mass fraction at the droplet surface is calculated by

$$\omega_{A,s} = \frac{M_A}{M_M} \frac{P_A}{P} \quad (3.26)$$

where  $M_A$  is the molecular weight of the species A,  $M_M$  is the molecular weight of the mixture,  $P_A$  is the partial pressure of the vapor at the droplet surface, and  $P$  is the local pressure. The partial pressure of the vapor at the droplet surface is defined as the

saturation pressure corresponding to the droplet temperature. If the mole fraction of species A is small, then the molecular weight of the continuous phase is used rather than molecular weight of the mixture and the vapor mass fraction in the free stream is assumed zero in the calculations. The evaporation increase due to the relative velocity between the droplet and the conveying gas is represented by the Ranz-Marshall correlation (Ranz and Marshall (1952)),

$$Sh = 2 + 0.6Re^{0.5} Sc^{0.33} \quad (3.27)$$

where Re is the relative Reynolds number and Sc is the Schmidt number.

The evaporation time for the case cdd was obtained between 0.0962 s and 0.3275 s according to the relative Reynolds number. The evaporation time for the case lddd was obtained between 0.016 s and 0.284 s. Since the maximum residence time in the solution domain is 0.229 s, droplets do not have enough time for significant evaporation in the solution domain.

## **CHAPTER 4**

### **SUMMARY OF RESULTS AND CONCLUSIONS**

In this study, the experimental investigation and numerical analysis of the dispersed two-phase flow have been carried out. The experimental part of the study focuses on the Planar Laser Induced Fluorescence technique for the determination of spray mass distribution from a low-pressure port fuel injector. The numerical part of the study was conducted by employing a commercially available finite volume code. Some of the findings are summarized in the following sections.

#### **4.1. Concluding Remarks for Experimental Results**

The Planar Laser Induced Fluorescence technique was employed to investigate the spatial and temporal distribution of the spray mass from a set of four-hole, split-stream port fuel injectors. The experiments showed the application of the PLIF to detect the spray oscillation as functions of operating pressure and injector timing. Ensemble average PLIF fluorescent intensity images displayed the evolving structure of the spray mass distributions. The spray instabilities observed were most likely due to small, internal geometry differences within tolerances. By summing PLIF average images over the trigger delay time sequence, a measure of total mass passing through the laser light sheet was obtained. These results give information on the spatial spray mass distribution during an injection event. The Planar Laser Induced Fluorescence mass distribution results were compared with an independent mass-catch technique. An agreement is observed between the results of two techniques. The Planar Laser Induced Fluorescence technique is not only an experimental method but also a semi-quantitative fuel injector

performance evaluation tool. The technique might be used as a testing procedure after the injector manufacturing process for the rapid detection of the spray instability and distinguishing unstable injectors.

Quantitative information from a PLIF system is based on the careful measurement of fluorescence intensity, which is proportional to the mass of liquid droplets. The proportionality is valid only if the dye concentration within droplets is constant and uniform. The optical complexities associated with droplets, e.g., lensing and morphology dependent resonances (MDR), may be diminished by using saturation spectroscopy. Selection of the fluorescent dye has a crucial importance during the spray application of the PLIF since the fluorescent dye is an agent to obtain the accurate spray mass information. The spectroscopic properties of six fluorescent dyes in four liquid hydrocarbon solvents were investigated in the range of 250-500 nm in this study in order to select optimal laser excitation and fluorescent emission wavelengths for later droplet and spray experiments. The database involves absorption and fluorescence spectra and other relevant properties of the fluid combinations. By referring to the measured absorption spectra for solutions, the optimal laser excitation for each dye was selected and the suitable laser instruments were recommended. The use of the Nd-Yag 3<sup>rd</sup> harmonic laser is recommended for dyes: POPOP, Anthracene, and LD390. However, the solubility problem of POPOP in selected solvents discourages the use of this dye. The dyes, BBQ and PPO, are suitable for the XeCl Excimer laser applications. Naphthalene is a suitable dye for the Nd-Yag 4<sup>th</sup> harmonic laser applications; but since the obtained extinction coefficient values are low for Naphthalene, it may not provide the detectible level of signal in PLIF applications. Among six dye candidates BBQ provided the highest

extinction coefficient values. Solvent effect was observed in the spectra of BBQ, LD390, and PPO. Since the unseparated absorption and emission maxima may cause self-absorption within the droplet, large Stokes shift is desirable for PLIF applications. Anthracene and LD390 have small Stokes shift and may cause self-absorption. The use of BBQ or PPO is recommended to eliminate self-absorption problem. All dyes have good separation between excitation wavelength and the wavelength of emission peak. The separation of excitation wavelength and emission maxima wavelength simplifies the excitation wavelength filtering during the PLIF application.

The continuing development of laser technology has led to significant advances in resolving the global characteristics of sprays. On the other hand, the dense spray flows are less accessible by the optical methods and need further considerations for optical corrections. The laser diagnostic methods specialized on the dense spray flows require considerably more research.

#### **4.2. Concluding Remarks for Spray Modeling Results**

The dispersed two-phase modeling was conducted by employing the computational fluid dynamics (CFD) code Fluent. The boundary conditions of the solved cases were designed similar to the spray experiments. The modeling results present the capabilities of the CFD code Fluent in the dispersed two-phase flow solutions. Fluent describes continuous phase flow field in an Eulerian reference frame and employs a Lagrangian reference frame to simulate the discrete phase motion. This type of solution method is called the discrete-particle approach. The approach is valid only for dilute spray solutions. In Fluent, the discrete-particle approach is conducted by using the

coupled two-step solution method, meaning that one discrete phase iteration is performed after every specified number of continuous phase iterations. During the discrete phase iteration the mass, momentum, and heat exchange between phases are calculated to obtain the interphase exchange quantities. The continuous phase source terms are updated according to the interphase exchange terms. The current coupled calculations were carried on until the converged continuous phase solution was obtained.

The current study presents the results of two cases with the same input and boundary conditions. The spray in the first case involves only droplets with diameters of 100  $\mu\text{m}$ . A linear droplet diameter distribution between 40  $\mu\text{m}$  and 100  $\mu\text{m}$  is employed in the second case. A core region close to the injection tip with higher velocity values is observed for both cases. The particle traces results indicate higher spray center temperature and velocity values for the constant droplet diameter case. The continuous phase velocity vectors graph shows the entrainment of air along the shear layer.

The lack of an atomization modeling is the most important discrepancy of Fluent in the dispersed two-phase flow solutions. Since the initial droplet field is the result of atomization, the atomization modeling is an important need in the code, especially for low-pressure injection. The discrete-particle approach employed in Fluent is valid only for the solution of dilute sprays, in which the discrete phase volume fraction is about 10 percent or less. The discrete-particle approach should not be used for the dense spray flows. Other commercial codes are available for dense sprays. These codes employ the Eulerian multiphase method (or multi-continua approach). It should be noted that the Eulerian multiphase method can model only droplets of the same size. The effect of continuous phase turbulence on the discrete phase can be taken into account in Fluent.



However, it should be kept in mind that the spray modeling is a complicated problem due to the coupling between two phases. The stochastic approach available in Fluent appeared to add further instability to the solution and create convergence difficulties.

## REFERENCES

- Adrian, R.J. (1991) "Particle-imaging techniques for experimental fluid mechanics," *Annual Review of Fluid Mechanics*, 23: 261-304.
- Baritaud, T.A., Heinze, T.A. (1992) "Gasoline distribution measurements with PLIF in a SI engine," *SAE Paper 922355*.
- Bayraktar, T., Roberts, A.S., Pace, J.B. (2001a) "Spray instability characterization of port fuel injectors by using PLIF," ILASS Americas, *Proceeding of the 14<sup>th</sup> Annual Conference on Liquid Atomization and Spray Systems*, 279-283, Dearborn, MI.
- Bayraktar, T., Roberts, A.S., Pace, J.B. (2001b) "Fluorescence and absorption spectra for use in fuel spray studies," ILASS Americas, *Proceeding of the 14<sup>th</sup> Annual Conference on Liquid Atomization and Spray Systems*, 200-204, Dearborn, MI.
- Berlman, I.B. (1965) *Handbook of Fluorescence Spectra of Aromatic Molecules*, Academic Press, New York.
- Bird, R.B., Stewart, W.E., and Lightfoot, E.N. (1960) *Transport phenomena*, John Wiley & Sons, New York.
- Bos, F. (1981) "Optimization of spectral coverage in an eight-cell oscillator-amplifier dye laser pumped at 308 nm," *Applied Optics*, 20, no. 20, 3553-3556.
- Brackmann, U. (1985) *Lambdachrome Laser Dyes Data Sheets*, Lambda Physik GmbH, Gottingen, Germany.
- Brown, G.M., Kent, J.C. (1983) "Fluorescent light section technique for fuel spray characterization," *Proceedings of the Third International Symposium on Flow Visualization*, 3: 118-122, University of Michigan, Ann Arbor, MI.

- Coleman, H.W., Steele, W.G. (1999) *Experimentation and Uncertainty Analysis for Engineers*, John Wiley & Sons, New York.
- Crowe, C., Sommerfeld, M., Tsuji, Y. (1998) *Multiphase Flows with Droplets and Particles*, CRC Press, Boca Raton, Florida.
- Dantec Dynamics (2001a) "Principles of phase doppler anemometry," retrieved July 11, 2001, from the World Wide Web: <http://www.dantecmt.com/pda/Princip/Index.html>
- Dantec Dynamics (2001b) "Laser doppler anemometry, introduction to principles and applications," retrieved July 11, 2001, from the World Wide Web: <http://www.dantecmt.com/lda/Princip/Index.html>
- Dawson, M., Hochgreb, S. (1998) "Liquid fuel visualization using laser-induced fluorescence during cold start," *SAE Paper 982466*.
- Domann, R., Hardalupas, Y. (2000) "Evaluation of the Planar Droplet Sizing (PDS) Technique," presented at the Eight International Conference on Liquid Atomization and Spray Systems, Pasadena, CA, July 17-20.
- Doroshenko, A.O., Kirichenko, A.V., Mitina, V.G. and Ponomaryov, O.A. (1996) "Spectral properties and dynamics of the excited state structural relaxation of the ortho analogues of POPOP – Effective abnormally large Stokes shift luminophores," *Journal of Photochemistry and Photobiology A: Chemistry*, 94, 15-26.
- Eckbreth, A.C. (1988) *Laser Diagnostics for Combustion Temperature and Species*, Abacus Press, Cambridge, MA, pp. 367.
- Elghobashi, S. and Truesdell G.C. (1992) "Direct simulation of particle dispersion in a decaying isotropic turbulence," *Journal of Fluid Mechanics*, 242, 655-700.
- Exciton Inc. (1992) *Exciton Laser Dyes Catalog*

- Fischer, M., Georges, J. (1996) "Fluorescence quantum yield of rhodamine 6G in ethanol as a function of concentration using thermal lens spectroscopy," *Chemical Physics Letters*, 260, no. 1,2, 115-118.
- Fluent, Inc. (1998) *Fluent Manual*, Lebanon, New Hampshire.
- Georges, J., Arnaud, N. and Parise L. (1996) "Limitations arising from optical saturation in fluorescence and thermal lens spectrometries using pulsed laser excitation: application to the determination of the fluorescence quantum yield of rhodamine 6G," *Applied Spectroscopy*, 50: 1505-1511.
- Ghandhi, J.B., Bracco, F.V. (1996) "Mixture preparation effects on ignition and combustion in a direct-injection spark-ignition engine," *SAE Paper 962013*.
- Godrie P. and Zellat M. (1994) "Simulation of flow field generated by intake port-valve-cylinder configurations-comparison with measurements and applications," *SAE Paper 940521*.
- Gosman, A.D. and Ioannides, E. (1983) "Aspects of computer simulation of liquid-fueled combustors." *Journal of Energy*, 7: 482-490.
- Govan, A.H., Hewitt, G.F. and Ngan, C.F. (1989) "Particle motion in a turbulent pipe flow," *Int. J. Multiphase Flow*, 15: 471-481.
- Greenhalgh, D.A. (1994) "Inelastic scattering laser diagnostics; CARS, planar LIF and planar LII," *Optical Diagnostics for Flow Processes*, (Edited by Lading, L., Wigley, G., and Buchhave, P.), 357-389, Plenum Press, New York.
- Greenhalgh, D.A. (2000) "Laser imaging of fuel injection systems and combustors," *ImechE Journal of Power and Energy*, 214, A4: 367-376.

- Hassan, Y.A. (1992) "Simultaneous Measurements of Both Components of a Two-Phase Flow using Particle Image Velocimetry," *Int. J. Multiphase Flow*, 18: 371-395.
- Hinze, J.O. (1959) *Turbulence; an introduction to its mechanism and theory*, McGraw-Hill, New York.
- Ismailov, M.M., Obokata, T., Kobayashi, K., Polayev, V.M. (1999) "LDA/PDA Measurements of Instantaneous Characteristics in High Pressure Fuel Injection and Swirl Spray," *Experiments in Fluids*, 27: 1-11.
- Itoh, T., Kakuho, A., Hishinuma, H., Urushihara, T., Takagi, Y., Horie, K., Asano, M., Ogata E., and Yamasita, T. (1995) "Development of a new compound for use with laser induced fluorescence," *SAE Paper 952465*.
- Kotzubanov, V.D., Naboikin, Yu.V., Ogurtsova, L.A., Podgornyi, A.P., Povrovskaya, F.S. (1968) "Laser Action in solutions of organic luminophors in the 400-650 nm range," *Optics and Spectroscopy*, 25, no. 5, 406-410.
- Kuo K.K. (1986) *Principles of combustion*, John Wiley & Sons, New York.
- Lauder, B.E. and Spalding, D.B. (1974) "The numerical computation of turbulent flows," *Computational Methods in Applied Mechanics and Engineering*, 3: 269-289.
- Le Gal, P., Farrugia, N., and Greenhalgh, D.A. (1999) "Laser sheet dropsizing of dense sprays," *Optics and Laser Technology*, 31: 75-83.
- Lenz, H.P. (1992) *Mixture Formation in Spark-Ignition Engines*, Springer-Verlag/Wien, New York.
- Lewis, R.J. (1992) *Sax's Dangerous Properties of Industrial Materials*, Van Nostrand Reinhold, New York.

- Litchford, R.J., Jeng S.-M. (1991) "Efficient statistical transport model for turbulent particle dispersion in sprays," *AIAA Journal*, 29: 1443-1451.
- Mello, J.C., Wittmann, H.F., Friend, R.H. (1997) "An improved experimental determination of external photoluminescence quantum efficiency," *Advanced Materials*, 9: no. 3, 230-232.
- Meyer, R. (1998) *Liquid Fuel Transport into the Cylinder in Spark Ignition Engines*, PhD Thesis, Massachusetts Institute of Technology, Cambridge, MA.
- Morsi, S.A. and Alexander, A.J. (1972) "An investigation of particle trajectories in two-phase flow systems," *Journal of Fluid Mechanics*, 55: 193-208.
- Muralidhara, H.S., Shembharkar, T.R., Chidananda, M.S., Sundarrajan, T., and Shet, U.S.P. (2000) "Numerical simulation of two phase combustion in a gas turbine combustor," 5<sup>th</sup> National Conference on Air Breathing Engines and Aerospace Propulsion, December 21-23, Hyderabad, India.
- Naqwi, A.A., Menon, R., Fingerson, L.M. (1996) "An Adaptive Phase/Doppler System and Its Applications Including Particle Sizing in Submicron and Nanometer Ranges," *Experiments in Fluids*, 20: 328-334.
- Neij, H., Johansson, B., and Alden, M. (1994) "Development and demonstration of 2D-LIF for studies of mixture preparation in SI engines," *Combustion and Flame*, 99: 449-457.
- Patankar, S.V. (1980) *Numerical Heat Transfer and Fluid Flow*, McGraw-Hill, New York.
- Paul, P.H., van Cruyningen, I., Hanson, R.K., and Kychakoff, G. (1990) "High resolution digital flowfield imaging of jets," *Experiments in Fluids*, 9:241-251.

- Perkins, R.J., Hunt, J.C.R. (1989) "Particle Tracking in Turbulent Flows," *Advances in Turbulence 2*, Berlin: Springer-Verlag, 286-291.
- Raffel, M., Willert, C., Kompenhans, J. (1998) *Particle Image Velocimetry, A Practical Guide*, Berlin: Springer-Verlag.
- Ranz, W.E., Marshall, W.R. (1952) "Evaporation from drops – I and II," *Chemical Engineering Progress*, 48: 141-180.
- Reuss, D.L., Adrian, R.J., Landreith, C.C., French, D.T., and Fansler, T. (1989) "Instantaneous Planar Measurements of Velocity and Large Scale Vorticity and Strain Rate in an Engine Using Particle Image Velocimetry," *SAE Paper 89061*.
- Sankar, S.V., Maher, K.E., Robart, D.M., Bachalo, W.D. (1999) "Rapid characterization of fuel atomizers using an optical patternator," *Journal of Engineering for Gas Turbines and Power*, 121: 409-414.
- Sirignano, W.A. (1993) "Fluid dynamics of sprays-1992 freeman scholar lecture," *Journal of Fluid Engineering*, 115: 345-378.
- Skoog, D.A. and West, D.M. (1971) *Principles of Instrumental Analysis*, Holt, Rinehart, and Winston Inc., New York.
- Straughan, B.P. and Walker, S. (1976) *Spectroscopy, Volume Three*, John Wiley and Sons Inc., New York.
- Swindal, J.C., Acker, W.P., Chen, G., Serpenguzel, A., Chang, R.K. (1996) "Spray Diagnostics with Lasing and Stimulated Raman Scattering," *Progress in Astronautics and Aeronautics*, 171: 63-90.
- Talley, D.G., Thamban, A.T.S., McDonnell, V.G., Samuelsen, G.S. (1996a) "Laser sheet visualization of spray structure," *Recent Advances in Spray Combustion: Spray*

*Combustion Measurements and Model Simulation II in Progress in Astronautics and Aeronautics*, 171: 113-141.

Talley, D.G., Verdieck, J.F., Lee, S.W., McDonell, V.G., Samuelsen, G.S. (1996b)

“Accounting for laser sheet extinction in applying PLLIF to sprays,” 34<sup>th</sup> Aerospace Sciences Meeting and Exhibit, January 15-18, Reno, NV, *AIAA 96-0469*.

Telle, H., Huffer, W. (1981) “The XeCl excimer laser: a powerful and efficient UV pumping source for tunable dye lasers,” *Optics Communications*, 38, no. 5,6, 402-406

Van Cruyningen, I., Lozano, A., and Hanson, R.K. (1990) “Quantitative imaging of concentration by planar laser-induced fluorescence,” *Experiments in Fluids*, 10: 41-49.

Wayne, R.P. (1970) *Photochemistry*, American Elsevier Publishing Company, Inc., New York.

Wild, P.N., Boysan, F., Swithenbank, J. (1988) “Spray combustor modeling,” *Journal of the Institute of Energy*, 27-32.

Yeh, C.-N., Kosaka, H., and Kamimoto, T. (1996) “Measurement of drop sizing in unsteady dense sprays,” *Recent Advances in Spray Combustion: Spray Atomization and Drop Burning Phenomena I in Progress in Astronautics and Aeronautics*, 166: 297-308.

Yurteri, C.U., Kadambi, J.R., Arik, E. (1993) “Spray Characterization and Droplet Interactions Study Using Particle Dynamic Analyzer,” *Laser Anemometry Advances and Applications*, 2052: 145-152.



Ziegler, L.D., Hudson, B.S. (1980) "Tuning ranges of 266 nm pumped dyes in the near UV," *Optics Communications*, 32, no. 1, 119-120.

## APPENDIX

### INCIDENT INTENSITY MEASUREMENTS

The incident intensity measurements were made to determine the incident intensity uncertainty. For each solvent ten scans were made on a pure solvent filled cuvette. The line in each graph shows the average intensity of ten scans and error bars indicate the maximum discrepancy from the average intensity. The following settings were used during the measurements:

- (1) The scanned wavelength range was between 250 nm and 400 nm.
- (2) The number of data points taken for each scan was 300.
- (3) 10 ms integration time was specified for the data collection system (Acton SpectraCard SC-1).
- (4) The operating voltage for the photomultiplier tube was specified as 650 V.

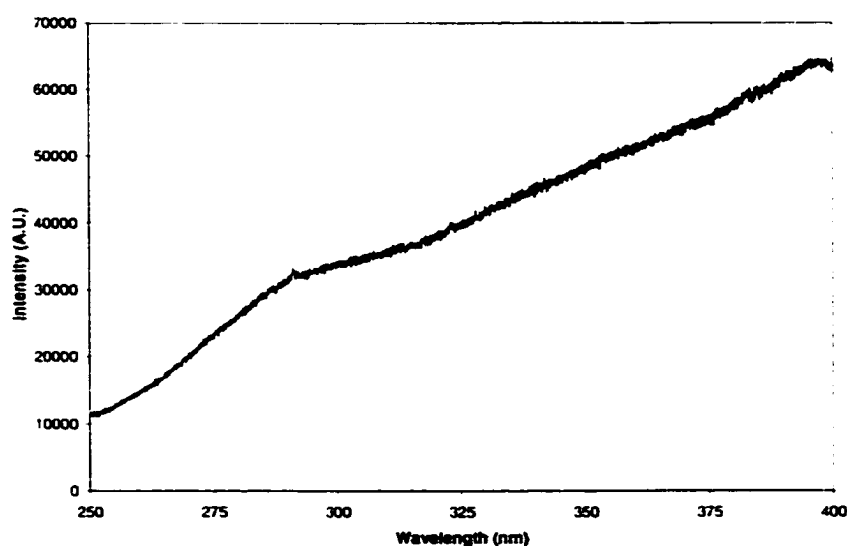


Figure A.1 Intensity fluctuations for Cyclohexane.

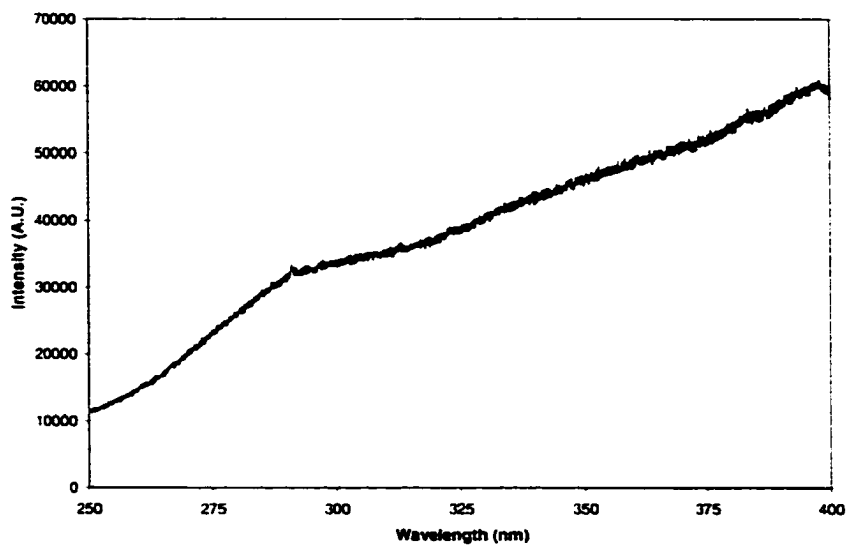


Figure A.2 Intensity fluctuations for Heptane.

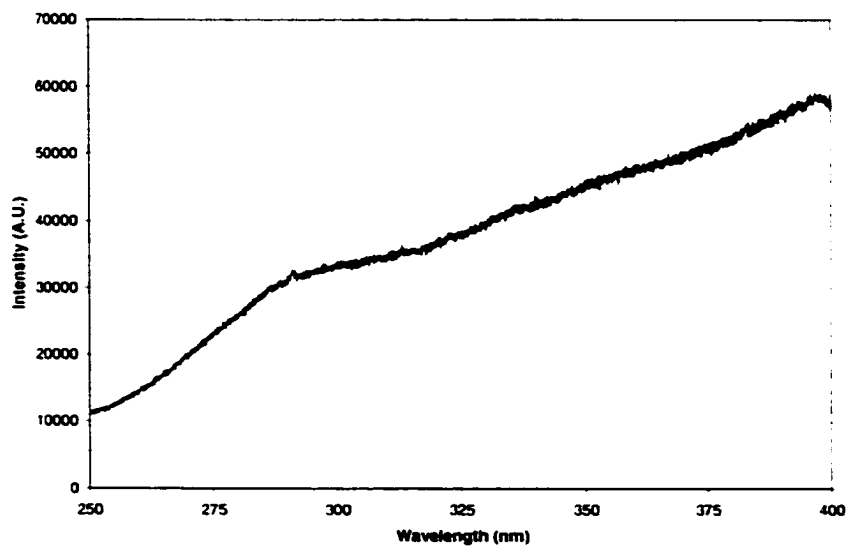


Figure A.3 Intensity fluctuations for Hexane.

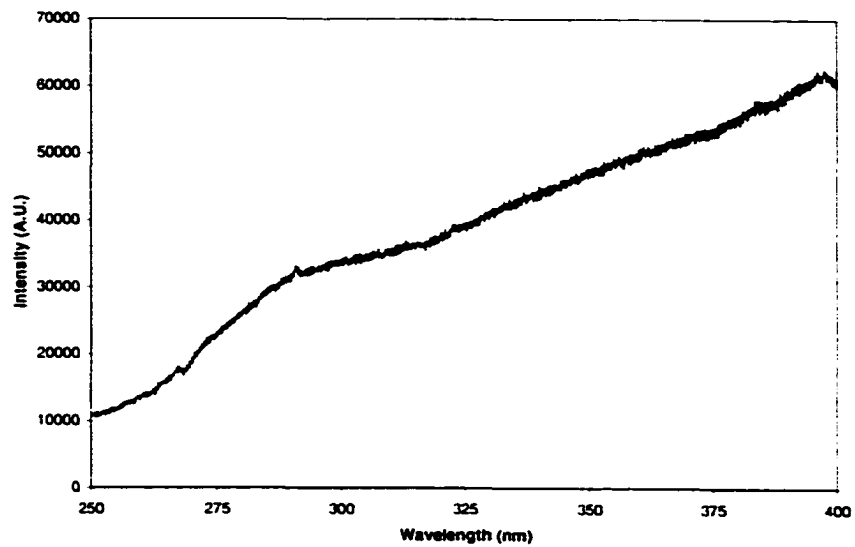


Figure A.4 Intensity fluctuations for Octane.

## **CURRICULUM VITA**

**for  
Tuba Bayraktar**

### **DEGREES:**

Doctor of Philosophy (Mechanical Engineering), Old Dominion University, Norfolk, VA, August 2002

Master of Science (Mechanical Engineering), Istanbul Technical University, Istanbul, Turkey, January 1997

Bachelor of Science (Mechanical Engineering), Suleyman Demirel University, Isparta, Turkey, June 1993

### **PROFESSIONAL CHRONOLOGY:**

Department of Mechanical Engineering, Old Dominion University, Norfolk, Virginia

Research Assistant, August 1998 – Present

Department of Mechanical Engineering, Old Dominion University, Norfolk, Virginia

Teaching Assistant, January – December 2001

Industrial Assessment Center, Old Dominion University, Norfolk, Virginia

Project Engineer, August 1998 – November 2000

Department of Mechanical Engineering, Southern Methodist University, Dallas, Texas

Research Assistant, August 1997 – May 1998

Department of Mechanical Engineering, Istanbul Technical University, Istanbul, Turkey

Teaching and Research Assistant, February 1996 – July 1997

### **SCIENTIFIC AND PROFESSIONAL SOCIETIES MEMBERSHIP:**

American Society of Heating, Refrigerating and Air Conditioning, 2001

Institute for Liquid Atomization and Spray Systems, 2001

American Institute of Aeronautics and Astronautics, 2000

### **SELECTED PUBLICATIONS:**

Bayraktar, T., Roberts, A. S. and Pace, J. B., 2001, "Fluorescence and Absorption Spectra for Use in Fuel Spray Studies," ILASS Americas, 14<sup>th</sup> Annual Conference on Liquid Atomization and Spray Systems, Dearborn, MI.

Bayraktar, T., Roberts, A. S. and Pace, J. B., 2001, "Spray Instability Characterization of Port Fuel Injectors Using PLIF," ILASS Americas, 14<sup>th</sup> Annual Conference on Liquid Atomization and Spray Systems, Dearborn, MI.